NTNU

Norwegian University of
Science and Technology

Sorbents for Sulfur Removal From Biomass-derived Syngas

Siri Stavnes

Chemical Engineering and Biotechnology
Submission date: June 2018
Supervisor: Edd Anders Blekkan, IKP
Co-supervisor: Kumar R. Rout, SINTEF
Jianyu Ma, IKP

Norwegian University of Science and Technology
Department of Chemical Engineering

There are no secrets to success.
It is the result of preparation, hard work,
and learning from failure.
- Colin Powell

Preface

This master´s thesis was written as a final part of the Master of Science degree in Chemical Engineering at the Norwegian University of Science (NTNU). The thesis is written for the Catalysis group at the Department of Chemical Engineering, in close collaboration with SINTEF.

Foremost, I would like to express my sincere thanks to my supervisor at NTNU, professor **Edd A. Blekkan**, for his guidance in the completion of this master´s thesis. I am grateful for all his valuable input and for always taking the time to answer questions.

I would also express my gratitude to my co-supervisors, Dr. **Kumar Rout** at SINTEF for valuable help in the lab and academic guidance, and **Jianyu Ma** (PhD at Department of Chemical Engineering) for all his help during the course of work, valuable discussions and for always being available and keeping my motivation up.

Finally, I would like to thank **Karin Wiggen Dragsten** for giving me practical training in using different instruments at the lab.

Declaration of compliance:

I declare that this is an independent work according to the exam regulations of the Norwegian University of Science and technology (NTNU).

Trondheim, June 28th, 2018

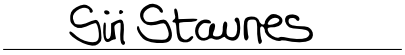

Siri Stavnes

Abstract

The rising concern of global warming and emission of greenhouse gases have increased the demand for sustainable resources. Biomass is carbon neutral and a renewable energy source, thus a promising alternative to produce biofuels for the replacement of fossil fuels. Biomass gasification is one possible pathway for biofuel production. However, a drawback of this process is the produced syngas which contains undesirable contaminants. Sulfur species are most detrimental and can cause severe damages on downstream equipment. Moreover, sulfur species are a known catalyst poison and have a negative impact on the environment. Thus, it is strongly desirable to remove these contaminants from the process. High-temperature gas cleaning using solid sorbents is a energy efficient and low-cost method for removal of sulfur, and several materials have been studied for this purpose. Manganese possesses great advantages such as high thermal stability and sorption capacity, thus a promising alternative. The main objective of this paper was to optimize alumina (Al_2O_3)-supported manganese oxide (MnO_x) sorbents for high-temperature sulfur removal by zirconium oxide (ZrO_2) modification.

A series of regenerable Zr-promoted Mn/Al_2O_3 sorbents were prepared by incipient wetness impregnation using Zr- and Mn-nitrate precursor. Sorbents were calcined in air at 500°C and 700°C, and Zr-loading varied from 0, 1, 5 and 10wt%. In addition, a selection of sorbents were prepared by co-precipitation (0, 1 and 10wt% Zr). Desulfurization performance of the prepared sorbents were tested in a quartz fixed bed reactor over ten (10) sorption and regeneration cycles. Moreover, the effect of Zr-loading, calcination temperature and preparation method on sorbent capacity and stability was investigated. N_2-adsorption, X-ray diffraction (XRD), temperature programmed reduction (TPR), X-ray fluorescence (XRF) and scanning electron microscopy (SEM) were applied to characterize the fresh and reacted sorbents.

The overall result indicates that the Zr1-Mn/Al_2O_3 (1wt% Zr and 15wt% Mn) sorbent prepared by incipient wetness impregnation and calcined at 700°C is a promising candidate for removal of H_2S. This sorbent showed the best desulfurization performance, and higher calcination temperature is beneficial as less deactivation is observed. Although sorbents prepared by co-precipitation have a higher initial capacity, the deactivation is larger after multiple sorption and regeneration cycles.

Sammendrag

En økt bekymring for klimagassutlsipp og global oppvarming har ført til større etterspørsel etter bærekraftige ressurser. Biomasse, som er karbonnøytral og en fornybar energikilde, er derfor et lovende alternativ til produksjon av biobrensel som kan erstatte fossilt brensel. Gassifisering av biomasse er en av flere mulige veier til produksjon av biodrivstoff. En ulempe ved denne prosessen er dannelsen av syntesegass som inneholder uønskede forurensinger, spesielt svovel som er sterkt ødeleggende for både miljøet, prosessutstyr og en kjent katalysatorgift. Det er derfor av stor interesse å fjerne disse forurensningene fra prosessen. Gassrensing ved høy temperatur, og ved bryk av faste sorbenter, er en energieffektiv og løsnnsom metode for å fjerne svovel. Flere materialer har blitt studert til dette formålet, og et lovende alternativ er mangan som har mange gode egenskaper, blant annet høy termisk stabilitet og sorpsjonskapasitet. Hovedmålet med denne oppgaven var å optimalisere manganoksid-baserte sorbenter på aluminia-bærer ved å tilføre zirconiumoksid som modifikator (ZrO_2-MnO_x/Al_2O_3), hvor disse videre kan brukes for å fjerne svovel ved høy temperatur.

En serie Zr-modifiserte Mn/Al_2O_3 sorbenter ble fremstilt ved impregnering ved bruk av nitratbaserte Mn- og Zr-forløpere. Sorbentene ble kalsinert i en luftstrøm ved 500°C og 700°C, og innholdet av Zr varierte fra 0, 1, 5 og 10wt%. I tillegg ble et utvalg av sorbenter fremstilt ved medutfelling (0, 1 og 10wt% Zr). For å undersøke yteevnen hver sorbent hadde til å fjerne svovel ble sorbentene testet i en kvartsreaktor over 10 sorpsjons- og regenereringssykluser. Videre ble effekten av varierende Zr-innhold, kalsineringstemperatur og prepareringsmetode på sorbentkapasitet og stabilitet undersøkt. Ulike teknikker ble anvendt for å karakterisere sorbentene: N_2-adsorpsjon-desorpsjon, røntgendiffraksjon (XRD), temperaturprogrammert reduksjon (TPR), røntgenfluorescens (XRF) og elektronmikroskopi (SEM).

Resultatene indikerer at sorbenten modifisert med 1wt% Zr (Zr1-Mn15/Al_2O_3), fremstilt ved impregnering og kalsinert ved 700°C, er et lovende alternativ for fjerning av H_2S. Denne sorbenten viste best yteevne til å ta opp H_2S, og høyere kalsineringstemperatur er gunstig da det observeres mindre deaktivering. Medutfelling har høyere innledende kapasitet, men deaktiveringen er større etter flere sorpsjons- og regenereringssykluser.

Table of Contents

List of Tables

List of Figures

Abbreviations

BET	Brunauer-Emmett-Teller
BJH	Barrett-Joyner-Halenda
BFB	Bubbling fluidized bed
CFB	Circulating fluidized bed
CP	Co-precipitation
EU	European Union
IWI	Incipient wetness impregnation
MBR	Moving bed reactor
PJ	Petajoule
ppm	parts per million
ppmv	parts per million volume
SEM	Scanning Electron Microscope
TCD	Thermal Conductivity Detector
TPR	Temperature Programmed Reduction
XRD	X-Ray Diffraction
XRF	X-Ray Fluorescence

Symbols

C	=	BET constant
d	=	Distance between two lattice planes
k	=	Shape factor
L	=	Crystallite particle size
n	=	An integer as the order of reflection
P	=	Partial vapour pressure
P_o	=	Saturated pressure
R	=	Gas constant
r_m	=	Mean pore radius
T	=	Absolute isothermal temperature
V	=	Volume of adsorbed nitrogen gas
V_L	=	Molar volume of liquid adsorbate
V_m	=	Volume of adsorbed nitrogen gas at monolayer coverage
β	=	Peak width at half peak height
γ	=	Surface tension of liquid adsorbate
θ	=	Diffraction angle
λ	=	Wavelength of the X-ray

Chapter 1

Introduction

1.1 Motivation

Use of sustainable resources for the production of fuels and chemicals have received great attention. Biomass is carbon neutral and a renewable energy source, hence biomass gasification is a promising route to produce biofuels that can replace fossil fuels. However, the produced syngas from gasification contains several undesired contaminants such as alkali, tars and sulfur species that consequently damage downstream equipment [1]. Sulfur species are acidic and can corrode metal. Moreover, the oxidized form of sulfur is sulfur dioxide (SO_2), which is a pollutant, and any emission of this compound is harmful to both health and environment and require strict emission control. H_2S is the main sulfur species present, a known catalysts poison that causes deactivation. Catalysts used in Fischer-Tropsch fuel synthesis, e.g., cobalt, are negatively influenced by the presence of sulfur, as a substantial decrease in activity occur [2]. Hence, gas cleaning to remove sulfur is essential.

High-temperature gas cleaning is favourable as no cooling and reheating is necessary, thus provide higher energy efficiency and is economically beneficial. Several sorbents for high-temperature sulfur removal have been studied [1], of which manganese possesses many beneficial properties such as high thermal stability, resistance against reduction and ability to regenerate and be used in chemical looping desulphurization.

1.2 Objective

This master´s thesis is a continuation of a specialization project that was completed in autumn 2017, where the aim was to develop sorbents for high temperature removal of sulfur. It is a part of a larger project where the final goal is to develop a new reactor system with relevance to the Chemical Looping Desulfurization (CLD) technology where these sorbents can be utilized.

The present work is based on a previous study by Milly Kure [3] that investigated the effect of different supports on manganese oxide, in addition to sorbent capacity and stability. Alumina was chosen for further studies although it did not show the best performance. However, advantages with alumina compared to other supports are the large surface area, relatively high stability and low cost.

The main objective of the present work is to optimize alumina-supported manganese oxide sorbents for high-temperature sulfur removal by zirconium oxide modification. Moreover, investigate the effect of Zr-loading, calcination temperature and preparation method on sorbent capacity and stability.

Chapter 2

Literature Review

The rising concern of global warming and emission of greenhouse gases, such as carbon dioxide, have increased the demand for renewable energy to replace fossil resources. At present, it appears that biofuels, derived from biomass, are the only source of sustainable liquid fuels. A significant decrease in emissions and the possibility of having greenhouse gas neutral feedstock make biofuels an essential element in the transportation sector [4]. In 2007 the European Commission approved the European Union (EU) 20-20-20 strategy with the goal of reaching 20% reduction of greenhouse gases by using 20% renewable energy sources within 2020. Further, the European Commission specified that biofuels used in the transportation sector should account for minimum 10% by 2020 [5]. Based on figures from 2006 by *Statistics Norway*, Norway had an energy consumption of 217 PJ (PJ=10^{15} J) in the transportation sector, whereas the total potential for biomass growth is about 145 PJ annually, where wood is the main feedstock among the biomass resources [6]. Based on this, it is possible to cover the transportation needs with about 53% if all the grown biomass is harvested and converted at an energy efficiency of 80%. Production of biofuels from biomass feedstocks is therefore highly interesting as it reduces the emission of harmful gases and offers a carbon neutral alternative as an energy source.

2.1 Biomass Feedstock

Biomass is often referred to as organic plant materials, which commonly denoted as lignocellulosic biomass. A potential lignocellulosic biomass feedstock includes plants and wood, agricultural and forest wastes and energy crops such as grass and corn. The main constituents in lignocellulosic biomass are cellulose (40-80%), hemicellulose (15-30%) and lignin (10-25%), which forms from the building blocks of biomass, namely sugar ($(CH_2O)_n$). Formation of the sugar building blocks occur when the plant material react with carbon dioxide from the atmosphere and water using solar energy, according to equation 2.1 [4].

$$nCO_2 + nH_2O + light \xrightarrow{chlorophyll} (CH_2O)_n + nO_2 \tag{2.1}$$

Cellulose consists of linear glucose polymer chains and tends to form hydrogen bonds, giving a crystalline structure with high tensile strength to the cell walls. In contrast, hemicellulose consists of branched chains with five different sugar polymers and has an amorphous structure with low strength. Lignin is a complex, cross-linked polyphenolic polymer with an amorphous structure based on benzene rings [4, 7]. The chemical structures of cellulose, hemicellulose and lignin are given in Figure 2.1 to Figure 2.3.

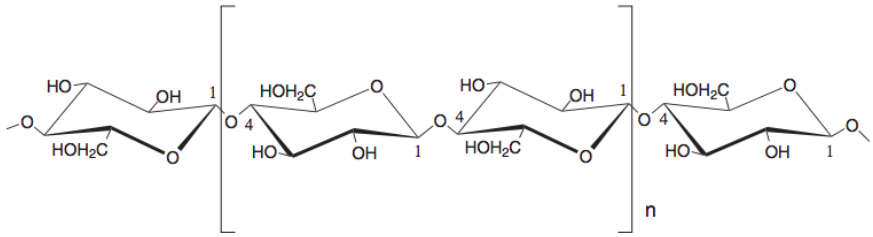

Figure 2.1: Chemical structure of cellulose [7]

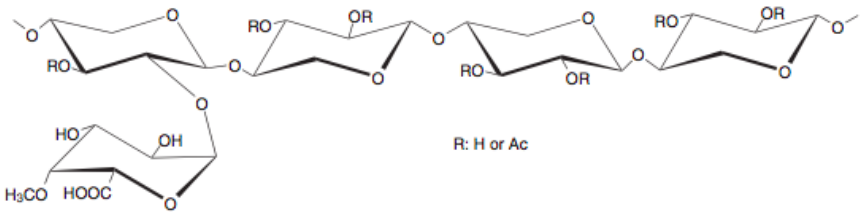

Figure 2.2: Chemical structure of woody hemicellulose [7]

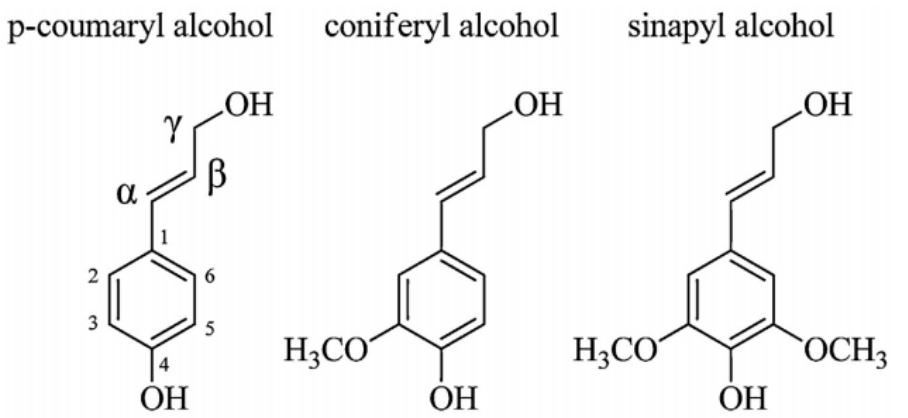

Figure 2.3: Chemical structure of the main three building blocks of lignin [4]

2.2 Biomass Conversion

There are two main paths for the conversion of biomass into fuels and chemicals, as shown in Figure 2.4. Thermochemical conversion includes the production of bio-oil through both pyrolysis and liquefaction, and production of syngas by gasification, whereas biochemical conversion, produce bioethanol and biodiesel [4].

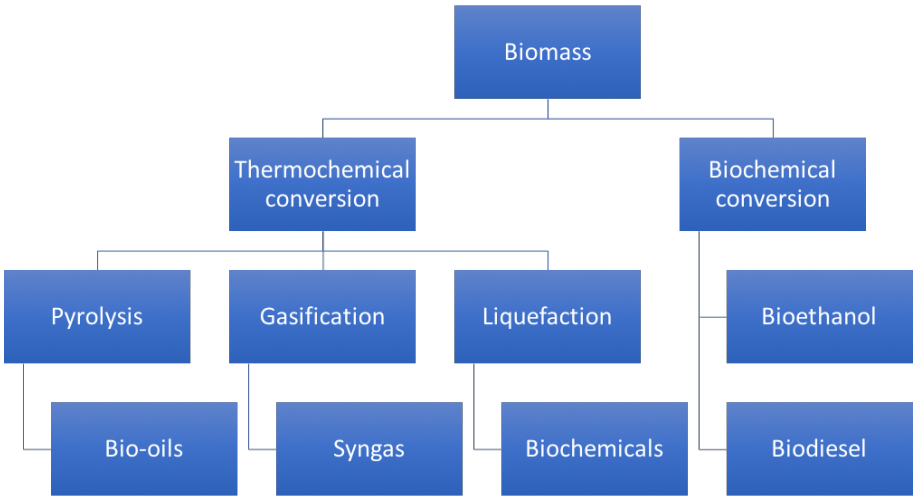

Figure 2.4: Biomass conversion processes

2.3 Biomass Gasification

Biomass gasification is a thermal process in which biomass is converted to synthesis gas after reacting with a gasifying oxidant such as oxygen, air or steam at high temperatures (800-1300°C). The generated synthesis gas, also called syngas, consist of mainly H_2, CO, CO_2 and CH_4. However, other undesired byproducts such as tars, particulate matter, sulfur, nitrogen, chlorine and alkali compounds are also produced [4, 8]. Section 2.3.3 give a more detail description of these contaminants.

2.3.1 Gasification Chemistry

As mentioned above, syngas is produced during gasification at high temperatures. However, there are a number of other reactions that take place followed by the formation of several byproducts, and the major reactions involved during gasification are pyrolysis, partial oxidation, steam reforming, water gas shift reaction and methanation [4]. Reactions of selected cellulose that occur during gasification are listed in Table 2.1. The formation of sulfur pollutants during biomass gasification can be described by the reactions listed in Table 2.2.

Table 2.1: Reactions of selected cellulose that occur during gasification [4]

Classification	Stoichiometric reaction	Enthalpy [kJ/kg][a]
Pyrolysis	$C_6H_{10}O_5 \rightarrow 5CO + 5H_2 + C$	180
	$C_6H_{10}O_5 \rightarrow 5CO + CH_4 + 3H_2$	300
	$C_6H_{10}O_5 \rightarrow 3CO + CO_2 + 2CH_4 + H_2$	-142
Partial oxidation	$C_6H_{10}O_5 + 1/2O_2 \rightarrow 6CO + 5H_2$	71
	$C_6H_{10}O_5 + O_2 \rightarrow 5CO + CO_2 + 5H_2$	-213
	$C_6H_{10}O_5 + 2O_2 \rightarrow 3CO + 3CO_2 + 5H_2$	-778
Steam gasification	$C_6H_{10}O_5 + H_2O \rightarrow 6CO + 6H_2$	310
	$C_6H_{10}O_5 + 3H_2O \rightarrow 4CO + 2CO_2 + 8H_2$	230
	$C_6H_{10}O_5 + 7H_2O \rightarrow 6CO_2 + 12H_2$	64
Water gas shift	$CO + H_2O \rightarrow CO_2 + H_2$	-41
Methanation	$CO + 3H_2 \rightarrow CH_4 + H_2O$	-206

[a] Ref. temp. 300K

Table 2.2: Sulfur formation reactions during gasification [9, 10]

Classification	Chemical reaction
Biomass devolatilization	Biomass-S + heat → H_2S + COS ... + char-S
Gas phase reactions	CO + H_2 + COS → H_2 + COS CO_2 + H_2S → COS + H_2O H_2S + COS → CS_2 + H_2O
Char oxidation	Char-S + O_2 → SO_2 Char-S + H_2O → H_2S Char-S + CO_2 → COS

2.3.2 Gasification Reactors

The reactor design for conventional gasifiers can be classified as moving bed gasifiers, fluidized bed gasifiers and entrained flow gasifiers [11].

Moving bed gasifiers

Moving bed gasifiers can be categorized as updraft and downdraft moving bed gasifiers, where biomass feed is introduced at the top of the reactor. For the updraft gasifier, the oxidant enters from the bottom of the reactor in countercurrent flow with the feed. In contrast, the oxidant enters from the top of the reactor in the downdraft gasifier, allowing the biomass feed to flow co-current with the oxidant [4, 11]. The updraft and downdraft gasifier design are shown in Figure 2.5. The countercurrent process in an updraft gasifier is highly energy efficient, however, a weakness of the moving bed reactor is the large number of undesired byproducts that form, some of them being ammonia tars, condensable hydrocarbons, dust and ash [12].

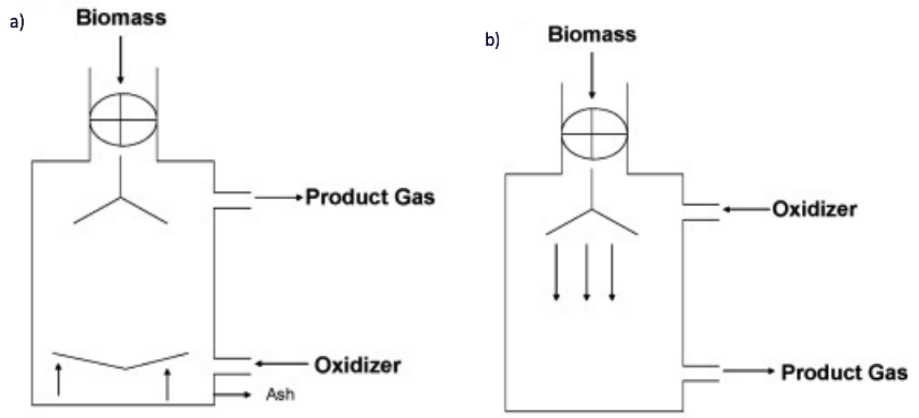

Figure 2.5: Principal design of a) updraft gasifier and b) downdraft gasifier [4]

Fluidized bed gasifiers

Fluidized bed gasifiers are different from moving bed gasifiers as the biomass feed enters the bottom of the reactor as shown in Figure 2.6. Due to the gasifying oxidant flowing upward at a suitable rate the biomass is maintained in the fluidized state. The fluid bed consists of inert material such as alumina, quartz sand or dolomite which is perfectly mixed with the biomass to improve the heat transfer and achieve a uniform temperature in the region of conversion. The fluidized gasifier usually operates at temperatures between 800-900°C, but unfortunately, the conversion rates of tar are rather low at this temperature. Even though the process is complex, fluidized bed reactors demonstrate better performance compared to the moving bed reactor [8].

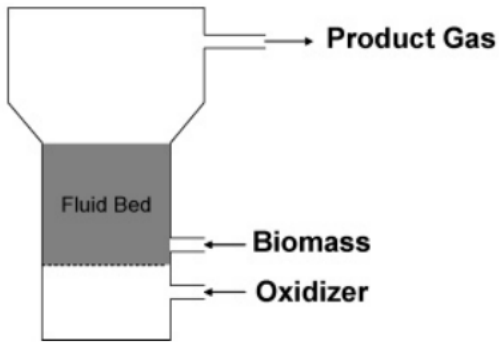

Figure 2.6: Principal design of fluidized bed gasifier [4]

Fluidized bed gasifiers have to main configurations, namely bubbling fluidized bed (BFB) and circulating fluidized bed (CFB). A schematic design of these gasifiers is shown in Figure 2.7.

Bubbling fluidized bed gasifiers contain a vessel where the gasifying oxidant is introduced from the bottom of the reactor and flows upward at a velocity high enough to ensure agitation of the bed material and upheld the temperature requirement. Biomass feed enters from the side of the gasifier and into the bed where char and tar are gasified due to the high bed temperature. Ash is separated out from the product gas (syngas), which contain low to medium tar content. A few issues regarding this type of gasifier is the back mixing which inhibits the conversion of solids, and development of oxidation spots because the oxygen diffusion is slow [8].

Circulating fluidized bed gasifiers contains a vessel where the gasifying oxidant is introduced from the bottom of the reactor and flows upward at a velocity high enough to provide long residence time and complete mixing by transferring the bed material in a loop. Biomass is mixed with the dispersed bed material. The CFB gasifier contain a cyclone which separates the solids into a gas product stream which exit at the top, and the rest going back to the gasifier. The design of a circulating fluidized bed demonstrates better contact between the gas and solid because bubbles are nonexistent which keep the gas from passing by the bed [8].

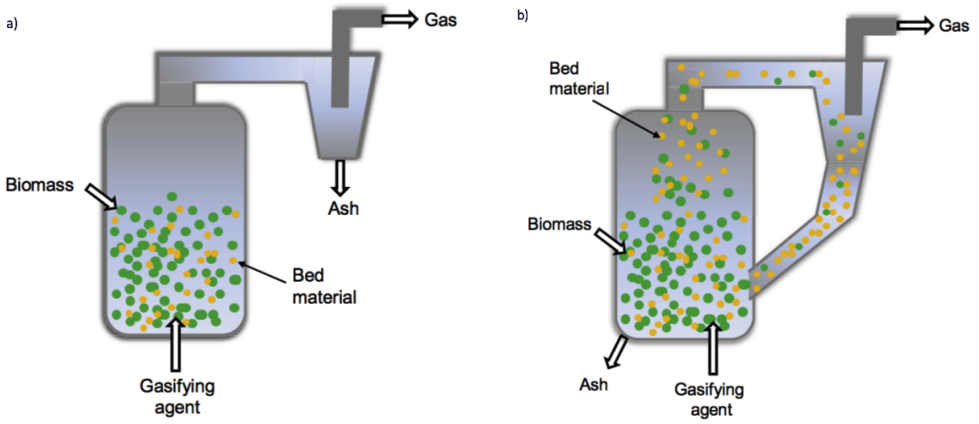

Figure 2.7: Schematic design of a) bubbling fluidized bed (BFB) reactor and b) circulating fluidized bed (CFB) reactor [8]

Entrained flow gasifier

Some challenges regarding this type of gasifier have been discussed by Bermudez and Fidalgo [8], such as short residence time, requirement of fine particles, ash content and difficulty of the processing biomass feedstocks. However, some configurations of entrained flow gasifiers (Figure 2.8) have demonstrated promising results regarding destruction ability of tar, low content of methane and high conversion rate of carbon [13, 14].

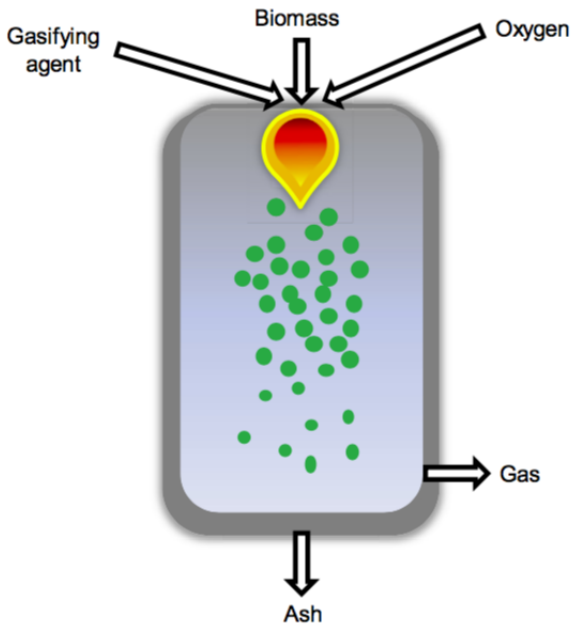

Figure 2.8: Schematic design of entrained flow gasifier [8]

2.3.3 Contaminants

Tars consist of hydrocarbons that are condensable such as polycyclic aromatic hydrocarbons (PAH) and heavy deoxygenated hydrocarbons. More heavy hydrocarbons are produced at high temperatures and long reaction time, but the tar yield reduces. Formation of tars is problematic as it cause condensation on the walls of downstream equipment, hence result in clogging and fouling of pipes and filters. It can also cause catalyst deactivation which affects further processing of syngas to other useful products [2].

Particulate matter is composed of unconverted biomass materials, mainly residual solid carbon (char) and inorganic compounds (ash), although bed materials from the gasifier may be included as well. The composition varies depending on process and feedstock, and the particles have a different size ranging from less than 1 μm to more than 100 μm. Fouling, corrosion and erosion are common problems with regard to particulate matter [2].

Nitrogen is mainly present as ammonia (NH_3) and molecular nitrogen (N_2), and smaller amounts of hydrogen cyanide (HCN). Decomposition of ammonia to molecular nitrogen occur at typical gasification temperatures, and a problem related to this is that molecular nitrogen is a possible source of thermal NOx emission and catalyst poisoning [2].

Chlorine is typically present as hydrochloric acid (HCl). HCl is formed due to vaporization of the chlorine in biomass during gasification and further reaction with water vapour. The presence of chlorine compounds can lead to poisoning of catalyst and corrosion of equipment [2].

Alkali compounds consist of mainly potassium (K) and sodium (Na). The compounds are volatile and reactive, and vaporize at temperatures higher than 600°C. Alkali compounds can react with species in the gasifier (e.g. chlorine), hence form chlorides, sulfates and hydroxide which can cause corrosion and fouling of equipment. Furthermore, catalysts can easily be deactivated by alkali compounds [2].

Sulfur is mainly present as hydrogen sulfide (H_2S) but also carbonyl sulfide (COS) is produced, although in smaller quantities. Sulfur species are acidic and can corrode metal surfaces and poison the catalyst. The oxidized form of sulfur is sulfur dioxide (SO_2), which is a pollutant, and any emission of these compounds is harmful to both health and environment and require strict emission control [2]. Due to these reasons, it is highly desirable to remove sulfur from the biomass-derived syngas.

2.4 Cleaning Technologies for Sulfur Removal

The content of hydrogen sulfide in raw syngas derived from biomass varies with the feedstock. For wood, the content is 20-100 ppmv, whereas for herbaceous feedstock the content is 300-600 ppmv. In any case, it is desirable to keep the sulfur level as low as possible, often also a requirement, due to factors such as deactivation of catalysts, damage on downstream process equipment and emissions [1]. Several methods exist for the removal of sulfur alongside with other species from biomass-derived syngas, and some of the most used cleaning technologies are presented in the following sections.

2.4.1 Scrubbing

Low temperature gas cleaning using amine scrubbers are typically used to remove sulfur and other components. Figure 2.9 illustrates the conversion from biomass to biofuels using this method. The downside of the amine scrubbing process is the necessity to lower the temperature of the syngas from gasification temperature at approximately 850°C to 50°C for cleaning of the gas. Simultaneously, tar condensation occurs which generates a large waste stream, lowers the utilization of carbon from the biomass and makes operation difficult as it causes fouling and plugging of the condenser and pipelines. After the low temperature cleaning process, the cleaned syngas need to be reheated up to synthesis temperature [1]. Cooling and reheating of the syngas is costly, and tar build up on the reactor walls inhibits heat recovery, thus making the process thermally inefficient resulting in loss of energy [15, 16].

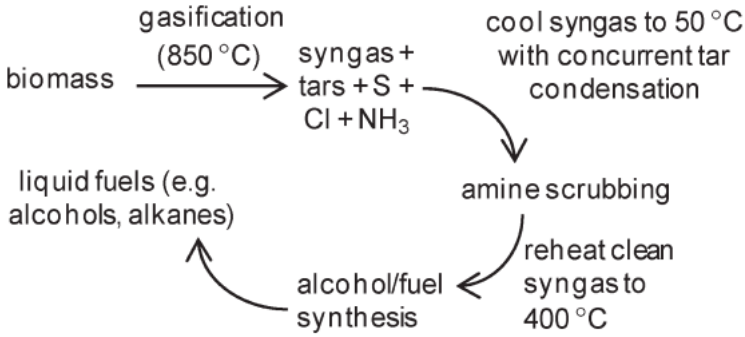

Figure 2.9: Schematic diagram of one possible pathway to convert biomass to biofuel, using the amine scrubbing process for cleaning of the biomass-derived syngas [1].

For these reasons high temperature gas cleaning is preferred as no cooling and reheating of the gas stream is necessary since the process operates between the gasification temperature and the synthesis temperature. This enhances the efficiency of the process and prevent heat loss. The gasification temperature is typically 850°C, while the synthesis temperature is approximately 400°C , although the synthesis temperature varies depending on the process [2]. It is desirable that the overall process, including gasification, gas cleaning and downstream processes, have similar operating temperatures, thus the choice of sulfur sorption materials are important [1]. Even though high temperature gas cleaning of biomass-derived syngas is preferred, only a few methods have been developed for this purpose, namely in-bed sulfur capture and downstream sulfur capture [10].

2.4.2 In-bed Sulfur Capture

Calcium-based sorbents, such as dolomite ($CaCO_3 \cdot MgCO_3$) or limestone ($CaCO_3$), are commonly used for in-bed sulfur capture (or in situ desulfurization) [10]. These materials are naturally available, have low cost and toxicity and can be utilized under conditions that are both reducing and oxidizing. It has been demonstrated that at temperatures higher than 800°C these materials are favorable for H_2S removal [1, 17].

Suitable process conditions and a sorbent that possesses high sulfur capacity is essential to achieve efficient desulfurization. Important factors that have a strong influence on the efficiency are calcination, sintering of the oxide, sulfiding of the calcined sorbents and sintering of the sulfide [10]. Table 2.3 give an overview of reactions regarding decomposition and sulfidation of calcium-based sorbents.

Table 2.3: Decomposition and sulfidation of calcium-based sorbents [10]

Reaction	Reaction equation	Equation number
Calcination	$CaCO_3 \rightarrow CaO + CO_2$	(1.3a)
	$CaCO_3 \cdot MgO \rightarrow CaO \cdot MgO + CO_2$	(1.3b)
Sulfidation	$CaO + H_2S \rightarrow CaS + H_2O$	(1.3c)
	$CaO \cdot MgO + H_2S \rightarrow Cas \cdot MgO + H_2O$	(1.3d)
Side reaction	$CaS + 2O_2 \rightarrow CaSO_4$	(1.3e)

The use of calcium-based sorbents for desulfurization follows equation 1.3c and 1.3d. The equilibrium constant of the calcium-based sorbents regarding these equations is another essential factor to achieve successful in-bed sulfur capture. To ensure low concentration of H_2S, the equilibrium constant need to be sufficiently high [17]. Besides, the concentration of H_2S strongly depends on the reaction temperature and the partial pressure of CO_2 and steam [10].

There are only a few studies on regeneration of spent calcium-based sorbents mainly due to the properties of dolomite and limestone, as they are rather soft and can easily be broken up, resulting in high attrition rate. CaS, which is produced during sulfidation, is unstable and can react further with O_2 to form $CaSO_4$ according to equation 1.3e. Hence, a stable layer of $CaSO_4$ forms on the sorbent surface during regeneration and lead to the loss of active material. Besides, disposal of CaS that is environmentally acceptable requires further stabilization. Due to these reasons, calcium-based sorbents are usually considered for applications not involving regeneration [10, 17]. However, downstream desulfurization is another method focusing on the use of regenerable metal oxide sorbents.

2.4.3 Downstream Sulfur Capture

Downstream desulfurization using regenerable solid sorbents have attracted much attention. Several metal oxide-based sorbents can be utilized for sulfur capture downstream of the gasification process at high temperature. However, the metal oxides possess both advantages and limitations at the same time [10]. Sorption capacity and lifetime of the sorbent are influenced by, amongst other, sintering, poisoning, coking and loss of active material. Therefore, developing a suitable sorbent is important as it can improve the efficiency of regeneration and the sulfur capacity, in addition, remove other contaminants along with sulfur [2].

Materials for Sulfur Removal

Cheah et al.[1] and Westmoreland and Harrison [18] studied a wide range of materials that can be applied as high-temperature solid sorbents (HTSS) for removal of sulfur, of which the mostly studied metal oxides are Zn, Cu, Mn, Fe and Ca.

The concept of high temperature gas cleaning for removal of sulfur through a chemical looping process is illustrated in Figure 2.10. The resulting syngas from biomass gasification enters the sorber where it is cleaned using a solid sorbent. The sulfur present in the syngas is captured by the sorbent through a sulfidation reaction and subsequently regenerated.

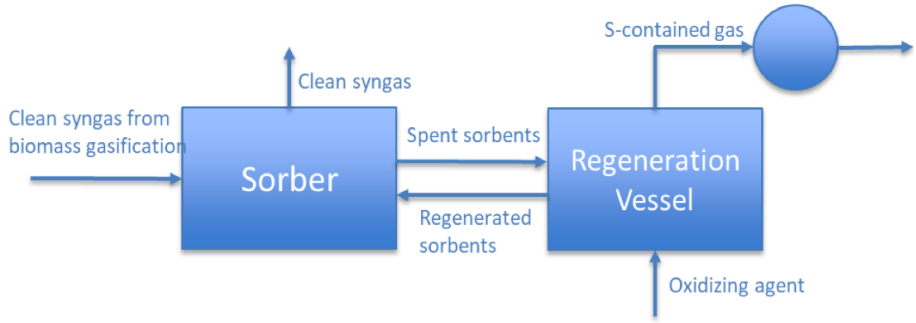

Figure 2.10: Schematic diagram of the concept for chemical looping desulfurization (CLD)

The reaction mechanism for sulfur adsorption with metal oxide-based sorbents are described by a sulfidation reaction (equation 2.2) and a regeneration reaction (equation 2.3). During sulfidation, the metal oxide (MeO) react with hydrogen sulfide (H_2S) to form metal sulfide (MeS) and water. Subsequently, after the sulfur is captured, oxygen is used to regenerate the spent metal sulfide back to metal oxide [19]. However, formation of sulfate during regeneration (equation 2.4) is an undesired side reaction which consequently decrease the desulfurization capacity [20].

$$MeO(s) + H_2S(g) \leftrightarrow MeS(s) + H_2O \tag{2.2}$$

$$MeS(s) + 1/2O_2(g) \leftrightarrow MeO(s) + SO_2(g) \tag{2.3}$$

$$MeO(s) + SO_2(g) + 1/2O_2 \leftrightarrow MeSO_4(s) \tag{2.4}$$

The properties of the most relevant sorbents (Zn, Cu and Mn) are important if to be used for high temperature sulfur removal. However, there are both advantages and disadvantages for each metal oxide. Oxides based on copper can easily be reduced to elemental copper, hence cause sintering. On the other hand copper oxides can provide low levels of H_2S and fast sorption rate. Zinc oxide-based materials have a good sulfur capacity, however these materials are not stable at higher temperatures (>550°C) due to reduction of zinc oxide and subsequent vaporization of elemental zinc. Although copper oxide and zinc oxide have more favorable thermodynamics than manganese-oxide based materials, the latter has good stability at high temperatures due to its resistance against reduction to elemental manganese, which is beneficial considering the reducing environment and high temperatures of biomass gasification. Moreover, manganese-oxide based materials have high sulfur uptake capacity [1]. Several factors

must be considered when selecting sulfur sorption materials. The most important being mechanical stability against attrition and degradation, chemical stability, high sulfur sorption capacity, kinetics and ability to regenerate [1, 21]. Manganese fulfill many of these criteria and are commonly used for processes involving high temperature and steam [15].

Supports are commonly used for optimization of sorbents to enhance their properties. Both supported and unsupported metal oxides have been investigated for high-temperature desulfurization, of which supported metal oxides are more beneficial as they increase the reaction rate, provide a large surface area where the metal oxide can be dispersed and have good stability. However, the adsorption capacity can be slightly reduced when using supported metal oxides [22].

Promoters are commonly used to improve catalyst performance and the activity of active sites. Zirconium oxide is a common promoter due to enhanced performance in steam-containing environments, high stability and can provide high surface area [23, 24, 25]. Thus, in the present work zirconium oxide was applied to improve the manganese-based sorbent.

As mentioned, there are several issues regarding sulfur-containing species generated from the gasification process when converting biomass to biofuels. To solve these problems high-temperature gas cleaning is applied. The present work aims to optimize manganese-based sorbents with zirconium oxide. Moreover, study the effect of Zr-loading, calcination temperature and preparation method on the sorbents desulfurization performance after multiple sorption- and regeneration cycles. Different characterization techniques are applied to characterize fresh and reacted sorbents.

Chapter 3

Theoretical Concepts of Experimental Methods

3.1 Sorbent Preparation

3.1.1 Incipient Wetness Impregnation

Impregnation methods are commonly used for deposition of metal particles onto the support. The incipient wetness impregnation method involves a support, which has been dried beforehand, being brought in contact with a precursor solution of equal volume as the support pore volume. Subsequently, the precursor solution is drawn into the pores by capillary forces, filling up the pores such that no excess of precursor solution is remaining outside the pore space. This requires air to be eliminated from the pores. The capillary pressure becomes greater than the pressure of air inside the pores in the case of very small pore radius, which lead to the dissolving of air in the liquid. Another outcome is that air escapes through greater pores. In cases where the support cannot withstand bubbles due to poor mechanical strength, the impregnation should be done under vacuum. Then the support is dried so that the solvent evaporates, and the active metal can be deposited into the pores of the support [26].

3.1.2 Co-precipitation

The co-precipitation method involves one or several metals that are being precipitated along with a support and/or a precursor [27]. A flowchart of this preparation method including precipitation, filtration, washing, drying and calcination is given in Figure 3.1.

During the precipitation step, a precipitation agent is added to the solution containing the precursor compounds, resulting in precipitation of the precursors as hydroxide crystallites. Addition of a precipitation agent increases the pH which gives a highly supersaturated solution. Constant mixing should be applied to ensure a homogeneous solution, hence allow both metals to precipitate simultaneously [28]. After a complete precipitation, the product is filtered to separate the mixture of hydroxide metal salts from the residue. Further, drying and calcination of the precipitate are necessary to achieve an active catalyst [27].

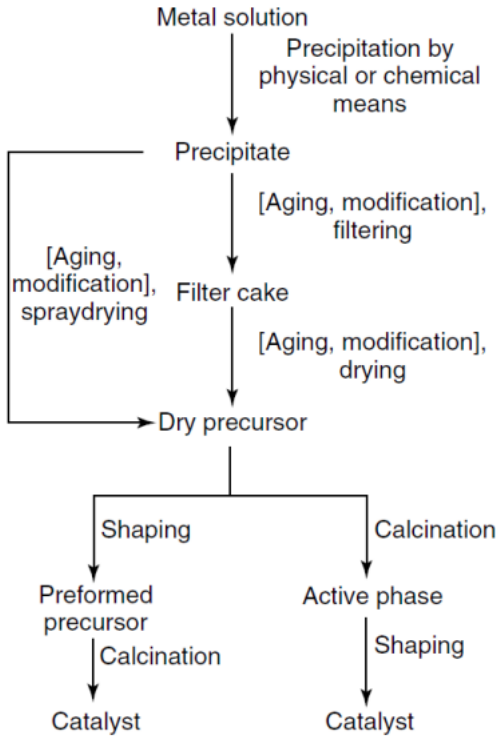

Figure 3.1: Flowchart for preparation of a precipitated catalyst [29].

The co-precipitation method is considered to be more challenging compared to the impregnation method and requires more precise control of process conditions. Hence this method is costly due to use of more advanced equipment. Process conditions such as ingredients, the method of dosing, stirring and mixing have a significant effect on the final product and its size, shape, pore structure, dispersion and surface area [27].

3.2 Characterization Methods

The sorbents were characterized by nitrogen adsorption, temperature programmed reduction (TPR), X-ray diffraction (XRD) X-ray fluorescence (XRF) and scanning electron microscope (SEM). Sorbent capacity was tested using a designed laboratory set-up consisting of gas supply and metering system, a quartz fixed bed reactor and an analysis section including a quadrupole mass spectrometer to observe the H_2S concentration.

3.2.1 Nitrogen Adsorption

Gas adsorption is a widely used method for characterization of porous solid materials, where usually nitrogen is used as the adsorptive gas at a temperature of 77 K. From nitrogen adsorption both surface area, pore size distribution and pore volume of the materials can be determined [30, 31].

77 K is the liquid nitrogen temperature, and at this temperature nitrogen can form multilayer adsorption. The Brunauer-Emmett-Teller (BET) method is based on multilayer adsorption and used for determination of surface area [32]. The method is a generalization of the Langmuir theory, which has the assumption of monolayer molecular adsorption. Other Langmuir assumptions are immobile adsorption, homogeneous surface (heat of adsorption is independent of the coverage) and dynamic equilibrium between a gas phase and adsorbed species [33].

Degassing of the solid samples to remove any contaminants is necessary before determining the surface area. This can be done by applying vacuum, heat, or flowing dry gas. Cooling of the solid is then done under vacuum to cryogenic temperature (77 K). Nitrogen is successively added to the solid, and after each dose of nitrogen the pressure is allowed to attain equilibrium and the amount adsorbed can be calculated [32]. Adsorption of a gas by a porous material is described by an adsorption isotherm which is defined by the amount of adsorbed gas at a set temperature as a function of pressure [34].

Equation 3.1 shows the adsorption isotherm equation developed by Brunauer, Emmett and Teller [33].

$$\frac{P}{V(Po-P)} = \frac{1}{VmC} + \frac{(C-1)}{VmC} \cdot \frac{P}{Po} \tag{3.1}$$

Where:

- P: partial vapour pressure of nitrogen [Pa]
- Po: saturated pressure of nitrogen at the adsorption temperature [Pa]
- V: volume of adsorbed nitrogen gas [ml]
- Vm: volume of adsorbed nitrogen gas at monolayer coverage [ml]
- C: dimensionless BET constant

In the BET plot, $\frac{P}{V(Po-P)}$ are plotted against $\frac{P}{Po}$ which yield a straight line. The slope is equal to $\frac{(C-1)}{VmC}$ and the intercept is equal to $\frac{1}{VmC}$ [30]. This can be used to calculate the volume of adsorbed nitrogen gas at monolayer (Vm) where $\frac{1}{(slope+intercept)}$ gives Vm, and (1 + $\frac{slope}{intercept}$) gives the BET constant, C [30].

Barrett, Joyner and Halenda (BJH) method are used to determine pore volume and pore size distribution based on the Kelvin equation (equation 3.2 [35]), which describes the desorption isotherm [31].

$$ln(\frac{P}{P_0}) = -\frac{2\gamma V_L}{RTr_m} \tag{3.2}$$

Where:

- P: measured pressure
- P_0: saturated pressure
- γ: surface tension of liquid adsorbate
- V_L: molar volume of liquid adsorbate
- R: gas constant
- T: absolute isothermal temperature
- r_m: mean pore radius

IUPAC conventions commonly classify the pore size of porous materials and adsorption isotherms with correlated hysteresis loops. Figure 3.2 shows the six types of adsorption isotherms, each having a specific shape that is characteristic for different adsorbents. Type I indicates microporous adsorbents, whereas nonporous or macroporous adsorbents are of type II and III, and mesoporous adsorbents are of type IV and V. Not so common is type VI isotherm, which indicates a surface that is highly uniform with stepwise adsorption of layers [34].

Figure 3.3 shows the hysteresis loops of adsorption and desorption branches, where the shape of the hysteresis loop give information about the pore structure. The characteristic of H1 hysteresis loop is the parallel adsorption and desorption branches, and the mesopores tend to have narrow pore size distribution. For the H2 type, the loop is wider with a steeper desorption curve compared to the adsorption curve, giving a more complex pore structure. A non-rigid pore structure is characteristic for H3 and H4 hysteresis loops, either between particle grains or flat plates, respectively. This is characterized by lack of a plateau at $P/P_0 = 1$ and the absence of overlapping adsorption and desorption branches [36, 37].

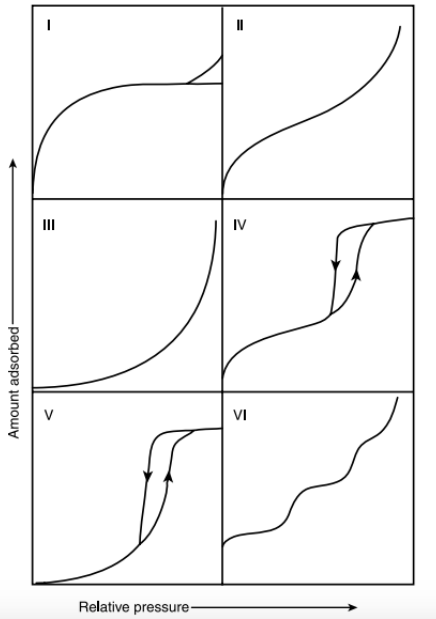

Figure 3.2: Classifications of physisorption isotherms by IUPAC [34]

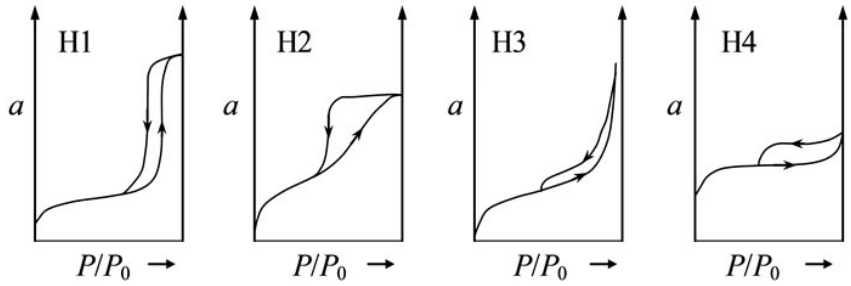

Figure 3.3: Classifications of adsorption-desorption hysteresis loops by IUPAC [36]

3.2.2 X-Ray Diffraction (XRD)

X-ray diffraction is a technique used to identify the phase of crystalline substances. It can also provide information about structural properties such as particle size [30].

The technique is based on constructive interference where a beam of monochromatic X-rays interacts with the crystalline substance, leading to diffraction of X-rays by the atoms within the substance. This interference effect gives a diffraction pattern with structural information or phase identification of the crystalline substance. Constructive interference of diffracted X-rays by crystals is described by Bragg´s Law, which is given in equation 3.3 [30].

$$n\lambda = 2d_{hkl} \cdot sin\theta_{hkl} \tag{3.3}$$

Where:

- n: An integer named as the order of reflection
- λ: Wavelength of the X-ray
- d: Distance between two lattice planes
- θ: Incident angle (angle between incoming X-rays and the lattice plane)

By measuring 2θ, which are the angles of maximum intensity and where constructive interference appears, one can get the distance between the lattice planes (hkl), as shown in Figure 3.4 [30, 38].

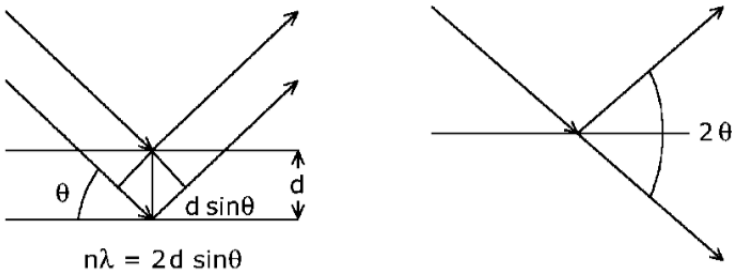

Figure 3.4: Constructive interference of X-rays scattered by atoms in in an ordered lattice [30]

The Scherrer formula is given in equation 3.4 and provides an estimate of the crystallite particle size related to line width [30, 38]:

$$L = \frac{k\lambda}{\beta cos\theta} \tag{3.4}$$

Where:

- L: Crystallite particle size
- λ: Wavelength of X-ray
- θ: Diffraction angle
- β: Peak width at half-peak height (FWHM)
- k: shape factor (k=0.9 for FWHM (full width at half maximum) [39])

As it can be seen from the formula, an increase in the crystallite size, L, result in a decrease of the peak width of an XRD line, β. This means that the larger the crystals are, the sharper the peaks will be.

3.2.3 Temperature Programmed Reduction (TPR)

Temperature programmed reduction is a commonly used technique to characterize the reducibility of catalysts, typically metal oxides, mixed metal oxides or supported metal oxides, by monitoring a chemical reaction as the temperature increases [30, 40, 41].

This technique involves flowing a reducing gas mixture over the reducible catalyst while raising the temperature linearly with time at a heating range of typically 0.1 to 20 °C /min [30]. The reducing gas mixture is usually H_2 /Ar or H_2 /N_2 [41]. A furnace is used to heat the reactor, while a thermal conductivity detector (TCD), or a mass spectrometer, is used for determination of the hydrogen consumption at the outlet of the reactor [30, 41]. During the reduction of the metal catalysts, hydrogen is consumed to produce water. It is important to remove the water before the gas mixture enters the TCD to achieve a quantitative signal. Hence, the set-up consists of a trap where water is condensed [40]. The metal catalysts are reduced according to equation 3.5:

$$M_xO_y + yH_2 \rightarrow xM + yH_2O \tag{3.5}$$

Where M_xO_y are the metal oxide [40]. However, reduction can only occur if the enthalpy change of the reaction (equation 3.6) is less than zero:

$$\Delta G = \Delta G^0 + n \cdot RT\ ln\ \frac{P_{H_20}}{P_{H_2}} < 0 \tag{3.6}$$

The temperature of reduction is different between noble metals and non-noble metals, and the more noble metal is, the easier the reduction is, and a higher water/hydrogen ratio can be acceptable [30].

A graphical representation of a TPR profile for a metal oxide is presented in figure 3.5. The temperature at the maximum point of the peak represents the temperature at which the reduction rate is highest. Total hydrogen gas consumed during the reduction is represented as the area under the TPR curve, which can be calculated by integration [30, 40].

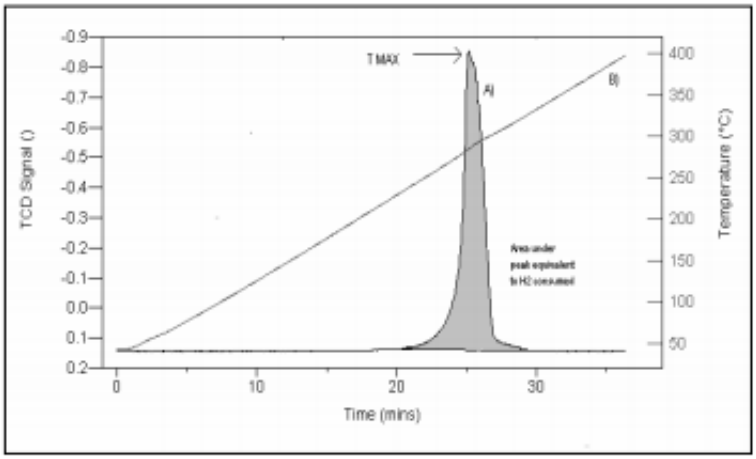

Figure 3.5: Temperature programmed reduction (TPR) profile for a metal oxide. A) presents the TCD signal output as a function of time. B) presents the temperature as a function of time. [42]

It is also possible to calculate the hydrogen uptake in a TPR experiment by doing a pulse calibration. In pulse calibration the TCD signal is calibrated with a known volume of hydrogen gas, which then provides reference values on the TPR plot, hence the amount of consumed gas can be calculated.

3.2.4 X-Ray Fluorescence (XRF)

X-Ray fluorescence (XRF) analysis is a spectroscopic technique used to determine the composition of a sample, either powders, bulk solids or liquids. The technique is quick and non-destructive.

Conventional XRF instruments are based on wavelength dispersive spectrometers where an X-ray tube is used to excite the sample, and the characteristic fluorescent X-ray spectrum for the specific sample is detected by an x-ray spectrometer. A principal diagram of a wavelength dispersive X-ray fluorescence spectrometer is shown in Figure 3.6 [43].

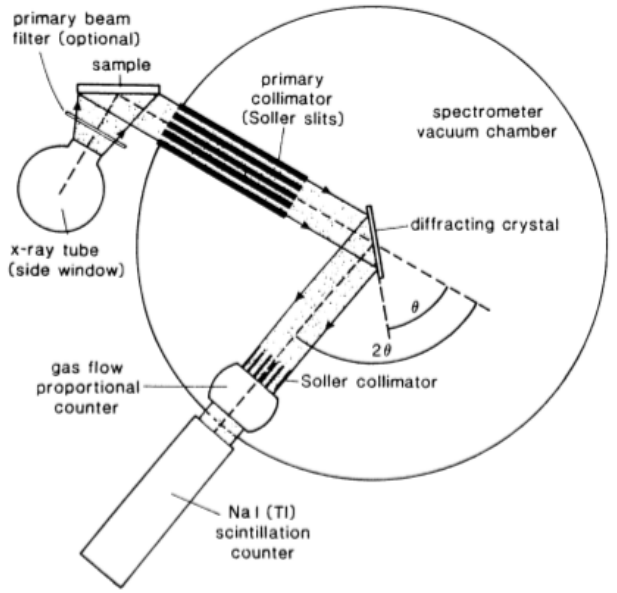

Figure 3.6: Principal diagram of a wavelength dispersive X-ray fluorescence spectrometer [43]

The source of the X-ray tube can include palladium (Pd) or other metals with a high melting point such as rhodium (Rh) and iron (Fe). After the sample has been excited to X-ray fluorescence by the X-ray tube, the X-rays are converted into electronic signals by a detection system, which determines the characteristic radiation emitted from the sample [44].

Atoms are composed of a nucleus, which is positively charged and consist of both protons and neutrons, and electrons surrounding the nucleus as orbital shells (K, L, M, etc.) as shown in Figure 3.7 [43].

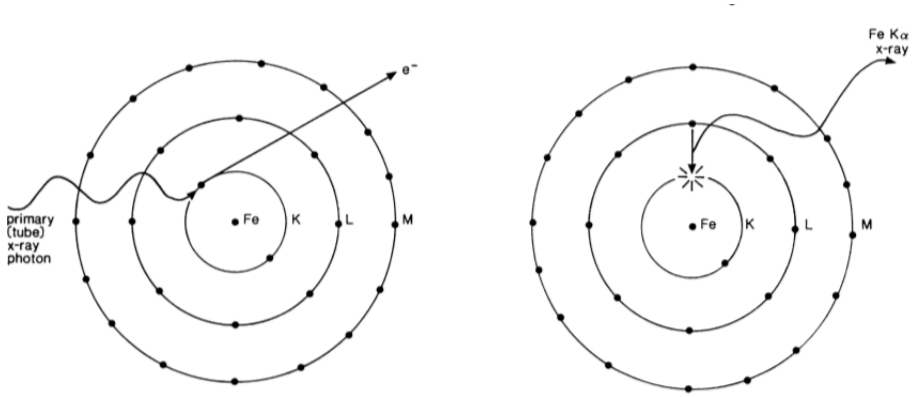

Figure 3.7: The structure of an atom is described by a simplified model after Bohr, showing the concept of X-ray fluorescence [43]

A sample that is illuminated with high energy photons (X-rays) generates the ejection of electrons from the inner orbital shell (K), producing an ion. The electron vacancy is instantly filled by another electron that drops down from the higher energy shell (L), releasing energy that corresponds to characteristic fluorescent X-rays [44].

3.2.5 Scanning Electron Microscope (SEM)

Scanning electron microscopy (SEM) is a technique used to provide information about chemical composition, microstructure, morphology and topography of a sample [45, 46]. A principle design of a scanning electron microscope is presented in Figure 3.8.

A beam of high-energy electrons is scanned across the sample surface, and the interaction that occurs between the sample and the electron beam generates a variety of signals, as shown in Figure 3.9 [46]. X-ray or Auger electron spectra can be used to get information about the sample composition, while secondary electrons (SE) and backscattered electrons (BSE) are used to form SEM images. The reflection of secondary electrons occurs close to the specimen surface and can give information about the sample topography. Backscattered electrons are reflected from deeper inside the sample and based on compositional contrast these electrons can give information about the different elements present in the sample. The reflection of backscattered electrons depends on the atomic number of the specimen, where high atomic number gives a high backscattering signal due to high positive charges, resulting in more electrons that are backscattering. This will appear as brighter areas in an SEM image [46, 47].

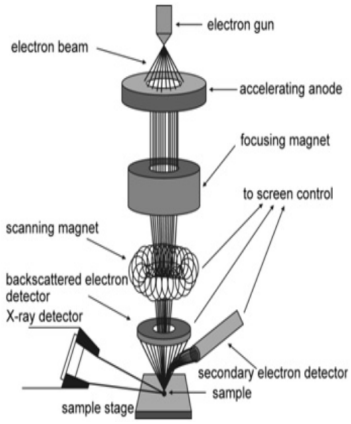

Figure 3.8: Principle design of a scanning electron microscope [48].

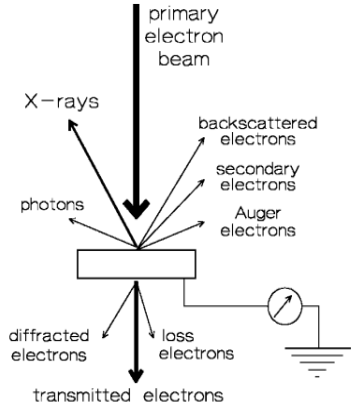

Figure 3.9: Different signals detected after interaction between the sample and the primary electron beam [45].

3.3 Laboratory Setup

A flowsheet of the laboratory setup used for sorption-regeneration measurements is shown in Figure 3.10. The setup consists of gas supply and metering system, a quartz fixed bed reactor and an analysis system including a quadrupole mass spectrometer. Hydrogen gas, nitrogen gas and pure air from the gas distribution line are connected to the setup, whereas a cylinder containing hydrogen sulfide gas (1% H_2S in Ar) is placed inside the setup enclosure and connected. To control the gas flows the setup is equipped with mass flows controllers which are specific for each of the gases. A 100 mL soap bubble meter was used for the calibration of the mass flow controllers, and the resulting calibration curves are given in Appendix C. A tubular quartz reactor containing the sorbent bed is surrounded by aluminum blocks and a furnace that is connected to a temperature regulation system. A bypass line is used for stabilization of gases when changing from sorption to regeneration and a quadrupole mass spectrometer is used to monitor the H_2S concentration.

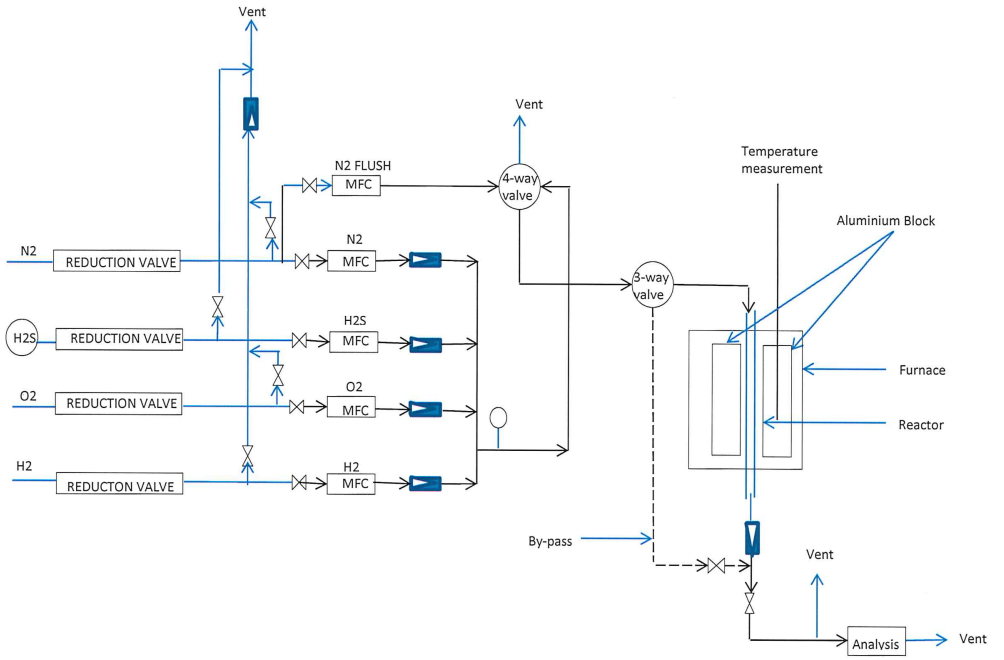

Figure 3.10: Schematic diagram of the laboratory setup used for sorption and regeneration experiments [3]. The setup consists of a gas supply and metering system, a quartz fixed bed reactor and an analysis system including a quadrupole mass spectrometer to measure gas concentration.

Chapter 4

Experimental

A risk evaluation associated with the sorbent preparation and laboratory work during this master´s thesis was performed. The risk assessment is attached to Appendix A.

4.1 Sorbent Preparation

A series of ZrO_2-modified Mn/γ-Al_2O_3 sorbents were prepared using two different preparation methods: incipient wetness impregnation (IWI) and co-precipitation (CP). Constant loading of 15wt% Mn was used for both methods. The sorbents prepared by IWI were promoted with 1wt%, 5wt% and 10wt% Zr, and for the sorbents prepared by CP the Zr loading was 1wt% and 10wt%. In addition, a reference sorbent of pure manganese oxide supported on alumina (Mn/γ-Al_2O_3) was prepared for comparison.

Fresh sorbents are denoted with a prefix ZrX, where *X* indicates Zr-loading, followed by *Mn15*, which indicates the constant nominal Mn loading. The support are indicated by */support name*, e.g. Zr1-Mn15/Al_2O_3. Reacted sorbents after 10 cycles of sorption and regeneration are denoted with an additional affix *-AR*; e.g. Zr1-Mn15/Al_2O_3-AR.

Manganese nitrate tetrahydrate ($Mn(NO_3)_2 \cdot 4H_2O$, ≥ 97.0%, Sigma-Aldrich) and zirconyl nitrate solution ($ZrO(NO_3)_2$, 35 wt.% in dilute nitric acid, ≥ 99%, Sigma-Aldrich) were used as metal precursors, and alumina (Al_2O_3) as support. The prepared sorbents were then calcined at both 500°C and 700°C for 5 hours using a calcination setup with air flow. The heating rate used was 5 °C/min. An overview of the prepared sorbents used in this study is presented in Table 4.1.

Table 4.1: List of prepared sorbents

Sorbent	Preparation method	Active part		Support		Promoter		Calcination temp.	
		Comp.	Content [wt.%]	Comp.	Content [wt.%]	Comp.	Content [wt.%]		[°C]
Al2O3	IWI			Al2O3	100			500	700
Mn15/Al2O3	IWI	Mn	15	Al2O3	85			500	700
Zr1-Mn15/Al2O3	IWI	Mn	15	Al2O3	84	Zr	1	500	700
Zr5-Mn15/Al2O3	IWI	Mn	15	Al2O3	80	Zr	5	500	700
Zr10-Mn15/Al2O3	IWI	Mn	15	Al2O3	75	Zr	10	500	700
Al2O3	CP			Al2O3	100			500	700
Mn15/Al2O3	CP	Mn	15	Al2O3	85			500	700
Zr1-Mn15/Al2O3	CP	Mn	15	Al2O3	84	Zr	1	500	700
Zr10-Mn15/Al2O3	CP	Mn	15	Al2O3	75	Zr	10	500	700

IWI: Incipient wetness impregnation
CP: Co-precipitation

4.1.1 Incipient Wetness Impregnation

Before impregnation, the support (γ-Al_2O_3, 96%, Strem Chemicals) was pretreated by calcination at 500°C for 10 hours using a calcination setup with air flow. The heating rate used was 10°C/min.

After the pretreatment, the capacity (pore volume) of the support was determined empirically. 1 gram of support was weighed out and a micropipette was used to add distilled water (1.3 mL) to the support. The required amount of distilled water depends on the support and how much of the distilled water it can absorb.

The next step involves dissolving the required amount of metal precursor in the distilled water. In this case, it is essential to take into account that the Mn- and Zr-precursor contains water. It is, therefore, necessary to do a correction of the volume by subtracting the amount of water in the salt from the volume of distilled water for the support.

The desired amount of support was weighed out and placed in a crucible. The support was then impregnated by the solution containing the metal precursors, using a plastic pipette to step wisely add small amounts of the solution. The solution was homogeneously distributed over the support and a glass rod was used to stir between each adding of the solution. Finally, when all the dissolved precursor was added, the impregnated support was stirred for 30 minutes.

Parafilm was used to cover the crucible and left at room temperature for 24 hours. The samples were then dried for 24 hours in an oven at 100°C, before calcined at 500°C and 700°C, using a calcination setup with air flow.

Sorbents to be used in H_2S sorption studies and characterized by nitrogen adsorption need to have a particle size between 150-250 μm. This is achieved by crushing the calcined sorbents using a hydraulic press at 10 tons for 30 minutes to provide pellets, followed by crushing of the pellet using mortar and pestle before sieved to the desired size.

4.1.2 Co-precipitation

For the preparation of manganese oxide-based sorbents using co-precipitation, $Al(NO_3)_3 \cdot 9H_2O$ (≥ 98.5%, Merck) was used to function as a support, and the composition was kept the same as for sorbents prepared by incipient wetness impregnation. Na_2CO_3 (≥ 99.5%, VWR) and NaOH (≥ 99%, VWR) were used as precipitating agents. Calculations for this process are given in Appendix B.2.

A solution of Na_2CO_3, NaOH and distilled water were mixed before added into a reactor consisting of a thermocouple and a mechanical stirrer. Subsequently, a nitrate solution of Mn, Zr and Al precursor salts together with distilled water were mixed and slowly added (for a period of 2 h) to the first solution under constant stirring. Diluted nitric acid was then used to adjust the pH between 9 and 10 before heated for 16 h at 353 K. The resultant precipitate (or bed) was filtered and thoroughly washed with distilled water before dried at 90°C using a high-temperature furnace, and finally calcined under desired conditions.

4.2 Nitrogen Adsorption

To obtain textural properties of the fresh and reacted sorbents, nitrogen adsorption measurements were performed using the Micromeritics TriStar II 3020 Surface Area and Porosity Analyzer. For the pretreatment part, the VacPrep 061 Degasser unit was used. Brunauer-Emmett-Teller (BET) method was applied to measure specific surface area, and pore size and pore volume were measured by the Barrett-Joyner-Halenda (BJH) method were used.

Clean cotton gloves were used when handling the sample glass tubes to avoid leaving any fingerprints. The empty sample tubes were weighed before a known amount of sample (~100 mg) was added and the new weight was recorded. The samples were then pretreated and left under vacuum overnight at 200°C. When the pressure of the degassing is 100torr or less the samples are ready for analysis. The samples are then cooled and the mass change after degassing are recorded before installing into the instrument, evacuated and cooled by liquid nitrogen.

4.3 X-Ray Diffraction (XRD)

Bruker D8 Advance DaVinci X-ray Diffractometer with CuKα radiation (λ = 0.154060 nm) was used to identify the phases present within the fresh and reacted sorbents. XRD patterns for the support was also obtained.

The analysis was performed on powder samples with a 2θ range of 5-75 degrees for 60 minutes using V6 divergence slit.

A standard RDB database (PDF-4+2016) was used to identify the peaks on the produced diffractograms using the Diffrac.Suite EVA software. The same software was also used to determine the crystallite size as the full width at half maximum (FWHM) for the active phase using the Scherrer equation.

4.4 Temperature Programmed Reduction (TPR)

TPR measurements were performed to obtain reduction profiles for all the fresh sorbents using a BenchCAT Hybrid 1000 HP instrument.

Approximately 100 mg sample was weighed out and placed in a U-shaped quartz reactor. To ensure that the sample was kept in place, a layer of quartz wool was placed at the bottom and on top of the sample in the reactor before connected to the TPR equipment. To measure the bed temperature a thermocouple was placed close to the sample (above) and a furnace was used to heat the reactor containing the sample. The dissecant (drierite, 1g) in the water trap is to be changed if necessary, and before continuing with the analysis a leak test was carried out.

For the pretreatment, the samples were heated to 350°C using argon as the inert treatment gas at a flow rate of 50 ml/min. The temperature ramp rate was set to 10°C/min. The samples were held at final setpoint temperature (350°C) for 30 minutes before cooled down to 50°C.

For the TPR measurements, a reducing gas mixture containing 10% hydrogen in argon with a flow rate of 50 ml/min was used. A temperature interval from 50°C to 800°C was studied using a heating rate of 10°C/min. A thermal conductivity detector (TCD) measured the concentration of hydrogen in the outlet gas from the reactor.

4.5 X-Ray Fluorescence (XRF)

The Wavelength Dispersive X-Ray Fluorescence (WDXRF) Supermini200 Analyser was used for elemental analysis of fresh sorbents.

Approximately 200 mg of sample was mixed with approximately 3 g of boric acid (binder) and crushed by hand for 10 minutes using mortar and pestle to obtain a homogeneous mixture. The mixture was then pelletized using a hydraulic press at 10 tons for minimum 4 minutes before placed in a sample retainer and covered with polypropylene film. 3 pellets from the same batch were made to ensure reproducibility. The samples were then loaded into the instrument.

4.6 Scanning Electron Microscope (SEM)

SEM Apreo was used to study the morphology of the sorbent surface.

Small amounts of each sample (powder) was attached to a specimen stub using an adhesive (double-sided copper tape) to ensure good conductivity. One spot on each sample was chosen for imaging at different magnifications.

4.7 H_2S Sorption and Regeneration Experiments

The designed laboratory setup was used to measure the sulfur capacity of various sorbents after multiple sorption-regeneration cycles and consists of a gas supply and metering system, a quartz fixed bed reactor and an analytical system consisting of a Thermostar GSD 320 T1 C. The latter is equipped with a quadrupole mass spectrometer using a SEM detector for measurements of H_2S concentration. A thermocouple was placed close to the sorbent bed on the outer wall of the quartz reactor to observe changes in the temperature, and Bronkhorst mass flow controllers (MFC) was used to control the gas flows.

The experiment was carried out in a tubular quartz reactor at atmospheric pressure. A description of the process is given in Figure 4.1. Approximately 200 mg of sorbent (150-250 μm) was used for the analysis. The sorbent was reduced prior to the sorption experiment using a mixture of H_2 (25vol%) and N_2 (25vol%), and a leak test was performed. During the reducing step, the sorbent was heated to sorption temperature followed by 1 hour stabilization. Subsequently, the system was flushed with N_2 which required another 30 minutes of stabilization (bypass) before starting the sorption experiment. For the sorption experiment a total flow of 100 ml/min (40vol% H_2, 20vol% N_2, 0.4vol% H_2S and 39.6vol% Ar) was used at 600°C. Soon after breakthrough was achieved the sorption measurements were stopped. The regeneration experiment was performed at 650°C with a total flow of 100 ml/min using a mixture of pure air (25vol%) and nitrogen (75vol%). The regeneration lasted for 15-20 minutes. Both sorption and regeneration were performed at a pressure of 2 bar. A total flow of 25 ml/min (12.5vol% H_2 and 12.5vol% N_2) at sorption temperature was used whenever the sorbent was left overnight, which in this study refers to cycle 5.

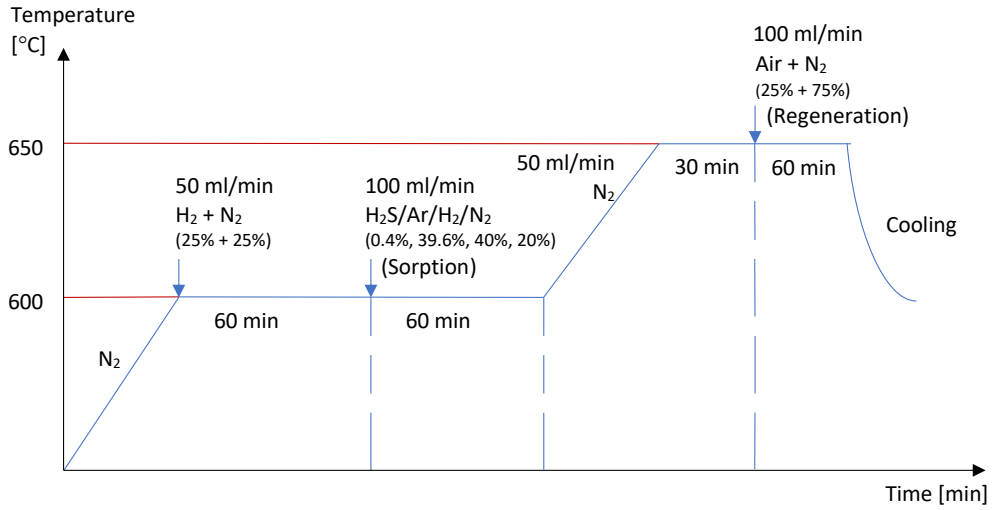

Figure 4.1: Procedure for sorption-regeneration experiment using a designed laboratory set-up consisting of a gas supply and metering system, a quartz fixed bed reactor and an analysis section including a quadrupole mass spectrometer to measure the H_2S concentration.

H_2S Sorption Capacity

A quadrupole mass spectrometer was used to monitor the H_2S concentration, and the changes in gas concentration present the use of ion current measurements. By assuming a linear relationship between the ion current signal and H_2S concentration (Figure 4.2) equation 4.1 is obtained, hence ion current (IC) can be converted to concentration.

$$IC = a \cdot [C] + b \tag{4.1}$$

Two ion current signals are obtained (0 ppm and 4000 ppm). The ion current for 0 ppm is obtained from the reducing step after 30 minutes stabilization with pure N_2 and H_2, whereas the ion current for 4000 ppm, which indicates the maximum ion current, is obtained after 30 minutes stabilization of the gas mixture for H_2S sorption.

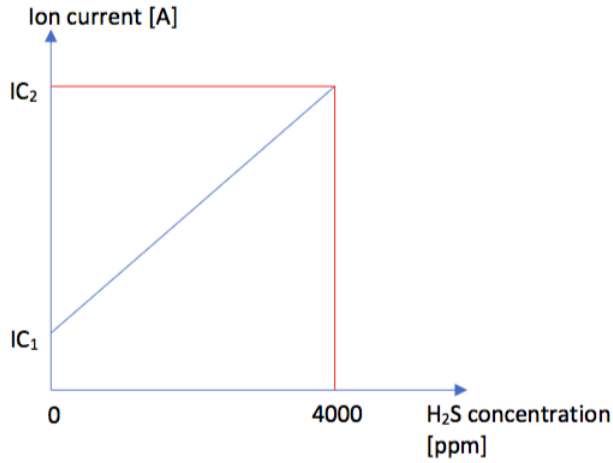

Figure 4.2: Linear relationship between the ion current signal and concentration of H_2S.

The amount [mL] of H_2S removed can be calculated based on the concentration of H_2S. Further, the molar volume can be found from equation 4.2 and equation 4.3 by assuming ideal gas. Under a certain temperature and pressure, the molar volume of a gas indicates the volume occupied by 1 mol of that particular gas. As a result, the total amount [mol] of H_2S adsorbed by the sorbent is obtained.

$$V_m = \frac{V}{n} \tag{4.2}$$

$$PV = nRT \tag{4.3}$$

At T=20°C and P= 1 atm the molar volume, V_m = 24.04 L/mol.

The H_2S sorption capacity refers to amount H_2S removed before breakthrough of the sorbent (equation 4.4). The point of breakthrough is when the H_2S concentration in the reactor increase after a complete saturation by the sorbent.

Maximum efficiency refers to the theoretical value of H_2S removal and is defined as the amount H_2S to achieve full conversion of MnO and H_2S to MnS. The molar ratio of MnO to H_2S is 1, according to sulfidation reaction (equation 2.2). The theoretical efficiency is calculated from equation 4.5.

Usage efficiency is defined as amount H_2S per gram MnO in sorbent (equation 4.6). It is used to describe how efficient H_2S is removed by the sorbent relative to the theoretical H_2S removal value. Amount of MnO in sorbent is found by equation 4.7.

$$\text{Breakthrough capacity} = \frac{\text{mmol } H_2S}{\text{g sorbent}} \tag{4.4}$$

$$\text{Theoretical efficiency} = \frac{1 \text{ mol } H_2S * \text{Mm } H_2S}{1 \text{ mol MnO} * \text{Mm MnO}} = \frac{34}{71} \tag{4.5}$$

$$\text{Usage efficiency} = \frac{\text{g } H_2S}{\text{g MnO}} \tag{4.6}$$

$$\text{Mol MnO in sorbent} = \frac{\text{g sorbent} \cdot \text{g Mn}}{\text{Mm Mn}} \tag{4.7}$$

Chapter 5

Results and Discussion

In this chapter, the H_2S sorption data obtained for Zr-promoted Mn/Al_2O_3 sorbents are presented. Furthermore, the sorption performance for unmodified Mn/Al_2O_3 (reference sorbent) is used for comparison to see the effect of using Zr as a promoter. The data are mainly based on sorbents prepared by incipient wetness impregnation. In addition, a selection of sorbents has been prepared by co-precipitation for comparison, of which H_2S sorption data have been obtained for one of these sorbents (pure manganese oxide supported on alumina). All sorbents were calcined under two different temperatures to study the influence of heat treatment on sorption performance, as well as textural and structural properties.

Different characterization methods were used to assess the properties of the different sorbents before and after multiple sorption and regeneration cycles. Textural properties of the sorbents were obtained by nitrogen adsorption, and their elemental composition was studied by X-ray fluorescence. X-ray diffraction was used for manganese oxide phase identification and estimation of particle size. The reduction profiles of fresh sorbents were studied by temperature programmed reduction, and scanning electron microscopy was used to study morphology on a selection of fresh and reacted sorbents.

5.1 H_2S Sorption Experiments

One sorption experiment was performed for each of the prepared sorbents to investigate the sorption capacity and stability throughout ten (10) sorption and regeneration cycles. In addition to the sorption and regeneration step, nitrogen was used to flush the sorbents before and after sorption. At the beginning of a new experiment (cycle 1), the sorbent was reduced in a gas flow of H_2 and N_2. Each experiment was done in two days, were cycle 1-4 were completed the first day, and cycle 5-10 the following day.

It should be mentioned that only one H_2S sorption experiment was performed for the reference sorbent ($Mn15/Al_2O_3$) prepared by co-precipitation due to changes and new installations on the laboratory setup, hence limited time to complete experiments for the Zr-promoted sorbents. However, all sorbents prepared by incipient wetness impregnation have been analyzed.

Before sorption, the sorbent stabilizes by flowing through a bypass line. Subsequently, H_2S is captured by the sorbent during sorption, which can be seen as a drop in concentration. When the sorbent becomes fully saturated, it can no longer remove more H_2S. Hence the H_2S concentration begins to increase again (breakthrough). The concentration increases until it reaches the same level as the inlet gas concentration which indicates complete reaction, as shown in Figure 5.1. However, the results from the present study do not illustrate a complete reaction as the sorption experiments were stopped shortly after saturation as indicated in Figure 5.2.

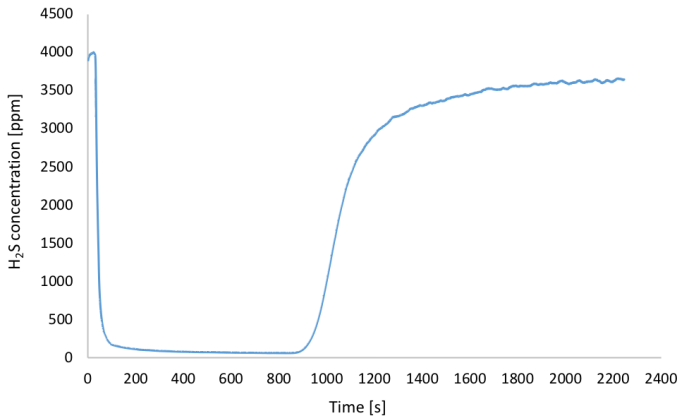

Figure 5.1: H_2S concentration breakthrough measurements during sulfidation for Zr1-$Mn15/Al_2O_3$. The sorbent has been prepared using incipient wetness impregnation and calcined at 600°C (result obtained from specialization project fall 2017).

One sorbent is selected as an example to show the procedure of converting the raw data to sorption capacity. Figure 5.2 include the raw data obtained from H_2S sorption measurements on Zr1-Mn15/Al_2O_3 for all ten cycles, and illustrates the development of breakthrough curves. In agreement with the supervisor, the raw data from H_2S sorption experiments are not included in Appendix. However, all data are handed over to the supervisor for future work.

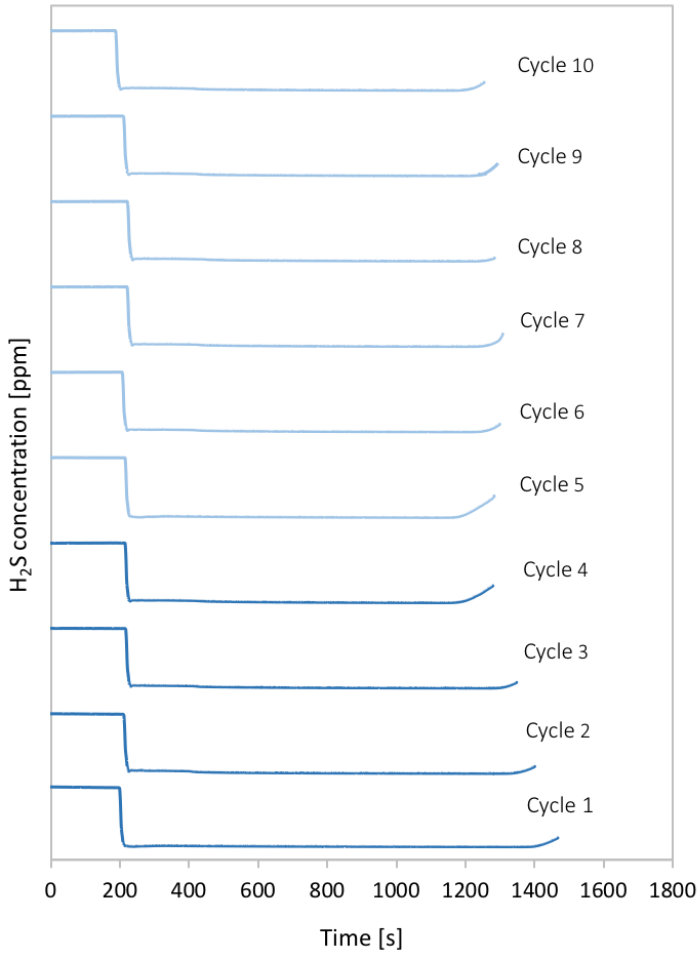

Figure 5.2: H_2S sorption breakthrough measurements on Zr1-Mn15/Al_2O_3 (1wt% Zr, 15wt% Mn). The sorbent has been prepared using incipient wetness impregnation and calcined at 700°C. The first 4 cycles were done on day one, whereas the remaining 6 were completed the following day.

The H_2S sorption capacity can be found by first converting the raw data, which comprise H_2S ion current, to H_2S concentration as illustrated in Figure 5.3 (a)-(b). This is done by using the linear assumption (equation 4.1) described in section 4.7. Subsequently, the curve is simply turned as illustrated in Figure 5.3 (c). The amount of H_2S removed by the sorbent can then be found by converting the concentration [ppm] to volume [mL] (Figure 5.3 (d)), and further use the assumption of ideal gas to find the total amount of H_2S [mol], see calculations in Appendix D.

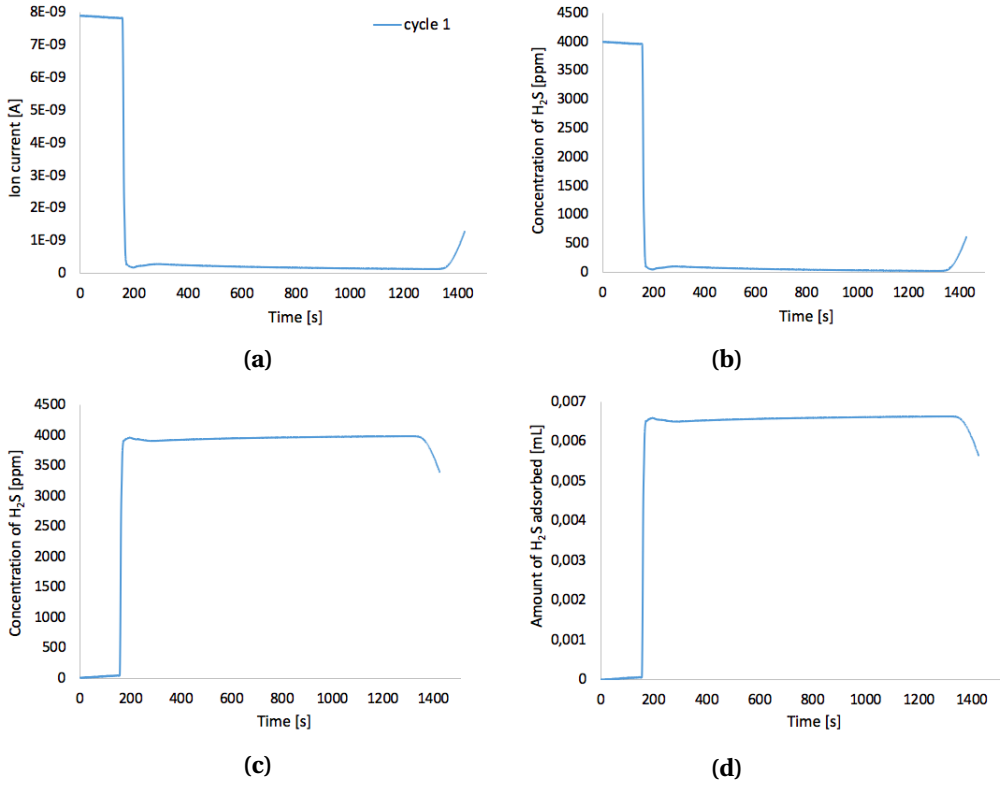

Figure 5.3: The process of converting the raw data from H_2S sorption measurements to get the amount of H_2S adsorbed by the sorbent. (a): Raw data from mass spectrometer showing H_2S ion current as a function of time; (b): H_2S concentration as a function of time; (c): H_2S concentration as a function of time; (d): amount of H_2S adsorbed by the sorbent

During sulfidation a significant drop in H_2S concentration occur, followed by a minor increase in concentration before it subsequently decreases again and keeps stable throughout the sulfidation. This is indicated in Figure 5.4. The lowest concentration is assumed to be a constant level and used when calculating the point at 4000 ppm. This behavior is suggested to be due to H_2S as it has a tendency to stick to all surfaces, hence become unstable and interrupt with the measurements and accuracy of the mass spectrometer.

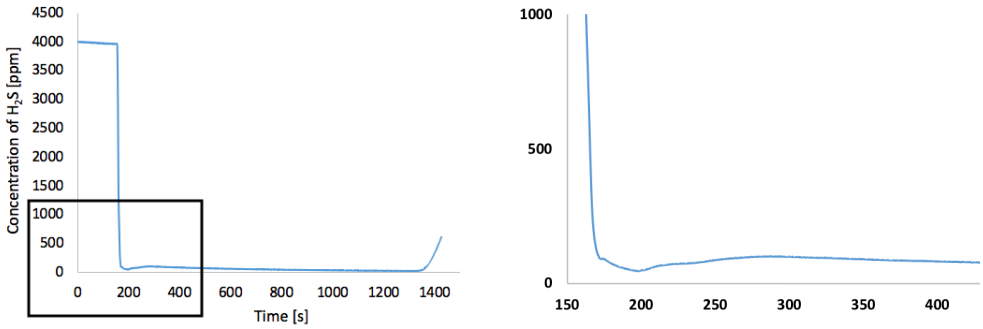

Figure 5.4: Changes in H_2S concentration during sorption. (a): indicate the area of focus; (b): enlarged area to clarify the changes that occur during sorption

5.1.1 Evaluation of Sorbents Prepared by Incipient Wetness Impregnation

Initial Capacity

The initial capacity (cycle 1) for sorbents prepared by incipient wetness impregnation are presented in Figure 5.5. It is observed that the initial capacity is higher for Zr-promoted manganese oxide sorbents supported on alumina (ZrX-Mn15/Al_2O_3) compared to pure manganese on alumina (Mn15/Al_2O_3). Moreover, higher calcination temperature reduces the initial capacity. This can be explained by the sorbents surface area, which will be discussed later.

In general, addition of 5wt% Zr give the highest initial capacity whereas unmodified sorbents (15Mn/Al_2O_3) the lowest. The initial capacity for sorbents containing 1wt% and 10wt% Zr are nearly the same. These observations applies for calcination temperatures at both 500°C and 700 °C. Hence, the initial capacity (cycle 1) decrease in the following order: Zr5-Mn15/Al_2O_3 > Zr10-Mn15/Al_2O_3 ≥ Zr1-Mn15/Al_2O_3 > Mn15/Al_2O_3.

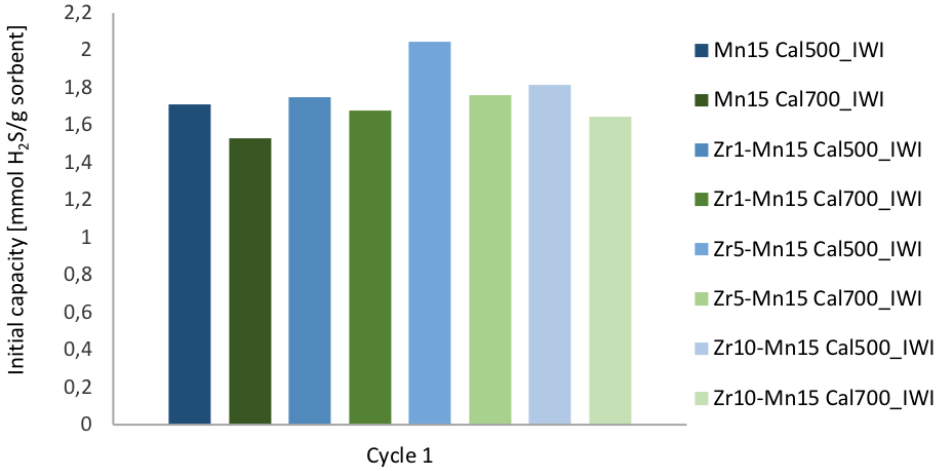

Figure 5.5: Initial capacity for sorbents prepared by incipient wetness impregnation (IWI), calcined at 500°C (blue) and 700°C (green)

Capacity After Multiple Sorption and Regeneration Cycles

The H_2S sorption capacity for the various sorbents calcined at 500°C and 700°C are presented in Figure 5.6 and Figure 5.7, respectively. The sorbent capacity for each sorption cycle (1-10) is included.

For sorbents calcined at 500°C, no significant difference in capacity is observed for $Mn15/Al_2O_3$, $Zr1\text{-}Mn15/Al_2O_3$ and $Zr5\text{-}Mn15/Al_2O_3$, whereas for $Zr10\text{-}Mn15/Al_2O_3$ a more drastic loss in capacity is seen. For the latter, a sudden drop in capacity is observed during cycle 7. The measured capacity for this cycle is expected to be similar as the results obtained for cycle 8-10. It is evident that an error has occurred during the measurements causing the drop in capacity. After 10 cycles the sorption capacity decrease with increasing Zr-loading for sorbents prepared by incipient wetness impregnation and calcined at 500°C: $Mn15/Al_2O_3 > Zr1\text{-}Mn15/Al_2O_3 > Zr5\text{-}Mn15/Al_2O_3 > Zr10\text{-}Mn15/Al_2O_3$.

As for sorbents calcined at 700°C there is not the same noticeable drop in capacity between $Zr10\text{-}Mn15/Al_2O_3$ and the rest of the sorbents. However, after ten cycles the sorption capacities of the sorbents are different from the ones calcined at 500°C. At 700°C the sorption capacity decrease in the following order: $Zr1\text{-}Mn15/Al_2O_3 > Mn15/Al_2O_3 > Zr5\text{-}Mn15/Al_2O_3 > Zr10\text{-}Mn15/Al_2O_3$.

In general, with emphasis on calcination temperature, it is observed that the initial capacity for sorbents calcined at 500°C is higher than at 700°C. However, the overall deactivation is larger after ten cycles of sorption and regeneration at lower temperatures.

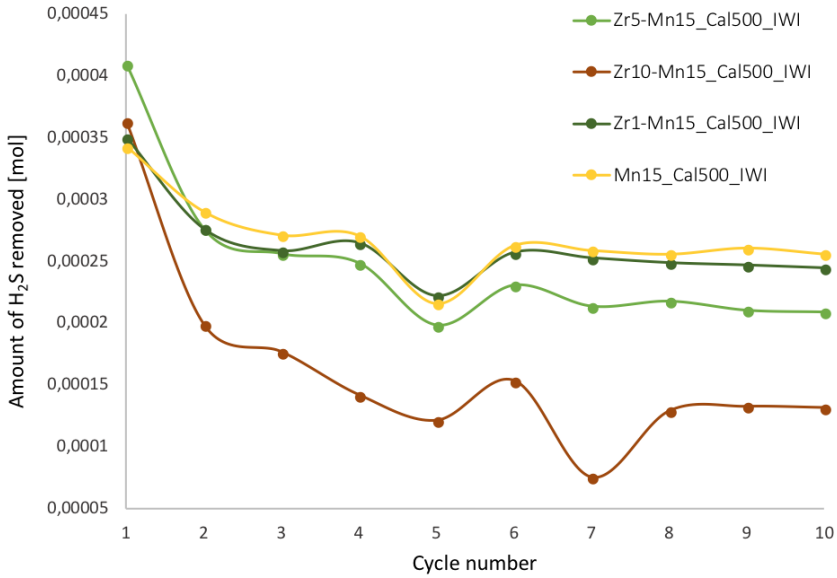

Figure 5.6: H_2S sorption breakthrough capacity for the various sorbents prepared by incipient wetness impregnation (IWI) and calcined at 500°C after ten cycles of sorption and regeneration

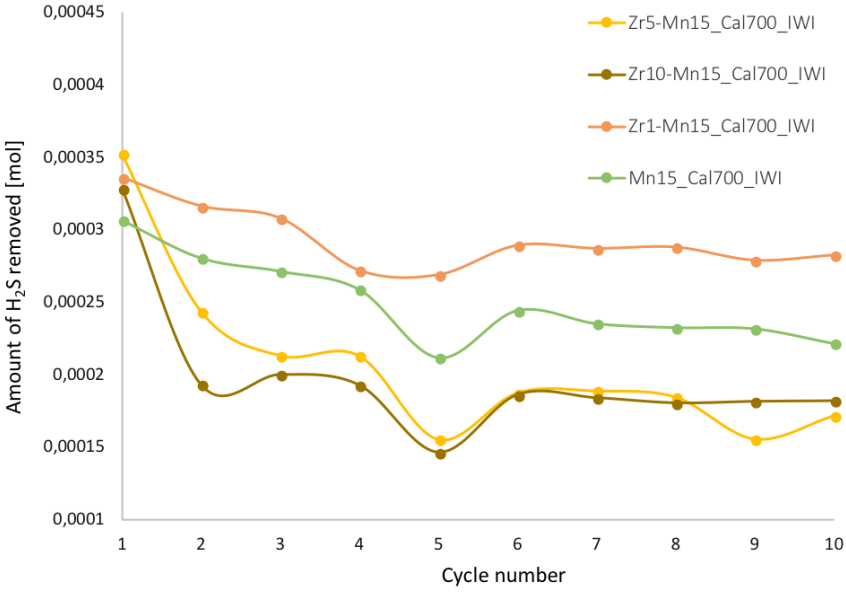

Figure 5.7: H_2S sorption breakthrough capacity for the various sorbents prepared by incipient wetness impregnation (IWI) and calcined at 700°C after ten cycles of sorption and regeneration

Table 5.1 and Table 5.2 show the breakthrough capacity between the first and last sorption for sorbents calcined at 500°C and 700°C, respectively.

After ten sorption and regeneration cycles the most significant drop in capacity for sorbents calcined at 500°C is observed for the Zr10-Mn15/Al_2O_3 sorbent (0.022 g H_2S/g sorbent), whereas the Mn15/Al_2O_3 sorbent show least deactivation (0.043 g H_2S/g sorbent). However, it is observed that the latter has quite similar stability performance as the sorbent promoted with 1wt% Zr (Zr1-Mn15/Al_2O_3, 0.042 g H_2S/g sorbent).

At 700°C the most significant drop in capacity is observed for the Zr5-Mn15/Al_2O_3 sorbent (0.029 g H_2S/g sorbent), whereas Zr1-Mn15/Al_2O_3 (0.048 g H_2S/g sorbent) show least deactivation. The latter also has the best stability performance of all sorbents calcined at both 500°C and 700°C.

With emphasis on Zr-loading, it is observed that sorbents with high Zr-content (Zr5-Mn15/Al_2O_3 and Zr10-Mn15/Al_2O_3) have the most significant drop in capacity after multiple sorption and regeneration cycles, whereas sorbents with 0wt% Zr or 1wt% Zr appears to be more stable with less decrease in capacity. Changes in the surface area of sorbents strongly influence the capacity and will be discussed in more detail later on.

There is a significant deactivation in sorption capacities from the first cycle to the second cycle for all sorbents. This common trend has also been reported by Wakker et al. [49]. Cycle 3-10 are relatively stable, however, a considerable decrease in sorption capacity is also observed at cycle 5, which is the first sorption after the sorbent has been left overnight in a reducing environment (flowing gas mixture of H_2 and N_2). Despite a decrease in capacity at cycle 5, the following cycle (6) demonstrate an improved sorption capacity and keeps stable for the final three (3) cycles.

Table 5.1: Breakthrough capacities of sorbents prepared by incipient wetness impregnation and calcined at 500°C after the first and last sorption (cycle 1 and 10)

Reacted sorbent	Calcination temp.[°C]	Cycle number	capacity [g H_2S/g Sorbent]
Mn15/Al2O3	500	1	0.058
Zr1-Mn15/Al2O3	500	1	0.059
Zr5-Mn15/Al2O3	500	1	0.070
Zr10-Mn15/Al2O3	500	1	0.062
Mn15/Al2O3	500	10	0.043
Zr1-Mn15/Al2O3	500	10	0.042
Zr5-Mn15/Al2O3	500	10	0.035
Zr10-Mn15/Al2O3	500	10	0.022

Table 5.2: Breakthrough capacities of sorbents prepared by incipient wetness impregnation and calcined at 700°C after the first and last sorption (cycle 1 and 10)

Reacted sorbent	Calcination temp. [°C]	Cycle number	capacity [g H_2S/g Sorbent]
Mn15/Al2O3	700	1	0.052
Zr1-Mn15/Al2O3	700	1	0.057
Zr5-Mn15/Al2O3	700	1	0.060
Zr10-Mn15/Al2O3	700	1	0.056
Mn15/Al2O3	700	10	0.038
Zr1-Mn15/Al2O3	700	10	0.048
Zr5-Mn15/Al2O3	700	10	0.029
Zr10-Mn15/Al2O3	700	10	0.031

Table 5.3: Ratio of breakthrough capacity between the first and last sorption (cycle 1 and 10). Sorbents prepared by incipient wetness impregnation and calcined at 500°C and 700°C

Reacted sorbent	Calcination temp. [°C]	Capacity ratio
Mn15/Al2O3	500	0.75
Zr1-Mn15/Al2O3	500	0.70
Zr5-Mn15/Al2O3	500	0.51
Zr10-Mn15/Al2O3	500	0.36
Mn15/Al2O3	700	0.72
Zr1-Mn15/Al2O3	700	0.84
Zr5-Mn15/Al2O3	700	0.49
Zr10-Mn15/Al2O3	700	0.55

Usage efficiency

The usage efficiency is defined in section 4.7, and describes how efficient H_2S is removed by the active part. Usually, the ratio between real amount H_2S removed and theoretical amount H_2S removed is used to describe the efficiency. Table 5.4 presents the usage efficiency after the last sorption (cycle 10) for sorbents calcined at 500° and 700°.

At 500°C the efficiency decrease with increasing Zr-loading, where unmodified sorbent (15Mn/Al_2O_3) show highest efficiency (0.22 g H_2S/g MnO). Addition of 1wt% Zr results in a similar efficiency as unmodified sorbent (0.21 g H_2S/g MnO). However, approximately 50% decrease in efficiency is observed at high Zr-loading (Zr10-Mn15/Al_2O_3, 0.12 g H_2S/g MnO).

At 700°, the efficiency is noticeably higher for 1wt% Zr-promoted sorbent compared to unmodified sorbent; 0.25 g H_2S/g MnO and 0.19 g H_2S/g MnO, respectively. Further, addition of higher Zr-loading (5 and 10wt% Zr) decrease the efficiency (0.15 and 0.16 g H_2S/g MnO).

Overall results indicate that after ten sorption- and regeneration cycles, Zr1-Mn15/Al_2O_3 (calcined 700°C) have the best H_2S removal efficiency (0.25 g H_2S/g MnO), whereas Zr10-Mn15/Al_2O_3 (calcined 500°C) the lowest (0.12 g H_2S/ g MnO). This is also in agreement with the deactivation of capacities.

It is expected that sorbents with a higher surface area (5 and 10wt% Zr) capture greater amounts of H_2S. This is indeed the case for the first sorption (cycle 1). However, after multiple sorption and regeneration cycles these sorbents have the most significant decrease in surface area, hence the larger deactivation and lower efficiency.

Table 5.4: Usage efficiency after the last sorption (cycle 10) for sorbents prepared by incipient wetness impregnation

Reacted sorbent	Calcination temp. [°C]	cycle number	Usage efficiency [$gH_2S/gMnO$]	Usage ratio [real/theoretical]
Mn15/Al2O3	500	10	0.22	0.47
Zr1-Mn15/Al2O3	500	10	0.21	0.45
Zr5-Mn15/Al2O3	500	10	0.18	0.38
Zr10-Mn15/Al2O3	500	10	0.12	0.24
Mn15/Al2O3	700	10	0.19	0.41
Zr1-Mn15/Al2O3	700	10	0.25	0.52
Zr5-Mn15/Al2O3	700	10	0.15	0.31
Zr10-Mn15/Al2O3	700	10	0.16	0.33

Theoretical efficiency = 0.48

Figure 5.8 and Figure 5.9 show the efficiency of all ten sorption and regeneration cycles for sorbents calcined at 500°C and 700°C, respectively. It is observed a similar trend as for sorbent capacities. The efficiency for the first sorption is higher for Zr-promoted sorbents, and the sorbent with high Zr-loading (Zr10-Mn15/Al_2O_3) have the largest deactivation.

At 500° the efficiency decrease in the same order as for capacities: Mn15/Al_2O_3 > Zr1-Mn15/Al_2O_3 > Zr5-Mn15/Al_2O_3 > Zr10-Mn15/Al_2O_3.

The same applies for sorbents calcined at 700°C where the efficiency decrease in the following order: Zr1-Mn15/Al_2O_3 > Mn15/Al_2O_3 > Zr5-Mn15/Al_2O_3 > Zr10-Mn15/Al_2O_3.

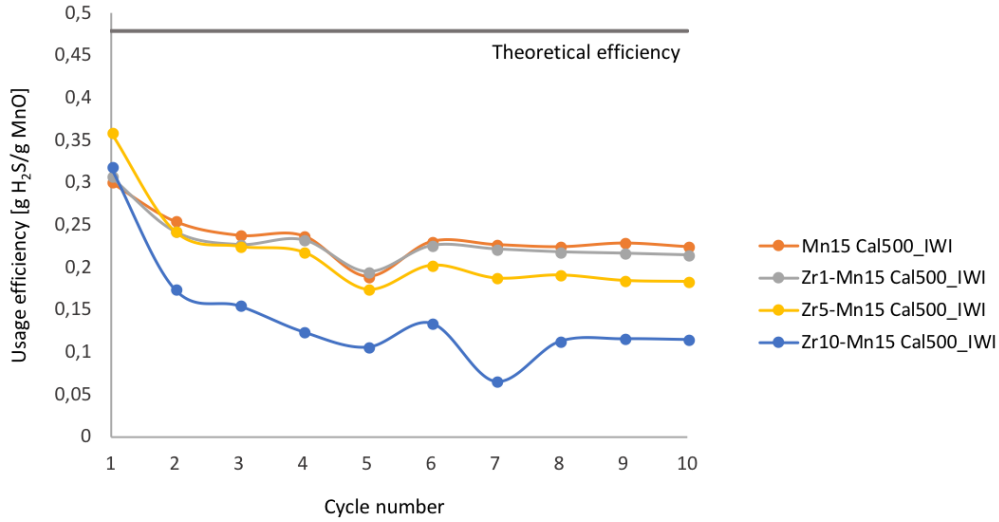

Figure 5.8: Usage efficiency for sorbents calcined at 500°C

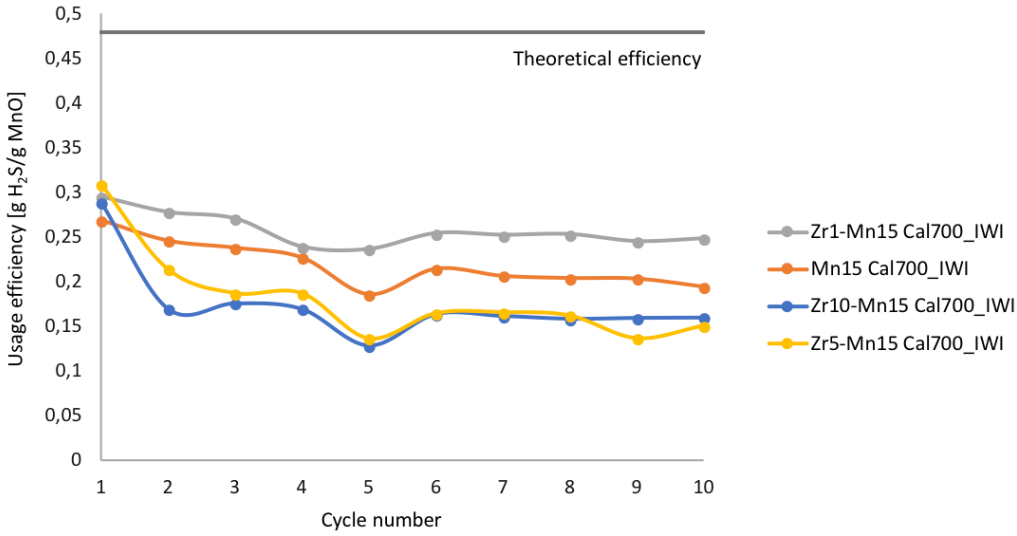

Figure 5.9: Usage efficiency for sorbents calcined at 700°C

5.1.2 Evaluation of Sorbents Prepared by Co-precipitation

Figure 5.10 show the initial capacity for $Mn15/Al_2O_3$ prepared by incipient wetness impregnation and co-precipitation. Higher initial capacity is observed at both 500°C and 700°C for the sorbent prepared by co-precipitation. This is expected as sorbents prepared by co-precipitation have a higher surface area, as discussed in the next section (5.2.1). In general, a decrease in capacity occurs at higher calcination temperature.

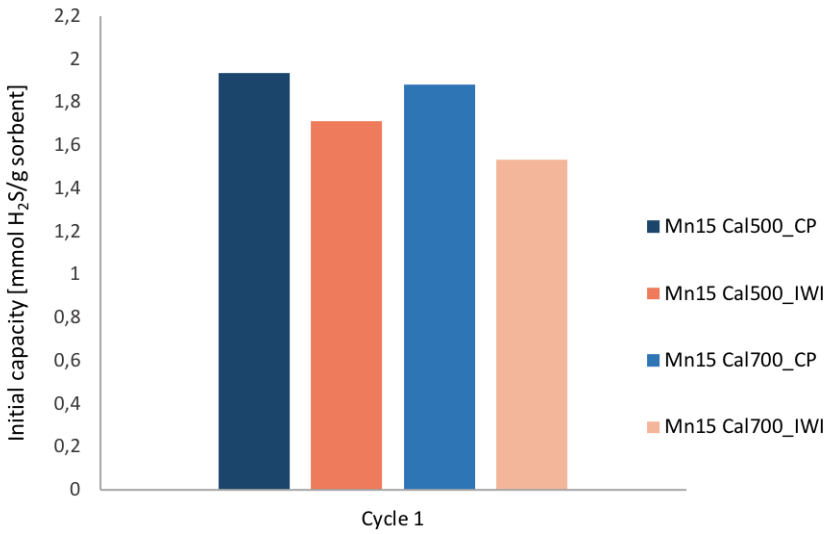

Figure 5.10: Initial capacity for sorbents calcined at 500 °C and 700°C. CP: Co-precipitation (blue), IWI: incipient wetness impregnation (red)

Only one sorbent ($Mn15/Al_2O_3$) prepared by co-precipitation was tested in the sorption-regeneration experiment. The capacity of this sorbent has been compared to the sorbent with the similar composition prepared by incipient wetness impregnation, as illustrated in Figure 5.11.

No significant differences in capacity are observed. However, there is a larger drop in capacity between the two first cycles for sorbents prepared by co-precipitation compared to sorbents prepared by incipient wetness impregnation. Throughout ten sorption and regeneration cycles, the sorbent prepared by incipient wetness impregnation and calcined at 500°C ($Mn15/Al_2O_3$ Cal500 IWI) show best performance. The sorbent with the largest decrease in capacity is observed when prepared using co-precipitation method and calcined at 700°C ($Mn15/Al_2O_3$ Cal700 CP). This is also anticipated from the results after nitrogen adsorption analysis.

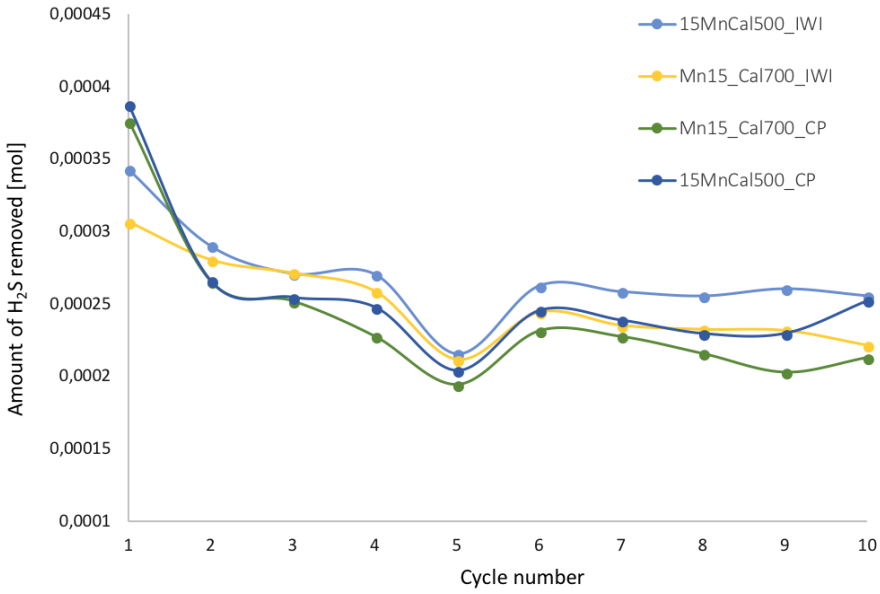

Figure 5.11: H_2S sorption capacity after 10 cycles of sorption and regeneration for reference sorbents ($Mn15/Al_2O_3$) calcined at 500°C and 700°C (CP: Co-precipitation, IWI: incipient wetness impregnation)

5.2 Characterization

5.2.1 Nitrogen Adsorption

BET analysis were performed to characterize the surface area of fresh and reacted sorbents, while pore volume and pore size was determined by BJH analysis. The results for fresh and reacted sorbents are presented in Table 5.5 and Table 5.6, respectively. Summary reports for all sorbents obtained from the analysis software are not included in this report. However one example for the reference sorbent ($Mn15/Al_2O_3$) is given in Appendix E.

In general, at higher calcination temperature the pores expand, hence a reduction in surface area. The textural properties for fresh sorbents indicate that at 500°C the surface area increase with increasing Zr-loading. For sorbents calcined at 700°C, a different trend is observed. The surface area does not increase with Zr-loading. Instead, the surface area increases from 1wt% Zr to 5wt% Zr before it decreases again at 10wt% Zr. This is in agreement with the initial capacity which increases for sorbents containing up to 5wt% Zr. Zr-loading of 10wt% result in a slightly decrease in initial capacity. Further, modified sorbent and 1wt% Zr-promoted sorbent has the same surface area. However, the latter has higher initial capacity. It is observed that after Zr-modification of sorbents with high Zr-loading (5 and 10wt%), both pore diameter and pore volume decreases. Whereas addition of 1wt% Zr causes the pore diameter and pore volume to increase.

Table 5.5: Textural properties of fresh sorbents

Fresh sorbent	Preparation method	BET surface area $[m^2/g]$		Average pore width[a] [nm]		Average pore volume[b] $[cm^3/g]$	
		Cal 500	Cal 700	Cal 500	Cal 700	Cal 500	Cal 700
Al2O3	IWI	169	163	13.4	13.8	0.61	0.60
Mn15/Al2O3	IWI	135	131	12.6	13.0	0.46	0.46
Zr1-Mn15/Al2O3	IWI	134	131	13.1	14.1	0.46	0.48
Zr5-Mn15/Al2O3	IWI	142	140	10.6	11.2	0.40	0.43
Zr10-Mn15/Al2O3	IWI	145	138	9.0	10.1	0.36	0.38
Mn15/Al2O3	CP	273	233	5.2	5.9	0.37	0.36
Zr1-Mn15/Al2O3	CP	169	141	6.3	8.1	0.28	0.29
Zr10-Mn15/Al2O3	CP	289	230	6.6	7.8	0.49	0.46

[a] Based on the Kelvin equation (BJH desorption)
[b] Accumulated
IWI: Incipient wetness impregnation
CP: Co-precipitation

The most distinct changes in textural properties are observed after the sorbents have been tested in multiple sorption-regeneration experiments, which result in a substantial drop in surface area, an enlargement of the pores and loss of pore volume. Commonly, higher calcination temperature leads to loss of surface area. However, a slightly higher surface area is observed at 700°C compared to at 500°C for the sorbent containing 10wt% Zr (Zr10-Mn15/Al_2O_3).

Compared to fresh sorbents, a drop in surface area is observed for all sorbents calcined at both 500°C and 700°C after multiple sorption and regeneration cycles. The surface area decreases with increasing Zr-loading, which is in agreement with the deactivation of capacities. Sorbents containing high Zr-loading (5 and 10wt% Zr) suffered a substantial loss in capacity after ten cycles and had the most significant decrease in surface area. For sorbents calcined at 500° the most significant decrease in surface area after multiple cycles are observed for the Zr10-Mn15/Al_2O_3 sorbent, whereas the lowest decrease is observed for both Mn15/Al_2O_3 and Zr1-Mn15/Al_2O_3. For sorbents calcined at 700°, Zr10-Mn15/Al_2O_3 sorbent show the most substantial decrease in surface area after multiple cycles, whereas Mn15/Al_2O_3 have the lowest reduction. However, Zr1-Mn15/Al_2O_3 have nearly the same surface area as Mn15/Al_2O_3, and these two could be considered to be equal.

Compared to fresh sorbents, the pore volume of all sorbents decreases after ten cycles of sorption and regeneration, and it decrease with increasing Zr-loading, meaning that the Zr10-Mn15/Al_2O_3 sorbent have lowest pore volume. Moreover, this sorbent also have the most significant decrease in surface area, hence show the most substantial loss in capacity. Loss of porosity might indicate sintering, which may explain the deactivation and noticeably loss in capacity.

Compared to fresh sorbents, the pore size is reduced for the Mn15/Al_2O_3 and Zr1-Mn15/Al_2O_3 sorbents after multiple sorption and regeneration cycles, whereas the pore size increases at higher Zr-loading (Zr5-Mn15/Al_2O_3 and Zr10-Mn15/Al_2O_3). Liang et al. [50] reported that larger pores reduce the reaction rate. Moreover, rapid sintering also influences the reaction rate by slowing it down [51]. Hence, it is suggested that sintering can cause the significant deactivation observed for sorbents with high Zr-loading.

Table 5.6: Textural properties of reacted sorbents

Reacted sorbent*	Preparation method	BET surface area [m^2/g]		Average pore width^{a} [nm]		Average pore volume^{b} [cm^3/g]	
		Cal 500	Cal 700	Cal 500	Cal 700	Cal 500	Cal 700
Mn15/Al2O3	IWI	123	118	12.9	12.2	0.42	0.40
Zr1-Mn15/Al2O3	IWI	122	117	13.0	13.6	0.43	0.42
Zr5-Mn15/Al2O3	IWI	104	101	13.2	13.0	0.38	0.37
Zr10-Mn15/Al2O3	IWI	89	90	13.4	13.8	0.34	0.35
Mn15/Al2O3	CP	185.5	186.4	6.89	7.21	0.33	0.35

^{a} Based on the Kelvin equation (BJH desorption)
^{b} Accumulated
IWI: Incipient wetness impregnation
CP: Co-precipitation
* 10 cycles of sorption and regeneration
Sorption temperature: 600°C
Regeneration temperature: 650°C

Sorbents prepared by co-precipitation have significantly higher surface area compared to corresponding sorbents prepared by incipient wetness impregnation. This is also in agreement with the initial capacity, where sorbents prepared by co-precipitation have a noticeably higher initial capacity. Further, the surface area decreases with increasing temperature, which also agrees with the results for initial capacity.

It is observed that co-precipitation provide a larger difference in surface area between unmodified sorbent (273 m^2/g) compared to the 1wt% Zr-promoted sorbent (169 m^2/g). However, the surface area increase substantially at higher Zr-loading (Zr10-$Mn15/Al_2O_3$, 289 m^2/g).

As only one sorbent was tested through multiple sorption and regeneration cycles a sufficient evaluation of the effect of surface area on capacity cannot be made. The initial capacity was higher for sorbent prepared by co-precipitation than incipient wetness impregnation. However, only the unmodified sorbent ($15Mn/Al_2O_3$) was tested. Nor the effect of surface area or Zr-loading on sorbent performance can be evaluated for sorbents prepared by co-precipitation due to lack of experimental data. However, it is expected that Zr optimizes the sorbent stability if a certain amount of Zr is added.

5.2.2 X-Ray Diffraction (XRD)

X-ray diffraction analysis was used for phase identification and the diffractograms of fresh and reacted sorbents prepared by incipient wetness impregnation are presented in Figure 5.12 and Figure 5.13, respectively. After a search and match analysis using Bruker Eva software, the phases identified for the fresh manganese-based sorbents were Mn_2O_3 and MnO_2, whereas Mn_3O_4, $MnAl_2O_4$ and $MnSO_4$ were identified for the reacted sorbents. The reference peaks for the different sorbents after search and match analysis are attached in Appendix F.

The results for fresh sorbents are presented in Figure 5.12. A somewhat broad diffraction pattern is observed for pure γ-Al_2O_3 support, hence indicating low crystallinity. After impregnation with manganese and zirconium new diffraction lines appears, which are sharper and more narrow indicating higher crystallinity. These new diffraction lines represents MnO_2 and Mn_2O_3. The sorbents calcined at 500°C consist of mainly MnO_2(PDF 00-024-0735), in addition to a small peak at 2-theta of 33°, observed for Mn15/Al_2O_3 and Zr1-Mn15/Al_2O_3, indicating Mn_2O_3 (PDF 00-024-0508). Sorbents calcined at 700° consist of only Mn_2O_3.

As it appears from the XRD results a phase change of manganese occur with increasing temperature, which is expected. Nitrate precursor was used in the sorbent preparation and it has been observed that the decomposition of this salt to MnO_2 takes place at very low temperatures (130°C). Further phase transition from MnO_2 to Mn_2O_3 occur when the calcination temperature is increased to 600°C [52, 53, 54].

The peaks at 2-theta of 38° and 2-theta of 39° for sorbents calcined at 500°C and 700°C, respectively, corresponds to different manganese oxide phases depending on calcination temperature, and are overlapped by the diffraction lines for the alumina support.

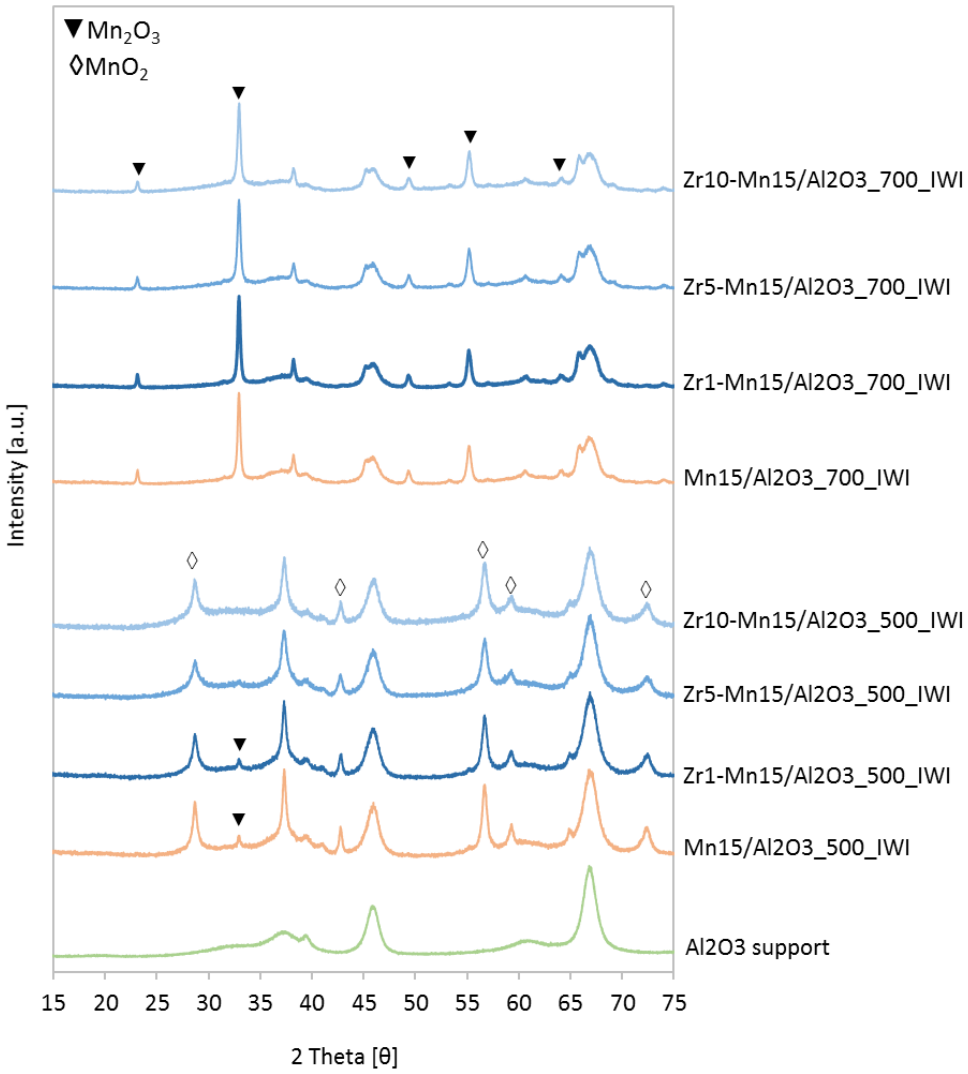

Figure 5.12: XRD patterns for fresh sorbents prepared by incipient wetness impregnation (IWI), and calcined at 500°C and 700°C

The results for reacted sorbents are presented in Figure 5.13. Diffraction patterns for these sorbents are obtained after 10 cycles of sorption and regeneration, and the results indicates new phases, mainly Mn_3O_4 (PDF 00-001-1127) and $MnAl_2O_4$ (PDF 00-029-0880).

The presence of Mn_3O_4 and $MnAl_2O_4$ spinel phase on the reacted sorbents are in agreement with others [21, 55, 56]. Before the first sorption (cycle 1), the sorbent is exposed to a reducing atmosphere during the heating up to sorption temperature (600°C). Since no MnO_2 and Mn_2O_3 phase is observed for the reacted sorbents, and instead Mn_3O_4 become the dominating phase, formation of MnO ($MnO_2 \rightarrow Mn_2O_3 \rightarrow Mn_3O_4 \rightarrow MnO$) during pretreatment of sorbent can be expected at temperatures higher than 250°C . However, reducing environments also emphasize the formation of $MnAl_2O_4$, although at higher temperatures. Hence, it is believed that during sorption MnO reacts with H_2S and forms MnS and water, and subsequently regenerated with O_2 according to the following equations [55]:

$$MnO - Al_2O_3 + H_2S \leftrightarrow MnS - Al_2O_3 + H_2O \tag{5.1}$$

$$MnS - Al_2O_3 + 1.5O_2 \rightarrow MnO - Al_2O_3 + SO_2 \tag{5.2}$$

The presence of $MnAl_2O_4$ spinel phase is common for regenerated sorbents, which implies formation of this phase from MnO and Al_2O_3 formed during regeneration [55].

$$MnO + Al_2O_3 \rightarrow MnAl_2O_4 \tag{5.3}$$

Moreover, the presence of $MnSO_4$(PDF 00-035-0751) phase is also detected on some of the sorbents as shown in Figure 5.13. This indicates that a side reaction (equation 5.4) might have occurred during regeneration, which may cause deactivation and contribute to a loss in capacity.

$$MnS + 3O_2 \leftrightarrow MnSO_4 + SO_2 \tag{5.4}$$

The Zr10-Mn15/Al_2O_3 sorbent has the largest decrease in capacity. However, no $MnSO_4$ was detected for this sorbent, which indicates that $MnSO_4$ may not be responsible for a loss in capacity.

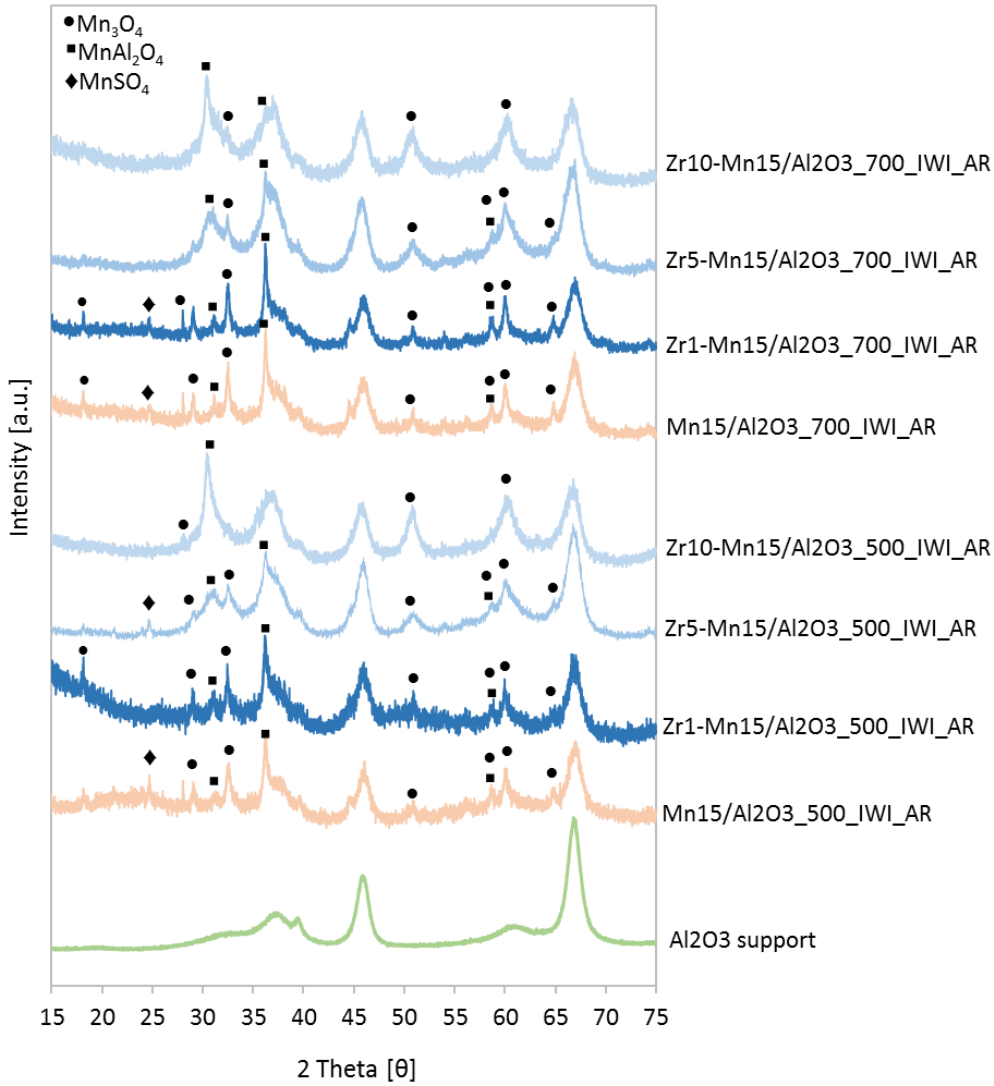

Figure 5.13: XRD patterns for reacted sorbents prepared by incipient wetness impregnation, and calcined at 500°C and 700°C. (AR: after reaction: 10 sorption-regeneration cycles)

Neither the diffraction patterns for fresh or reacted sorbents show the presence of ZrO_2. One limitation of XRD is that it only gives clear and definite information about the structure on particles if they are sufficiently crystalline and large enough [57]. Therefore it is suggested that the ZrO_2 particles are amorphous and that they do not have a sufficient long-range order, hence prevents clear diffraction peaks. Moreover, very small particles (> 5 nm [58]) are not detected by XRD which may indicate that the particles are well dispersed.

The crystallite size of the active phase was estimated from the Scherrer equation (3.4), and the results for the fresh and reacted sorbents are presented in Table 5.7 and Table 5.8, respectively. For the sake of simplicity, crystallite size will be referred to as particle size in the following sections.

For fresh sorbents prepared by incipient wetness impregnation and calcined at 500°C the present manganese oxide phase is MnO_2. The largest particle size is observed for the unmodified sorbent ($Mn15/Al_2O_3$, 18 nm), moreover the particle size decrease with increasing Zr-loading. At 700°C all MnO_2 phase have disappeared and are converted to Mn_2O_3. The largest particle size is observed for the sorbent containing 1wt% Zr (Zr1-$Mn15/Al_2O_3$, 29 nm), while a minor drop in particle size is observed when 5wt% Zr (Zr5-$Mn15/Al_2O_3$, 24 nm) is added. However, a slight increase in particle size is observed at higher Zr-content (Zr10-$Mn15/Al_2O_3$, 25 nm). The particle size of unmodified sorbent ($Mn15/Al_2O_3$, 28 nm) does not differ much from the 1wt% Zr-promoted sorbent.

In general, the particle size for fresh sorbents increase with increasing calcination temperature, and sorbents calcined at 700°C have a significantly higher particle size than the corresponding sorbents calcined at 500°C. N_2-adsorption measurements indicated that higher calcination temperature results in a reduction of surface area, hence larger pores. This is in agreement with the particle size estimation where higher calcination temperature results in larger Mn-oxide particles. It should be pointed out that when comparing particle size for different manganese oxide phases, one must consider the densities of the MnO_x-phases. The density of MnO_2 and Mn_3O_4 is 5.026 g/cm^3 and 4.5 g/cm^3, respectively. A rather small difference, which will have a minor impact on the particle size. The result is only a few nanometer decrease in the particle size of Mn_3O_4.

Table 5.7: Crystallite size of active phase for fresh sorbents

Fresh sorbents	Calcination temperature [°C]	Preparation method	Crystallite size, L [nm]*		
			Mn_2O_3 θ=33	MnO_2 θ=56	Mn_3O_4 θ=34
$Mn15/Al_2O_3$	500	IWI	-	18	-
$Zr1\text{-}Mn15/Al_2O_3$			-	16	-
$Zr5\text{-}Mn15/Al_2O_3$			-	15	-
$Zr10\text{-}Mn15/Al_2O_3$			-	14	-
$Mn15/Al_2O_3$	700	IWI	28	-	-
$Zr1\text{-}Mn15/Al_2O_3$			29	-	-
$Zr5\text{-}Mn15/Al_2O_3$			24	-	-
$Zr10\text{-}Mn15/Al_2O_3$			25	-	-
$Mn15/Al_2O_3$	500	CP	24	-	-
$Zr1\text{-}Mn15/Al_2O_3$			-	-	-
$Zr10\text{-}Mn15/Al_2O_3$			24	-	-
$Mn15/Al_2O_3$	700	CP	27	-	-
$Zr1\text{-}Mn15/Al_2O_3$			-	-	29
$Zr10\text{-}Mn15/Al_2O_3$			32	-	-

* Calculated from the Scherrer equation using EVA software. The crystallite size is calculated as full width at half maximum (FWHM).
IWI: Incipient wetness impregnation
CP: Co-precipitation

With regards to reacted sorbents, the particle size decrease with increasing Zr-loading and increasing temperature, meaning that the particle size for sorbents calcined at 500°C is larger than the corresponding sorbents calcined at 700°C.

At 500°C, when compared to fresh sorbents, larger particle size is obtained for sorbents with low Zr-loading (0 and 1wt% Zr), whereas sorbents with high Zr-loading (5 and 10wt%Zr) have smaller particle size after ten sorption and regeneration cycles. However, at 700°C, smaller particle size is observed for all sorbents. Decrease in particle size might be due to formation of more stable phases, such as $MnAl_2O_4$, which was identified by XRD analysis. Hence, it would become more challenging to adsorb sulfur.

As earlier discussed, sorbents with high Zr-loading (5wt% Zr an 10wt% Zr) show a larger deactivation. Further, these sorbents are estimated to have smaller particle size after multiple sorption and regeneration cycles, most probably due to sintering. It has been reported that in a reducing environment at higher temperatures, smaller particles are more susceptible to sintering [59].

Table 5.8: Crystallite size of active phase for reacted sorbents

Reacted sorbents	Calcination temperature [°C]	Preparation method	Crystallite size, L [nm]* Mn_3O_4 θ=60
$Mn15/Al_2O_3$			25
$Zr1\text{-}Mn15/Al_2O_3$	500	IWI	31
$Zr5\text{-}Mn15/Al_2O_3$			12
$Zr10\text{-}Mn15/Al_2O_3$			9
$Mn15/Al_2O_3$			23
$Zr1\text{-}Mn15/Al_2O_3$	700	IWI	21
$Zr5\text{-}Mn15/Al_2O_3$			10
$Zr10\text{-}Mn15/Al_2O_3$			9
$Mn15/Al_2O_3$	500	CP	24
$Mn15/Al_2O_3$	700	CP	21

* Calculated from the Scherrer equation using EVA software. The crystallite size is calculated as full width at half maximum (FWHM).
IWI: Incipient wetness impregnation
CP: Co-precipitation

For fresh sorbents prepared by co-precipitation and calcined at 500°C, no MnO_2 phase is present, only Mn_2O_3. This is in agreement with XRD results presented in the next section. No change in particle size is observed between unmodified sorbent and promoted sorbent containing 10wt% Zr. For fresh sorbents calcined at 700°C, both Mn_2O_3 and Mn_3O_4 phases are present, which is in agreement with XRD results. It is observed that the particle size increase with increasing Zr-loading. An overall observation is an increase in particle size with increasing temperature.

After ten sorption and regeneration cycles, the particle size for unmodified sorbent (Mn/Al_2O_3) maintains the same at 500°C, whereas the particle size decrease at 700°C.

Due to difficulties related to noise during analysis, the particle size for $Zr1\text{-}Mn15/Al_2O_3$ calcined at both 500°C and 700°C was not estimated. It should be pointed out that estimation of particle size from the broadening of the peak, is not that accurate. However, it can give an indication and a trend of the changes in particle size. XRD analysis only measures the size on crystalline phases. Hence, there is no guarantee that other phases are not present, in addition to those already identified.

Diffractograms of fresh and reacted sorbents prepared by co-precipitation are presented in Figure 5.14 and Figure 5.15, respectively.

After a search and match analysis using Bruker Eva software, Mn_2O_3 was identified as the dominating manganese oxide phase for fresh sorbents calcined at both 500°C and 700°C. However, Mn_3O_4 was also identified for one of the sorbents calcined at 700°C, namely Zr1-Mn15/Al_2O_3. The precence of this manganese oxide phase was also reported by Bulavchenko et.al. [60]. A previous study of manganese-based sorbents prepared by co-precipitation [61] observed that Mn_2O_3 was present at higher manganese content (> 13.7%), while Mn_3O_4 is present at lower Mn-content. In the present study a constant Mn-loading of 15wt% was used, and the one peak identified as Mn_3O_4 might be related to the preparation method. Co-precipitation can provide a better dispersion. Hence, it might be easier to form Mn_3O_4 than Mn_2O_3 at a higher temperature.

Only one sorbent, Mn15/Al_2O_3 calcined at 500°C and 700°C, was tested in a sorption-regeneration experiment. Figure 5.15 presents the XRD results for the reacted reference sorbent prepared by co-precipitation. As for incipient wetness impregnation, the same phases (Mn_3O_4, $MnAl_2O_4$ and $MnSO_4$) were identified, and the same finding was also reported by Wang et al. [61].

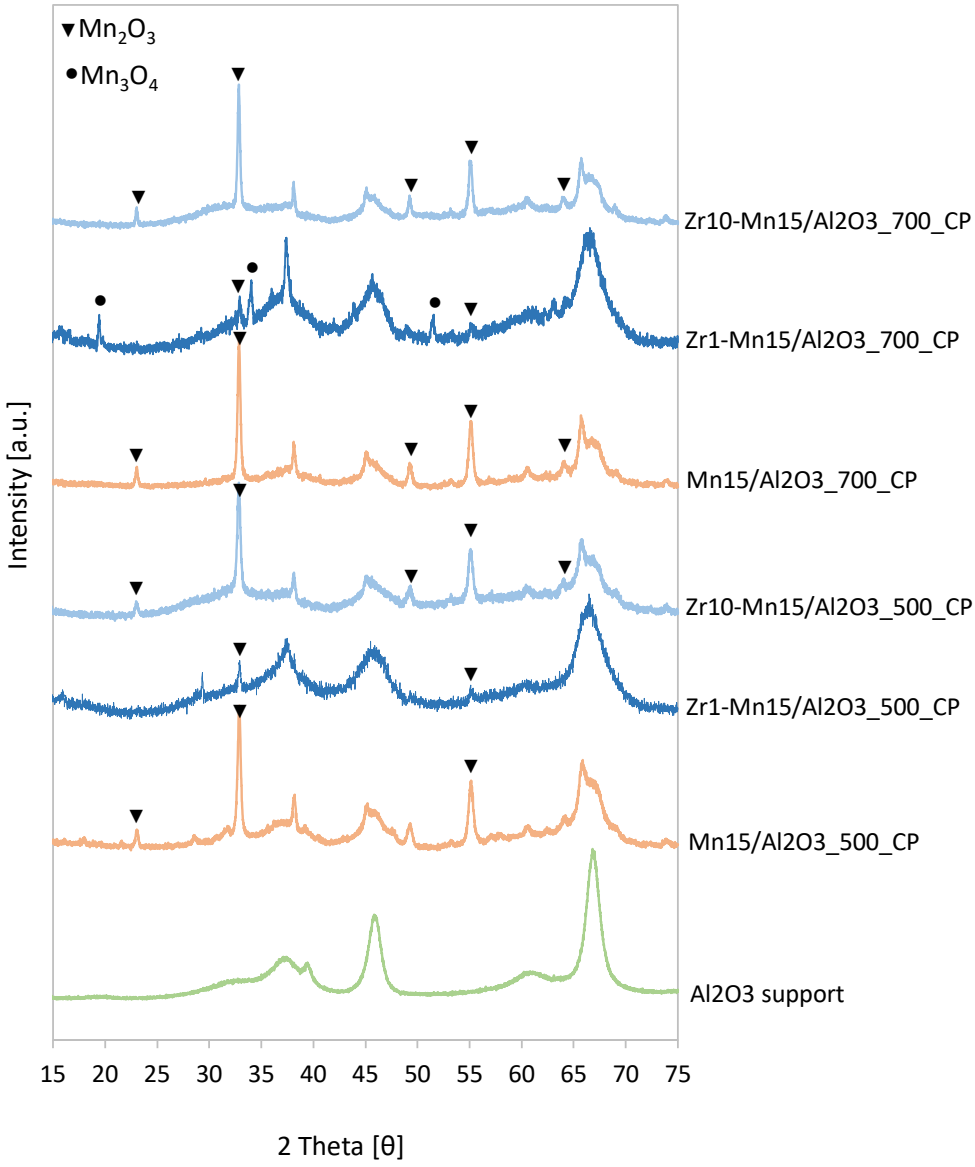

Figure 5.14: XRD patterns for fresh sorbents prepared by co-precipitation (CP), and calcined at 500°C and 700°C

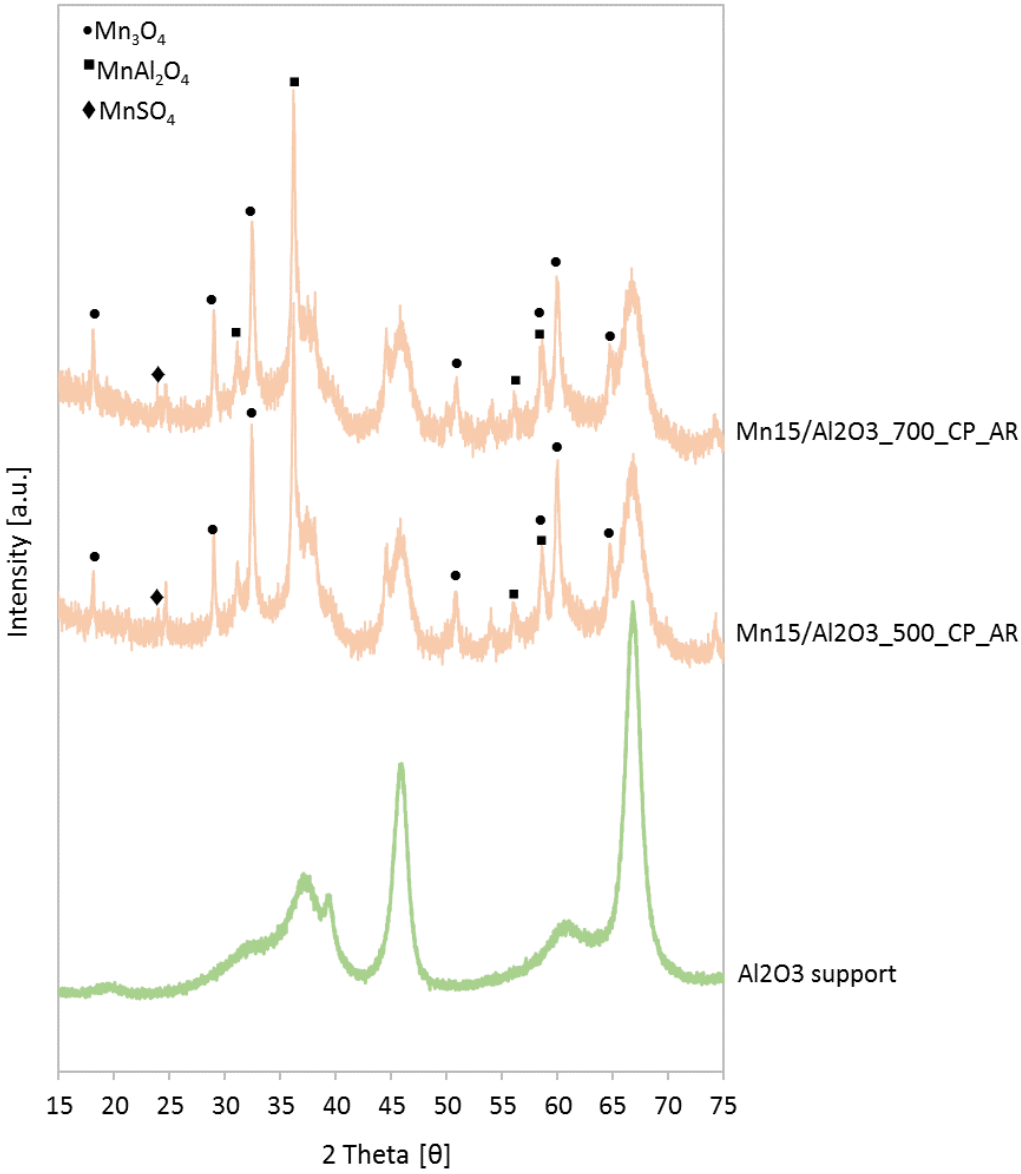

Figure 5.15: XRD patterns for reacted sorbents prepared by co-precipitation (CP), and calcined at 500°C and 700°C. (AR: after reaction; 10 sorption and regeneration cycles)

5.2.3 Temperature Programmed Reduction (TPR)

Temperature programmed reduction was performed to study the reduction properties of the prepared sorbents (fresh) in the temperature range 50-800°C. Due to the reductive character of biomass gasification gas it is desirable to study the reduction behavior of the manganese-based sorbents.

Figure 5.16 show reduction profiles for sorbents prepared by incipient wetness impregnation, calcined at 500°C and 700°C. The reduction profiles include manganese-based sorbents that are both Zr-modified and unmodified (reference). However, XRD did not reveal ZrO_2. Thus, the reduction peaks presented here are attributed to Mn_xO_y reduction.

As it appears from Figure 5.16, there are two main reduction peaks. For sorbents calcined at 500°C the reduction peaks look the same with a distinct first peak and a broad second peak, observed at temperatures from 335° to 430°. At 700°C, a peak shift to higher temperature is observed. For Mn15/Al_2O_3 and Zr1-Mn15/Al_2O_3 a broad first peak is observed at approx. 370°C, while a distinct second peak is observed at approx. 460°C. The two remaining sorbents calcined at 700°C (Zr5-Mn15/Al_2O_3 and Zr10-Mn15/Al_2O_3) have two broad and overlapping peaks at approx. 380°C and 440°C, indicating strong interaction between the metal oxide and the support.

Typically, a change in sorbent color from black to green was observed after H_2-TPR analysis, as it can be seen from Figure 5.17, which indicates formation of MnO [52]. According to literature, alumina-supported manganese oxides follow a three-step reduction process for the reduction of MnO_2 to MnO with Mn_2O_3 and Mn_3O_4 as intermediates [52, 53, 54]. The reduction process proceeds as follows:

$$2MnO_2 + H_2 \rightarrow Mn_2O_3 + H_2O \tag{5.5}$$

$$3Mn_2O_3 + H_2 \rightarrow 2Mn_3O_4 + H_2O \tag{5.6}$$

$$Mn_3O_4 + H_2 \rightarrow 3MnO + H_2O \tag{5.7}$$

In accordance to XRD results, which identified MnO_2 and Mn_2O_3 as the present manganese oxide phases, the two main peaks can be attributed to the reduction of MnO_2 → Mn_2O_3 and → Mn_2O_3 → Mn_3O_4, respectively.

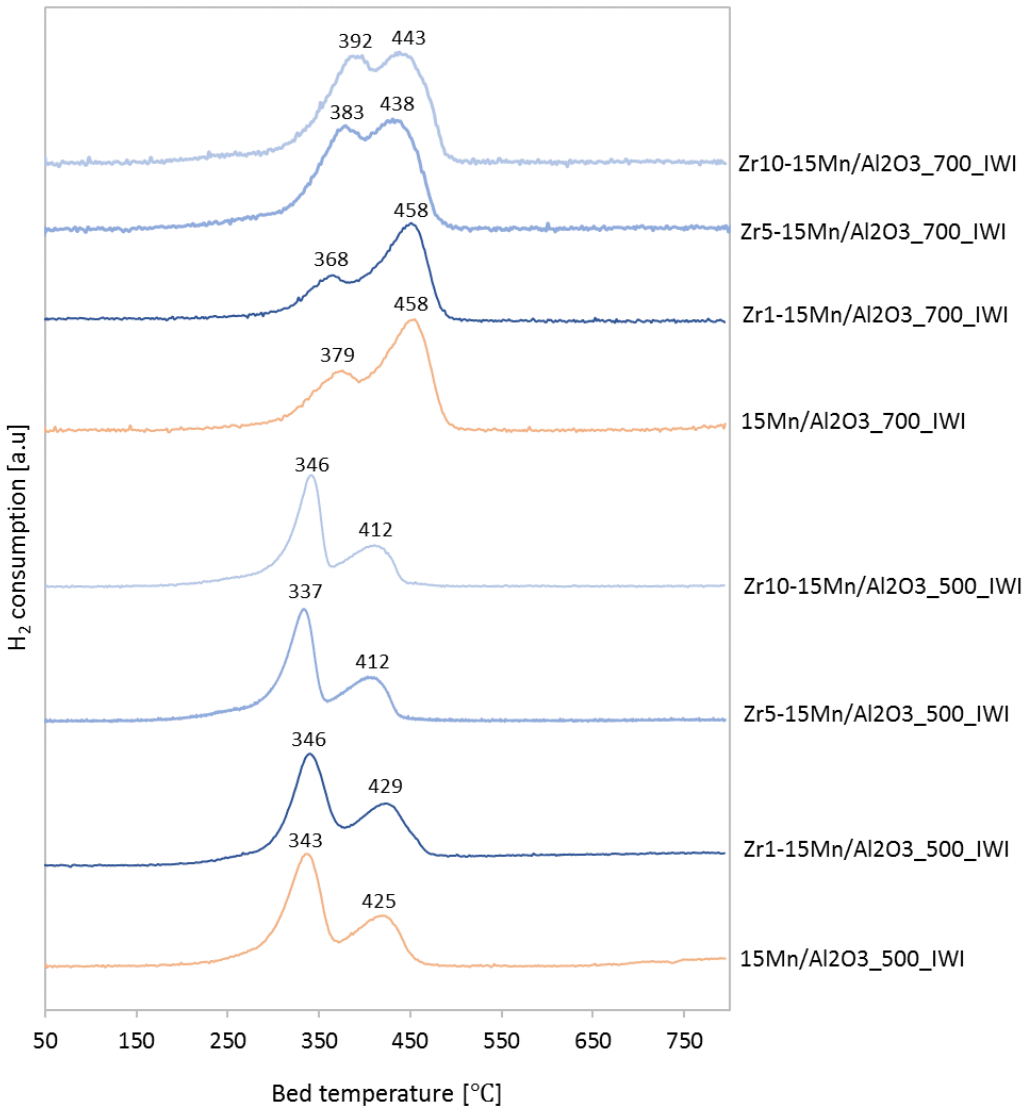

Figure 5.16: TPR profiles for fresh sorbents prepared by incipient wetness impregnation (IWI) and calcined at 500°C and 700°C

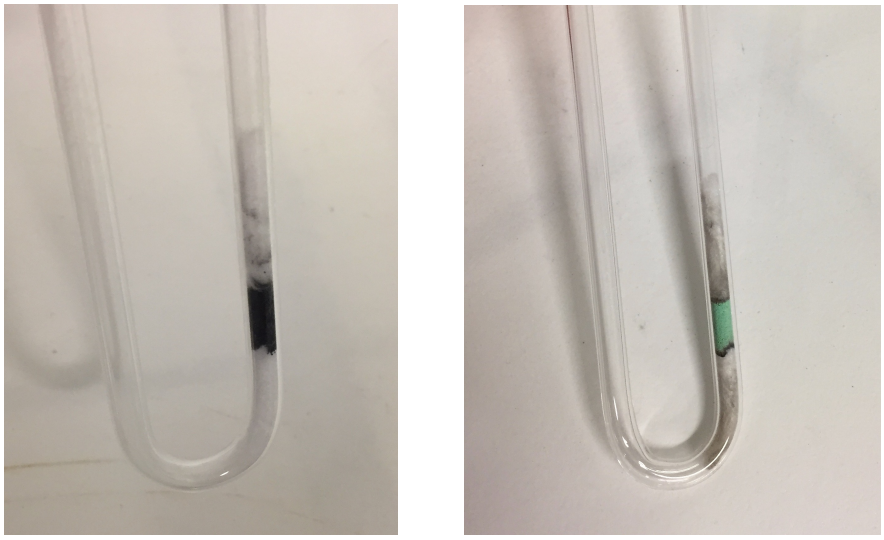

(a) **(b)**

Figure 5.17: Prepared sorbent (Zr1-Mn15/Al_2O_3) before (a) and after (b) H_2-TPR analysis

Figure 5.18 show reduction profiles for sorbents prepared by co-precipitation. The reference sorbent (15Mn/Al_2O_3) calcined at 500°C has two reduction peaks similar to that prepared by incipient wetness impregnation, with a distinct first peak at 295°C and a somewhat broad second peak at 406°C. The same could also be said for the reference sorbent calcined at 700°C, where the reduction peak shift to higher temperature. However, the first reduction peak at 341°C is more distinct and narrow compared to the same sorbent prepared by incipient wetness impregnation. At higher Zr-loading (10wt% Zr) and temperature (700°C), two broad and overlapping reduction peaks was observed for sorbents prepared by incipient wetness impregnation. However, when prepared by co-precipitation these peaks become more distinct and narrow. It is assumed that the two main peaks are attributed to the reduction of $MnO_2 \rightarrow Mn_2O_3$ and $Mn_2O_3 \rightarrow Mn_3O_4$, respectively.

All sorbents, except for the Zr-promoted sorbents containing 1wt% Zr, prepared by co-precipitation is assumed to follow the same reduction process as for sorbents prepared by incipient wetness impregnation:

$$2MnO_2 + H_2 \rightarrow Mn_2O_3 + H_2O \tag{5.8}$$

$$3Mn_2O_3 + H_2 \rightarrow 2Mn_3O_4 + H_2O \tag{5.9}$$

Low loading sorbents (1wt% Zr) prepared by co-precipitation show different reduction behavior than the corresponding sorbents prepared by incipient wetness impregnation. For the first mentioned the reduction peaks appears to be overlapping. This might indicate a strong interaction to the support. Hence it seems that higher Zr-loading reduces the interaction between metal and support due to more narrow and clear peaks.

The sorbent containing 1wt% Zr calcined at 500° have a distinct reduction peak observed at 362°C, with a shoulder at 420°C and 467°C. XRD results identified Mn_2O_3 as the present manganese phase. Hence, the first reduction peak might be attributed to the reduction of MnO_2 to Mn_2O_3. The two broad shoulders may indicate reduction of small crystallites and presence of other manganese oxides and aluminate species.

At 700°C, no distinct peak is observed on the sorbent containing 1wt% Zr. However a broadening of the peaks occur with three overlapping peaks at 351°C, 442°C and 495°C. This might indicate high dispersion of metal oxide on support. The reduction peaks shift to a higher temperature which may indicate the presence of smaller particles. The two first peak might be attributed to the reduction of $MnO_2 \rightarrow Mn_2O_3$ and $Mn_2O_3 \rightarrow Mn_3O_4$. Additionally, XRD detected Mn_3O_4 phase for this sorbent. Hence it is assumed that the third peak is attributed to the reduction of Mn_3O_4 MnO. Bulavchenko et al. [60] reported that the reduction peak attributed to the reduction of Mn_3O_4 to MnO occur at temperatures between 350-500°C, which is in agreement with the results presented here. The reduction process proceeds as follows:

$$2MnO_2 + H_2 \rightarrow Mn_2O_3 + H_2O \tag{5.10}$$

$$3Mn_2O_3 + H_2 \rightarrow 2Mn_3O_4 + H_2O \tag{5.11}$$

$$Mn_3O_4 + H_2 \rightarrow 3MnO + H_2O \tag{5.12}$$

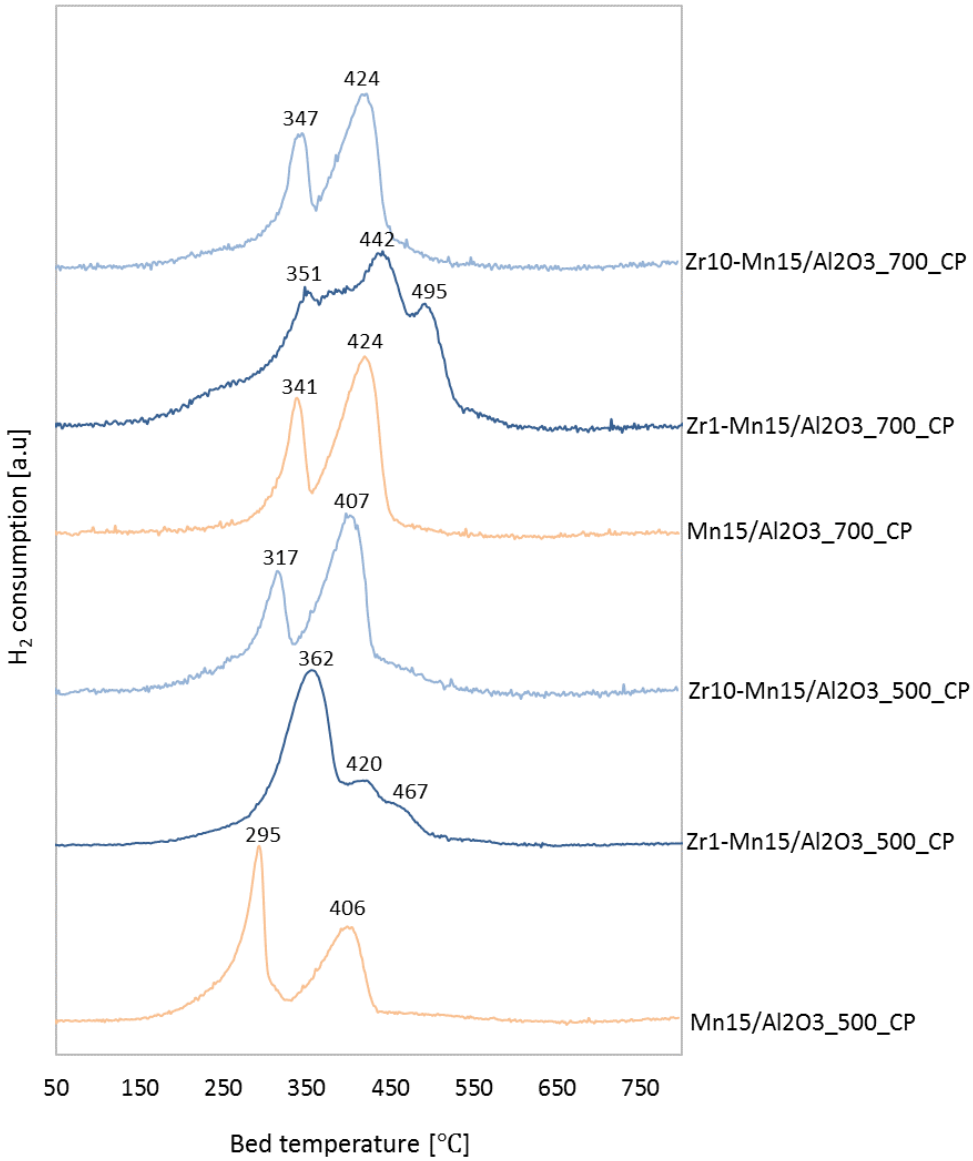

Figure 5.18: TPR profiles for fresh sorbents prepared by co-precipitation (CP) and calcined at 500°C and 700°C

5.2.4 X-Ray Fluorescence (XRF)

XRF was used to study elemental composition of all fresh sorbents. Preparation of pellets were repeated three (3) times for all batches to ensure reproducibility of the measurements performed on the pellet. Raw data from the analysis are given in Appendix G.

The Mn- and Zr-content are calculated from the detected manganese oxide (MnO) and zirconium dioxide (ZrO_2) content, and the results are presented in Table 5.9. XRF data confirm incorporation of Zr in all the promoted sorbents, as expected. However, for sorbents prepared by incipient wetness impregnation the quantitative analysis of the sorbents are not in agreement with the the theoretical composition as it shows lower Zr content. Moreover, the analysis indicates a minor loss of Mn, however it is observed that the Mn-content increase with increasing Zr-loading.

Table 5.9: Calculated manganese and zirconium content for fresh sorbents, based on results from XRF analysis

Sorbent	Preparation method	MnO content[a] [wt%]		Mn content[a] [wt%]		ZrO_2 content[a] [wt%]		Zr content[a] [wt%]	
		Cal 500	Cal 700	Cal 500	Cal 700	Cal 500	Cal 700	Cal 500	Cal 700
Mn15/Al2O3	IWI	15.1	14.2	11.8	11.1	-	-	-	-
Zr1-Mn15/Al2O3	IWI	13.3	14.4	10.3	11.2	0.6	0.6	0.4	0.5
Zr5-Mn15/Al2O3	IWI	17.4	16.4	13.5	12.8	4.0	3.4	3.0	2.5
Zr10-Mn15/Al2O3	IWI	18.3	19.1	14.2	14.8	8.9	8.7	6.6	6.4
Mn15/Al2O3	CP	17.1	17.2	13.3	13.4	-	-	-	-
Zr1-Mn15/Al2O3	CP	22.5	22.7	17.5	17.6	1.2	1.2	0.9	0.9
Zr10-Mn15/Al2O3	CP	21.5	22.2	16.7	17.3	15.1	15.1	11.2	11.2

[a] average value
IWI: Incipient wetness impregnation
CP: Co-precipitation

Zr-promoted sorbents should have theoretical values of 1wt%, 5wt% and 10wt% Zr and a constant Mn-loading of 15wt%. However, the analysis data indicates a significant lower Zr-content that is approximately half the wt% from what is expected for sorbents prepared by incipient wetness impregnation. These results might be attributed to a loss of materials during sorbent preparation. However, a critical step in XRF analysis is the preparation of pellet and achieving a homogeneous mixture. As it can be seen from Figure 5.19 there are some darker spots on the surface of the pellets, which may indicate that the samples are not sufficiently homogeneous.

Figure 5.19: Prepared pellets prior to XRF analysis

X-ray fluorescence data for sorbents prepared by co-precipitation have a composition that is closer to theoretical values, however the Zr-content is higher than expected for the sorbent containing 10wt% Zr. XRF indicates that this sorbent consist of approximately 11wt% Zr. The same trend is also observed for the manganese content as it is slightly higher than expected. Sorbent preparation using co-precipitation provide optimal mixing of the different species. Hence, good homogeneity. Moreover, the filtration cake is thoroughly washed before drying and high purity can be achieved.

XRF also reveals that sorbents prepared by both incipient wetness impregnation and co-precipitation contain other components such as iron oxide (Fe_2O_3), potassium oxide (K_2O), silicon dioxide (SiO_2) and sulfur trioxide (SO_3). However, these components are present in very small amounts and there is an uncertainty whether these elements are actually present or if it is fluorescence effects. Minor amounts of Hafnium dioxide (HfO_2) was also detected for sorbents containing 10wt% Zr, and according to Nielsen and Wilfing [62] hafnium is present in all known zirconium minerals. Additionally, the presence of sodium oxide (Na_2O) is observed for one of the sorbents (Zr1-Mn15/Al_2O_3) prepared by co-precipitation. It is suggested that the latter case is due to the use of Na_2CO_3 and NaOH during preparation. Residuals of these components might not have been completely removed during the washing step.

Interpretation of results from XRF analysis must be done with caution, and the analysis give only a indication of the sample composition. The purpose of XRF analysis in this study was to get qualitative information, not quantitative.

5.2.5 Scanning Electron Microscope (SEM)

Figure 5.20 show SEM images of fresh (a) and sulfided-regenerated (b) reference sorbent ($15Mn/Al_2O_3$) prepared by incipient wetness impregnation and calcined at 700°C. SEM images of sorbent with similar composition prepared by co-precipitation are presented in the same figure, where (c) and (d) indicates fresh and reacted sorbent, respectively. For all SEM imgaes presented in this section, a scalebar of 5μm and a magnification of 10 000x is used.

The surface of fresh sorbent (a) prepared by incipient wetness impregnation appears to be more rough compared to the sorbent prepared by co-precipitation (c), which seems smoother. Thus, it might indicate that incipient wetness impregnation cause more aggregated particles, while co-precipitation give homogeneous distribution of the active metal.

After multiple sorption and regeneration cycles the surface of the sorbent prepared by incipient wetness impregnation changes, and it can appear that the fresh $Mn15/Al_2O_3$ sorbent consist of smaller particles (a) that become larger after reaction (b). This might be an indication of sintering. For sorbent prepared by co-precipitation no evident change in microstructure is observed after multiple sorption and regeneration cycles.

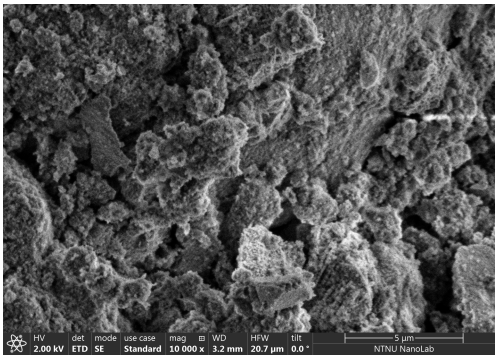

(a) 15MnCal700 Fresh (IWI)

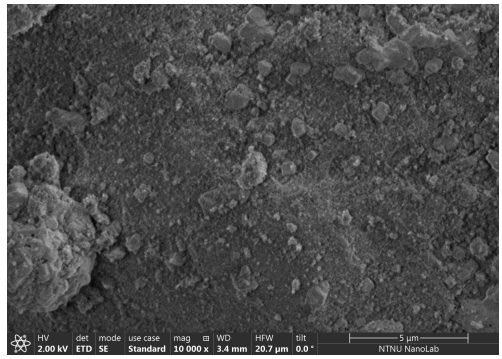

(b) 15MnCal700 AR (IWI)

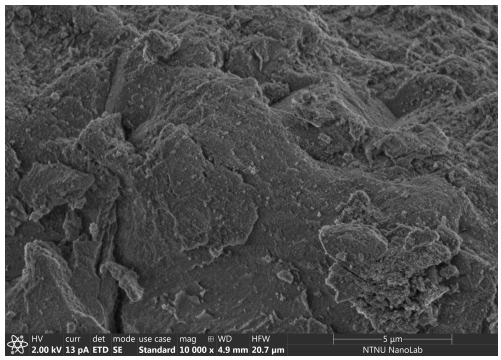

(c) 15MnCal700 Fresh (CP)

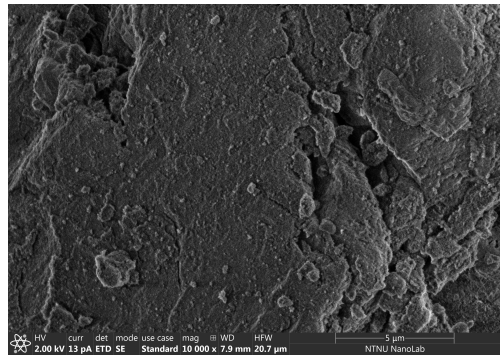

(d) 15MnCal700 AR (CP)

Figure 5.20: SEM images of fresh and reacted (AR) reference sorbents ($15Mn/Al_2O_3$) prepared by incipient wetness impregnation (IWI) and co-precipitation (CP), with a magnification of 10 000x. Scale: 5 μm

Figure 5.21 show SEM images for fresh (a) and reacted (b) Zr-promoted sorbent (1wt% Zr). Same scale and magnification (5μm and 10 000x) is used.

An evident change in microstructure is observed after multiple sorption and regeneration experiments for Zr-promoted sorbent (1wt% Zr). On the reacted sorbent primary particles can be clearly seen, while these particles are absent on the fresh sorbent. This might be an indication that sintering occurs.

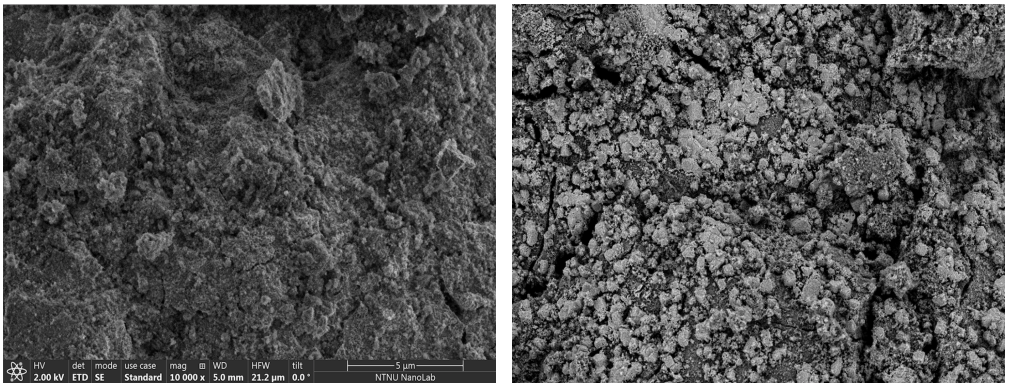

(a) Zr1-15MnCal700 Fresh (IWI) **(b)** Zr1-15MnCal700 AR (IWI)

Figure 5.21: SEM images of fresh (a) and reacted (AR) (b) sorbent promoted with 1wt%Zr (Zr1-Mn15/Al_2O_3), prepared by incipient wetness impregnation (IWI). Magnification:10 000x; Scale: 5 μm

It should be pointed out that SEM images were only performed on one single spot on the sorbent surface. For more reliable results, several random spots should be picked for SEM imaging, and documented with numerous pictures!

Chapter 6

Conclusion

Sorption capacity and stability of Zr-promoted Mn/Al_2O_3 sorbents, including the effect of Zr-loading, calcination temperature and preparation method, was investigated in this paper.

Incipient wetness impregnation and co-precipitation synthesized sorbents with different Zr-loading (0, 1, 5 and 10wt%), calcined at 500°C and 700°C, where characterized by N2-adsorption, XRD, TPR, XRF and SEM. H_2S sorption capacities of prepared sorbents were tested in a quartz fixed bed reactor over ten (10) sorption and regeneration cycles.

Influence of Zr-loading
Addition of small amounts of Zr to Mn/Al_2O_3 sorbents improved the H_2S sorbent performance, whereas higher Zr-content results in worse stability. Hence, the Zr1-Mn/Al_2O_3 sorbent show best desulfurization performance, while Zr10-Mn/Al_2O_3 the lowest.

Influence of calcination temperature
Sorbents calcined at 500°C have better initial capacity than the corresponding sorbents calcined at 700°C. However, the deactivation after ten sorption and regeneration cycles is slightly higher for sorbents calcined at 500°C.

Influence of preparation method
Sorbents prepared by co-precipitation have higher initial capacity compared to incipient wetness impregnation. However, the deactivation after ten sorption- and regeneration cycles is larger. These findings are in agreement with data obtained from BET-analysis, where the sorbent prepared by co-precipitation have the most substantial drop in surface area after ten cycles.

Chapter 7

Future Work

Further investigation of the effect of preparation method should be continued. Hence, all sorbents prepared by co-precipitation must be tested in multiple sorption-regeneration experiments under same conditions. Besides, synthesis of sorbent containing 5wt% Zr by co-precipitation should be conducted to get a sufficient evaluation between co-precipitation method and incipient wetness impregnation. Moreover, characterization of sorbents using Raman spectroscopy and chemisorption is recommended for further investigation of Mn- and Zr-oxide phases present, as well as information about dispersion and particle size of the sorbents.

Long-term sorption and regeneration experiment, preferably 50 cycles, on the sorbent showing best desulfurization performance (Zr1-Mn15/Al_2O_3 calcined at 700°C) is essential and highly recommended to see if the stability is maintained.

During sorption and regeneration experiments, a substantial decrease in capacity is always observed for the 5th cycle. However, the capacity increases again for the following cycle (6) and then keeps relatively stable from cycle 6 to 10. Cycle five is the first cycle after the sorbent has been left overnight in a gas flow of N_2 and H_2. Hence, this typical trend should be investigated closer to understand the influence of a reducing environment on the sorbent.

Steam is a key constituent of the produced syngas from biomass gasification. Hence, it is necessary to investigate the effect of steam for modeling the raw biomass. Introducing steam in the sorption and regeneration experiments is highly desirable to be able to study the effect on sorbent performance.

Study on regeneration conditions by comparing different factors, such as temperature, pressure and gas composition, is recommended for optimization of stability, hence acquire better kinetics.

Formation of manganese sulfide (MnS) was observed on the reactor wall after sorption- and regeneration experiments. Limitations related to the mass spectrometer for quantitative analysis might influence the accuracy of the measurements. Thus, it is suggested that new detection instruments are introduced to acquire more accurate sorption capacity data. .

Bibliography

[1] S. Cheah, D. L. Carpenter, and K. A. Magrini-Bair, ''Review of mid-to high-temperature sulfur sorbents for desulfurization of biomass-and coal-derived syngas,'' *Energy & Fuels*, vol. 23, no. 11, pp. 5291–5307, 2009.

[2] P. J. Woolcock and R. C. Brown, ''A review of cleaning technologies for biomass-derived syngas,'' *Biomass and bioenergy*, vol. 52, pp. 54–84, 2013.

[3] M. Kure, ''Hot gas cleaning,'' Master's thesis, NTNU, 2014.

[4] G. W. Huber, S. Iborra, and A. Corma, ''Synthesis of transportation fuels from biomass: Chemistry, catalysts, and engineering,'' *Chemical reviews*, vol. 106, no. 9, pp. 4044–4098, 2006.

[5] R. Luque, J. Clark, S. K. C. Lin, and K. Wilson, *Handbook of biofuels production: Processes and technologies (second edition)*. Elsevier, 2016.

[6] E. Trømborg, T. F. Bolkesjø, and B. Solberg, ''Biomass market and trade in norway: Status and future prospects,'' *Biomass and Bioenergy*, vol. 32, no. 8, pp. 660–671, 2008.

[7] F. HUANG, ''Chapter 1: What is biomass,'' in *Materials for Biofuels*, A. J. Ragauskas, Ed., World Scientific, 2014, pp. 1–26.

[8] J. Bermudez and B Fidalgo, ''Production of bio-syngas and bio-hydrogen via gasification,'' in *Handbook of Biofuels Production (Second Edition)*, Elsevier, 2016, pp. 431–494.

[9] Q. Luo, C. S. Park, A. S. Raju, and J. M. Norbeck, ''Experimental study of gaseous sulfur species formation during the steam hydrogasification of coal,'' *Energy & Fuels*, vol. 28, no. 5, pp. 3399–3402, 2014.

[10] X. Meng, W. De Jong, R. Pal, and A. H. Verkooijen, ''In bed and downstream hot gas desulphurization during solid fuel gasification: A review,'' *Fuel Processing Technology*, vol. 91, no. 8, pp. 964–981, 2010.

[11] P Mondal, G. Dang, and M. Garg, ''Syngas production through gasification and cleanup for downstream applications—recent developments,'' *Fuel Processing Technology*, vol. 92, no. 8, pp. 1395–1410, 2011.

[12] J. A. Moulijn, M. Makkee, and A. E. Van Diepen, *Chemical process technology*. John Wiley & Sons, 2013.

[13] P. Basu, *Biomass gasification and pyrolysis: practical design and theory*. Academic press, 2010.

[14] E4tech, *Review of technologies for gasification of biomass and wastes. final report*, 2009. [Online]. Available: `http://www.e4tech.com/wp-content/uploads/2016/01/gasification2009.pdf` (visited on 09/30/2017).

[15] S. Cheah, J. L. Olstad, W. S. Jablonski, and K. A. Magrini-Bair, ''Regenerable manganese-based sorbent for cleanup of simulated biomass-derived syngas,'' *Energy & Fuels*, vol. 25, no. 1, pp. 379–387, 2011.

[16] C. König, M Nachtegaal, M. Seemann, F Clemens, N van Garderen, S. Biollaz, and T. Schildhauer, ''Mechanistic studies of chemical looping desulfurization of Mn-based oxides using in situ x-ray absorption spectroscopy,'' *Applied Energy*, vol. 113, pp. 1895–1901, 2014.

[17] M. Husmann, C. Hochenauer, X. Meng, W. d. Jong, and T. Kienberger, ''Evaluation of sorbents for high temperature in situ desulfurization of biomass-derived syngas,'' *Energy & Fuels*, vol. 28, no. 4, pp. 2523–2534, 2014.

[18] P. R. Westmoreland and D. P. Harrison, ''Evaluation of candidate solids for high-temperature desulfurization of low-btu gases,'' *Environmental Science & Technology*, vol. 10, no. 7, pp. 659–661, 1976.

[19] L. F. Guo, K. L. Pan, H. M. Lee, and M. B. Chang, ''High-temperature gaseous H_2S removal by Zn -- Mn-based sorbent,'' *Industrial & Engineering Chemistry Research*, vol. 54, no. 44, pp. 11 040–11 047, 2015.

[20] Y. I. Yoon, B. H. Chun, Y. Yun, and S. H. Kim, ''A study of a regeneration reaction for desulfurization sorbents using natural manganese ore,'' *Journal of chemical engineering of Japan*, vol. 37, no. 7, pp. 835–841, 2004.

[21] W. J. Bakker, F. Kapteijn, and J. A. Moulijn, ''A high capacity manganese-based sorbent for regenerative high temperature desulfurization with direct sulfur production: Conceptual process application to coal gas cleaning,'' *Chemical Engineering Journal*, vol. 96, no. 1, pp. 223–235, 2003.

[22] W. Bakker, J. van Rossen, J. Janssens, and J. Moulijn, ''Hot gas cleaning, sulfiding mechanisms in absorption of H_2S by solids,'' in *Desulfurization of Hot Coal Gas*, A. T. Atimtay and D. P. Harrison, Eds., Springer, 1998, pp. 159–178.

[23] H. Sharifi Pajaie and M. Taghizadeh, ''Investigation of promoted $Cu/ZnO/Al_2O_3$ methanol steam reforming nanocatalysts by full factorial design,'' *Chemical Engineering & Technology*, vol. 35, no. 10, pp. 1857–1864, 2012.

[24] J Agrell, H Birgersson, M. Boutonnet, I Melián-Cabrera, R. Navarro, and J. G. Fierro, ''Production of hydrogen from methanol over Cu/ZnO catalysts promoted by ZrO_2 and Al_2O_3,'' *Journal of Catalysis*, vol. 219, no. 2, pp. 389–403, 2003.

[25] Q. Liu, F. Gu, Z. Zhong, G. Xu, and F. Su, ''Anti-sintering ZrO_2 modified ni/α-Al_2O_3 catalyst for co methanation,'' *RSC Advances*, vol. 6, no. 25, pp. 20 979–20 986, 2016.

[26] K. P. de Jong, *Synthesis of solid catalysts*. John Wiley & Sons, 2009.

[27] M. Lok, ''Coprecipitation,'' in *Synthesis of solid catalysts*, K. P. de Jong, Ed., John Wiley & Sons, 2009, pp. 135–149.

[28] I Chorkendorff and J. W. Niemantsverdriet, ''Coprecipitation,'' in *Concepts of modern catalysis and kinetics*, John Wiley & Sons, 2007, p. 197.

[29] F. Schüth and K. K. Unger, ''Precipitation and coprecipitation,'' in *Preparation of solid catalysts*, G. Ertl, H. KnÃ, J. Weitkamp, *et al.*, Eds., John Wiley & Sons, 2008, pp. 60–84.

[30] I. Chorkendorff and J. Niemantsverdriet, *Concepts of Modern Catalysis and Kinetics*. Wiley-VCH, 2003, 131–133 and 154 and 187.

[31] K. Sing, ''Adsorption methods for the characterization of porous materials,'' *Advances in Colloid and Interface Science*, vol. 76-77, no. 0, pp. 3–11, 1998.

[32] K. Sing, ''The use of nitrogen adsorption for the characterisation of porous materials,'' *Colloids and Surfaces A: Physicochemical and Engineering Aspects*, vol. 187-188, no. 0, pp. 3–9, 2001.

[33] S. Brunauer, E. P.H., and E Teller, ''Adsorption of gases in multimolecular layers,'' *Journal of the American Chemical Society*, vol. 60, no. 2, pp. 309–319, 1938.

[34] F. Kleitz, ''Ordered microporous and mesoporous materials,'' *Nanoscale Materials in Chemistry*, pp. 243–329, 2009.

[35] A. C. Mitropoulos, ''The kelvin equation,'' *Journal of colloid and interface science*, vol. 317, no. 2, pp. 643–648, 2008.

[36] W. Wang, P. Liu, M. Zhang, J. Hu, and F. Xing, ''The pore structure of phosphoaluminate cement,'' *Open Journal of Composite Materials*, vol. 2, no. 03, p. 104, 2012.

[37] M. Che and J. C. Védrine, *Characterization of solid materials and heterogeneous catalysts: From structure to surface reactivity*. John Wiley & Sons, 2012.

[38] K. Singh, J Rouquerol, G Bergeret, P Gallezot, M Vaarkamp, D. Koningsberger, A. Datye, J. Niemantsverdriet, T Butz, G Engelhardt, *et al.*, ''Characterization of solid catalysts: Sections 3.1. 1--3.1. 3,'' in *Handbook of Heterogeneous Catalysis*, G. Ertl, H. Knözinger, and J. Weitkamp, Eds., Wiley Online Library, 2008, pp. 582–689.

[39] N. Saenko, ''The x-ray diffraction study of three-dimensional disordered network of nanographites: Experiment and theory,'' *Physics Procedia*, vol. 23, pp. 102–105, 2012.

[40] F Kapteijn, J. Moulijn, and A Tarfaoui, ''Catalyst characterization and mimicking pretreatment procedures by temperature-programmed techniques,'' in *Catalysis: An Integrated Approach, Second Edition (Studies in Surface Science and Catalysis)*, J. Moulijn, B. Averill, P. van Leeuwen, and R. van Santen, Eds., Elsevier, 1999, pp. 525–541.

[41] J. Le Page, D Avnir, E Taglauer, M Guisnet, G Moretti, M Che, F Bozon-Verduraz, M Anpo, E Roduner, and H Knözinger, ''Characterization of solid catalysts: Sections 3.1.4-3.2.2,'' in *Handbook of Heterogeneous Catalysis*, G. Ertl, H. Knözinger, and J. Weitkamp, Eds., Wiley Online Library, 2008, pp. 582–689.

[42] Micromeritics, *Temperature-programmed reduction*. [Online]. Available: `http://www.micromeritics.com/Repository/Files/appnote120.pdf` (visited on 10/15/2017).

[43] P. Potts, ''X-ray fluorescence analysis: Principles and practice of wavelength dispersive spectrometry,'' in *A Handbook of Silicate Rock Analysis*, Springer, 1987, pp. 226–285.

[44] M. S. Shackley, ''An introduction to x-ray fluorescence (xrf) analysis in archaeology,'' in *X-ray fluorescence spectrometry (XRF) in geoarchaeology*, Springer, 2011, pp. 7–44.

[45] J. Niemantsverdriet, ''Microscopy and imaging,'' in *Spectroscopy in catalysis: an introduction*, Wiley Online Library, 2007, pp. 180–186.

[46] Y. Leng, ''Scanning electron microscope,'' in *Materials characterization: introduction to microscopic and spectroscopic methods, 2nd Edition*, John Wiley & Sons, 2013, pp. 127–162.

[47] Y. Wang and V. Petrova, ''Scanning electron microscopy,'' in *Nanotechnology research methods for food and bioproducts*, G. W. Padua and Q. Wang, Eds., John Wiley & Sons, 2012, pp. 103–126.

[48] Technoorg Linda, *High-resolution scanning electron microscopy*. [Online]. Available: `http://www.technoorg.hu/news-and-events/articles/high-resolution-scanning-electron-microscopy-1/` (visited on 06/02/2018).

[49] P. J. Wakker, A. Gerritsen, and J. A. Moulijn, ''High temperature H_2S and COS removal with MnO and FeO on - gamma-alumina acceptors,'' *Industrial and Engineering Chemistry Research*, vol. 32, pp. 139–149, 1993.

[50] B Liang, R Korbee, A. Gerritsen, and C. Van den Bleek, ''Effect of manganese content on the properties of high temperature regenerative H_2S acceptor,'' *Fuel*, vol. 78, no. 3, pp. 319–325, 1999.

[51] J Szekely, J. Evans, and H. Sohn, *Gas-Solid Reactions*. Academic Press, 1976.

[52] B. R. Strohmeier and D. M. Hercules, ''Surface spectroscopic characterization of manganese/aluminum oxide catalysts,'' *The Journal of Physical Chemistry*, vol. 88, no. 21, pp. 4922–4929, 1984.

[53] F. Kapteijn, A. D. Vanlangeveld, J. A. Moulijn, A. Andreini, M. A. Vuurman, A. M. Turek, J.-M. Jehng, and I. E. Wachs, ''Alumina-supported manganese oxide catalysts: I. characterization: Effect of precursor and loading,'' *Journal of Catalysis*, vol. 150, no. 1, pp. 94–104, 1994.

[54] J. Carnö, M. Ferrandon, E. Björnbom, and S. Järås, ''Mixed manganese oxide/platinum catalysts for total oxidation of model gas from wood boilers,'' *Applied Catalysis A: General*, vol. 155, no. 2, pp. 265–281, 1997.

[55] S. Chytil, M. Kure, R. Lødeng, and E. A. Blekkan, ''On the initial deactivation of Mn_xO_y -- Al_2O_3 sorbents for high temperature removal of H_2S from producer gas,'' *Fuel Processing Technology*, vol. 133, pp. 183–194, 2015.

[56] S. Chytil, M. Kure, R. Lødeng, and E. A. Blekkan, ''Performance of mn-based H_2S sorbents in dry, reducing atmosphere. manganese oxide support effects,'' *Fuel*, vol. 196, pp. 124–133, 2017.

[57] I Chorkendorff and J. W. Niemantsverdriet, ''Catalyst characterization,'' in *Concepts of modern catalysis and kinetics*, John Wiley & Sons, 2013, pp. 131–134.

[58] C. H. Bartholomew and R. J. Farrauto, ''Catalyst characterization and selection,'' in *Fundamentals of industrial catalytic processes*, Blackie Academic and Professional, 1997, p. 138.

[59] S. Nair and B. J. Tatarchuk, ''Supported silver adsorbents for selective removal of sulfur species from hydrocarbon fuels,'' *Fuel*, vol. 89, no. 11, pp. 3218–3225, 2010.

[60] O. A. Bulavchenko, T. N. Afonasenko, P. G. Tsyrul'nikov, and S. V. Tsybulya, ''Effect of heat treatment conditions on the structure and catalytic properties of $MnOx/Al_2O_3$ in the reaction of CO oxidation,'' *Applied Catalysis A: General*, vol. 459, pp. 73–80, 2013.

[61] J. Wang, B. Liang, and R. Parnas, ''Manganese-based regenerable sorbents for high temperature H_2S removal,'' *Fuel*, vol. 107, pp. 539–546, 2013.

[62] R. H. Nielsen and G. Wilfing, ''Zirconium and zirconium compounds,'' in *Ullmann's Encyclopedia of Industrial Chemistry 7th. edition*, B. Elvers, Ed., Wiley Online Library, 2012, pp. 753–776.

[63] A. H. Dam, ''Steam reforming of ethanol over Ni and Co hydrotalcite-derived catalysts,'' 2015.

Appendices

Appendix A

Risk Assessment

ID	23694	**Status**	**Date**
Risk Area	Risikovurdering: Helse, miljø og sikkerhet (HMS)	Created	03.10.2017
Created by	Siri Stavnes	Assessment started	03.10.2017
Responsible	Siri Stavnes	Actions decided	
		Closed	

Risk Assessment:

CAT, Master student, 2018, Siri Stavnes

Valid from-to date:

-

Location:

Chemistry block 5, Chemistry Hall D-144

Goal / purpose

This risk assessment comprises the preaparation and characterization of the sorbent materials used in a chemical looping desulphurization setup located in the Chemistry Hall D 1st floor (Unit 1.2). The risk assessments related to this setup can be obtained from ID 23777 and ID 23714. The sorbent materials used in the setup are characterized using various techniques.

Background

- Characterization techniques: N2-adsorption, XRF, XRD, TPR, SEM
- Sorbents: Zr-promoted Mn-oxides supported on gamma alumina (Al2O3)
- Chemicals: Support: gamma alumina and Al(NO3)3·9H2O ; Precursors: Mn(NO3)2•4H2O and (ZrO(NO3)2) ; Precipitating agents: NaOH and Na2CO3.
- The sorbents were calcined in air using a calcination setup
- Sorption-regeneration experiments were performed on the preapred sorbents using a desulphurization setup (ID 23777 and ID 23714)

Description and limitations

H2S is a toxic gas. Safety data sheet is attached.

Prerequesites, assumptions and simplifications

[Ingen registreringer]

Attachments

Safety data sheet Hydrogen sulphide.pdf

References

[Ingen registreringer]

Summary, result and final evaluation

The summary presents an overview of hazards and incidents, in addtition to risk result for each consequence area.

Hazard: **Nitrogen adsorption analysis**

Incident: **Contact with liquid nitrogen (N2)**

Consequence area: Helse Risk before actions: Risiko after actions:

Hazard: **X-ray exposure when using XRD and XRF**

Incident: **Exposed to radiation from X-ray**

Consequence area: Helse Risk before actions: Risiko after actions:

Hazard: **Calcination setup**

Incident: **Skin burns**

Consequence area: Helse Risk before actions: Risiko after actions:

Hazard: **H2S set-up (Refer to ID 23777 and ID 23714)**

Incident:

Not to be analyzes.

Hazard: **H2S**

Incident:

Not to be analyzes.

Hazard: **Sorbent preparation**

Incident: **Inhalation of dust**

Consequence area: Helse Risk before actions: Risiko after actions:

Final evaluation

Organizational units and people involved

A risk assessment may apply to one or more organizational units, and involve several people. These are lsited below.

Organizational units which this risk assessment applies to

- Institutt for kjemisk prosessteknologi

Participants

Karin Wiggen Dragsten
Edd Anders Blekkan
Kumar Ranjan Rout
Jianyu Ma

Readers

[Ingen registreringer]

Others involved/stakeholders

[Ingen registreringer]

The following accept criteria have been decided for the risk area Risikovurdering: Helse, miljø og sikkerhet (HMS):

Helse	Materielle verdier	Omdømme	Ytre miljø
			

Overview of existing relevant measures which have been taken into account

The table below presents existing measures which have been take into account when assessing the likelihood and consequence of relevant incidents.

Hazard	Incident	Measures taken into account
Nitrogen adsorption analysis	Contact with liquid nitrogen (N2)	Safety protective equipment
	Contact with liquid nitrogen (N2)	Transporting chemical bottles
X-ray exposure when using XRD and XRF	Exposed to radiation from X-ray	
Calcination setup	Skin burns	Safety protective equipment
Sorbent preparation	Inhalation of dust	Safety protective equipment
	Inhalation of dust	Fume cupboards

Existing relevant measures with descriptions:

Safety protective equipment

- Laboratory coat
- Safety googles
- Insulating gloves
- Protective gloves

Waste disposal/handling

Infectious waste, radioactive waste, explosive and/or spontaneously flammable chemicals should not be mixed with other chemical waste.

Correct storage of chemicals

Chemicals should be stored in chemical cabinets

Correct labelling of chemicals

All samples should be labelled according to regulation:
- Name of sample/chemical
- Name of person that made the solution
- Production date
- Hazard symbol

- Place a round coloured label on the lid with initials on it. The colour changes every year.

Transporting chemical bottles

Bottles with liquid chemicals are placed in a plastic bucket with a solid handle.

Gas detection

1. Small handheld detectors
2. Permanent installed systems
- Local warning at low and high alarm (blue lamp)
- Local power shutoff at high alarm (buzzer + red lamp)

Gas leakage test

Handheld detectors:
- CO-detector (cross sensitive to H2, not sensitive to hydrocarbons)
- Flammable gas detector (hydrocarbons and H2)

Detection spray

Fire alarms

[Ingen registreringer]

Emergency system to cut the power (heat and electricity)

[Ingen registreringer]

Fume cupboards

Use a fume cupboard when handling chemicals or materials that might lead to:
- hazardous or flammable/explosive vapours
- dust
- bothersome smells

Working alone in laboratories

Requirements for working alone outside normal working hours in laboartories (after 16:00 and in weekends):
- Risk assessment
- Written authorization
- Working alone alarm

Risk analysis with evaluation of likelihood and consequence

This part of the report presents detailed documentation of hazards, incidents and causes which have been evaluated. A summary of hazards and associated incidents is listed at the beginning.

The following hazards and incidents has been evaluated in this risk assessment:

- **Nitrogen adsorption analysis**
  - Contact with liquid nitrogen (N2)
- **X-ray exposure when using XRD and XRF**
  - Exposed to radiation from X-ray
- **Calcination setup**
  - Skin burns
- **Sorbent preparation**
  - Inhalation of dust

Detailed view of hazards and incidents:

Hazard: Nitrogen adsorption analysis

Contact with liquid nitrogen

Incident: Contact with liquid nitrogen (N2)

Cause: Not wearing the appropriate safety equipments

Description:

Safety goggles, lab coat, Isolating gloves, closed shoes

Likelihood of the incident (common to all consequence areas): **Less likely (2)**

Kommentar:

Always wear the the correct safety equipment. Correctly transport the liquid nitrogen in a dewar placed in a plastic bucket with a solid handle.

Consequence area: Helse

Risk:

Assessed consequence: **Medium (2)**

Comment: [Ingen registreringer]

Hazard: X-ray exposure when using XRD and XRF

Incident: Exposed to radiation from X-ray

Likelihood of the incident (common to all consequence areas): **Unlikely (1)**

Kommentar:
[Ingen registreringer]

Consequence area: Helse

Assessed consequence: **Very large (4)**

Comment: [Ingen registreringer]

Risk:

Hazard: Calcination setup

Incident: Skin burns

High temperature in calcination reactor (and furnace)

Cause: Not wearing the appropriate safety equipments

Description:
Gloves

Likelihood of the incident (common to all consequence areas): **Less likely (2)**

Kommentar:
Always wear the the correct safety equipment

Consequence area: Helse

Assessed consequence: **Medium (2)**

Comment: [Ingen registreringer]

Risk:

Hazard: Sorbent preparation

Incident: Inhalation of dust

Likelihood of the incident (common to all consequence areas): **Less likely (2)**

Kommentar:

Always wear the the correct safety equipment. Work in a fume cupboard when handling chemicals or materials that might lead to dust.

Consequence area: Helse

Risk:

Assessed consequence: **Medium (2)**

Comment: [Ingen registreringer]

Overview of risk mitiating actions which have been decided:

Below is an overview of risk mitigating actions, which are intended to contribute towards minimizing the likelihood and/or consequence of incidents:

Overview of risk mitigating actions which have been decided, with description:

Detailed view of assessed risk for each hazard/incident before and after mitigating actions

Appendix B

Calculations for Sorbent Preparation

B.1 Incipient Wetness Impregnation

Table B.1: Sorbents prepared by incipient wetness impregnation

Sorbent	Mn loading [wt%]	Zr loading [wt%]	Al_2O_3 loading [wt%]	Calcination temp.	[°C]
(1) Mn/γ-Al_2O_3	15	0	85	500	700
(2) Mn-Zr/γ-Al_2O_3	15	1	84	500	700
(3) Mn-Zr/γ-Al_2O_3	15	5	80	500	700
(4) Mn-Zr/γ-Al_2O_3	15	10	75	500	700

Basic information

- Molecular weight of Mn = 55 g/mol
- Molecular weight of Mn-precursor ($(Mn(NO_3)_2 \cdot 4H_2O)$) = 251 g/mol
- Molecular weight of Zr = 91 g/mol
- Molecular weight of Zr-precursor ($ZrO(NO_3)_2$) = 231 g/mol

Amount of precursor

Basis: 1g support

Amount of Mn-precursor:

$$\text{Mass of Mn-precursor} := \frac{m_{Mn}}{MW_{Mn}} \cdot MW_{Mn(NO_3)_2} \tag{B.1}$$

$$m_{Mn} = \frac{wt\%Mn}{wt\%Al_2O_3} \tag{B.2}$$

35wt% of the Zr-precursor ($ZrO(NO_3)_2$) is diluted in nitric acid. The amount of Zr-solution is:

$$\text{Mass of Zr-precursor} := \frac{m_{Zr}}{MW_{Zr} \cdot 0.35} \cdot MW_{ZrO(NO_3)_2} \tag{B.3}$$

$$m_{Zr} = \frac{wt\%Zr}{wt\%Al_2O_3} \tag{B.4}$$

Volume of water in precursor

In 1 mol Mn-precursor, which is equal to 251g, the amount of water is:

$$\text{Mass of water} : m_{H_2O} = n_{H_2O} \cdot MW_{H_2O} \tag{B.5}$$

(B.6)

Total amount of water in Mn-precursor:

$$\text{Mass of water Mn-precursor} : m_{Mn_{precursor}} = \frac{n_{H_2O} \cdot MW_{H_2O}}{MW_{Mn(NO_3)_2 \cdot 4H_2O}} \cdot m_{Mn(NO_3)_2 \cdot 4H_2O} \tag{B.7}$$

Volume of water in Mn-precursor salt:

$$\text{Volume of water Mn-precursor} : V_{H_2O} = \frac{m_{H_2O}}{\rho_{H_2O}} \tag{B.8}$$

For the Zr-precursor, where 35% of the precursor is diluted in nitric acid, the mass of water is:

$$\text{Mass of water Zr-precursor}: m_{Zr-precursor} = (1 - 0.35) \cdot m_{ZrO(NO_3)_2} \tag{B.9}$$

Capacity of 1g alumina support (pore volume) = 1.3 mL.
The volume of water required to dissolve the precursors per 1 gram support is:

$$\text{Amount water required}: m_{H_2O} = 1.3 - m_{H_2O(\text{Mn-precursor})} - m_{H_2O(\text{Zr-precursor})} \tag{B.10}$$

B.2 Co-precipitation

Table B.2: Sorbents prepared by co-precipitation

Sorbent	Mn loading [wt%]	Zr loading [wt%]	Calcination temp.	[°C]
(1) Mn/γ-Al_2O_3	15	0	500	700
(2) Mn-Zr/γ-Al_2O_3	15	1	500	700
(3) Mn-Zr/γ-Al_2O_3	15	10	500	700

The estimated composition of Mn/Al_2O_3 and Zr-modified Mn/Al_2O_3 sorbents are calculated in the following sections.

The mol number of Mn^{2+}, Zr^{4+}, Al^{3+}, OH^- and $CO_3{}^{2-}$ are denoted as x, y, z, a and b, respectively. The molar masses of reactants used during preparation are given in Table B.3.

Table B.3: Molar masses of reactants

	Component	Molar mass [g/mol]
Precursor	$Mn(NO_3)_2 \cdot 4H_2O$	251
	ZrN_2O_7	231
	$Al(NO_3)_3 \cdot 9H_2O$	375
Precipitating agent	NaOH	40
	Na_2CO_3	106
	Mn	55
	Al_2O_3	102
	Zr	91

Need to solve three (3) equation sets to find x, y and Z

- An expression for y (mol Zr^{4+}) can be obtained from equation B.12
- An expression for z (mol Al^{3+}) can be obtained from equation B.13

  NB! Al_2O_3 contain 2 Al^{3+} ions
- Insertion in equation B.11 give x (mol Mn^{2+})

$$2x + 4y + 3z = 18 \tag{B.11}$$

$$55x = 15 \cdot 91y \tag{B.12}$$

$$\frac{55x}{15} \cdot 84 = \frac{z}{2} \cdot 102 \tag{B.13}$$

The resulting molar composition is given in Table B.4.

Table B.4: Stoichiometric coefficients for the ions constituting the prepared sorbents

Sorbent	Metal loading [wt%]			Mol number				
	Mn	Zr	Al_2O_3	x	y	z	a ⋆	b ⋆
Mn15/γ-Al_2O_3	15	0	85	0.95	-	5.37	16	1.5
Mn15-Zr1/γ-Al_2O_3	15	1	84	0.89	0.04	5.36	16	1.5
Mn15-Zr10/γ-Al_2O_3 †	15	10	75	0.93	0.31	4.97	16	1.5

x = mol Mn^{2+}; y = mol Zr^{4+}; z = mol Al^{3+}; a = mol OH^-; b = mol $CO_3{}^{2-}$

⋆ Constant, retrieved from [63]

† Calculation error. The given values corresponds to approx. 8.5wt% Zr

When calculating the amount of reactants one must consider the carbonate to aluminium ratio, hence mol $CO_3{}^{2-}$ = 0.0375.

Table B.5: Mass of reactants. Basis: 1 g sorbent

Sorbent	$Mn(NO_3)_2 \cdot 4H_2O$	ZrN_2O_7	$Al(NO_3)_3 \cdot 9H_2O$	NaOH	Na_2CO_3
Mn15/γ-Al_2O_3	5.96	-	50.36	16	3.98
Mn15-Zr1/γ-Al_2O_3	5.57	0.59	50.27	16	3.98
Mn15-Zr10/γ-Al_2O_3	5.84	2.63	46.61	16	3.98

Calculation example for Zr1-Mn15/Al_2O_3

Find an expression for z:

$$\frac{55x}{15} \cdot 84 = \frac{z}{2} \cdot 102$$
$$z = \frac{308}{51}x$$

Find an expression for y:

$$55x = 15 \cdot 91y$$
$$y = \frac{55}{1365}x$$

Insert and find x:

$$2x + 4y + 3z = 18$$
$$2x + 4 \cdot \frac{55}{1365}x + 3 \cdot \frac{308}{55}x = 18$$
$$x = 0.9493 = molMn^{2+}$$

y and z can then be found by inserting x in the above equations.

Appendix C

Calibration of Mass Flow Controllers

Calibration data measured at 23 ℃ and 1 atm

Air

Channel: 1
User tag: O2

Valve opening [%]	Volume [mL]	Corrected volume	Time [s]	Flow rate [mL/min]
0	-	-	-	0
2	1	0,98494942	4,376	13,50479095
5	9	8,864544782	17,642	30,14809471
10	9	8,864544782	9,102	58,43470522
15	9	8,864544782	6,079	87,49345072
20	9	8,864544782	4,512	117,8795849
25	9	8,864544782	3,641	146,0787385
30	9	8,864544782	3,031	175,4776268

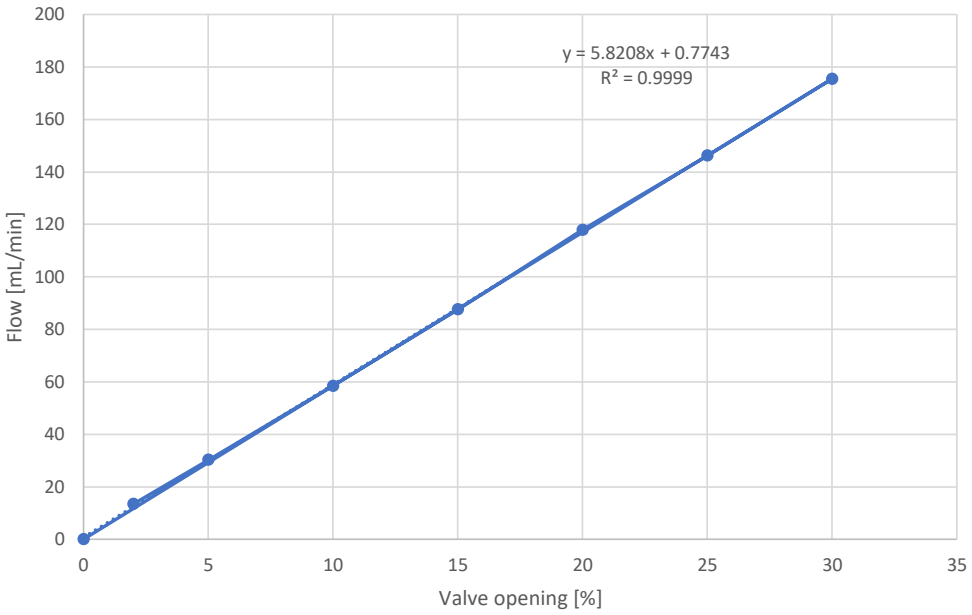

Hydrogen

Channel: 2
User tag: H2

Valve opening [%]	Volume [mL]	Corrected volume	Time [s]	Flow rate [mL/min]
0	-	-	-	0
2	1	0,98198865	5,077	11,60514458
5	9	8,837897853	19,309	27,46252376
10	9	8,837897853	9,709	54,61673408
15	9	8,837897853	6,531	81,19336567
20	9	8,837897853	4,918	107,8230726
25	9	8,837897853	3,923	135,1704999
30	9	8,837897853	3,218	164,7836766

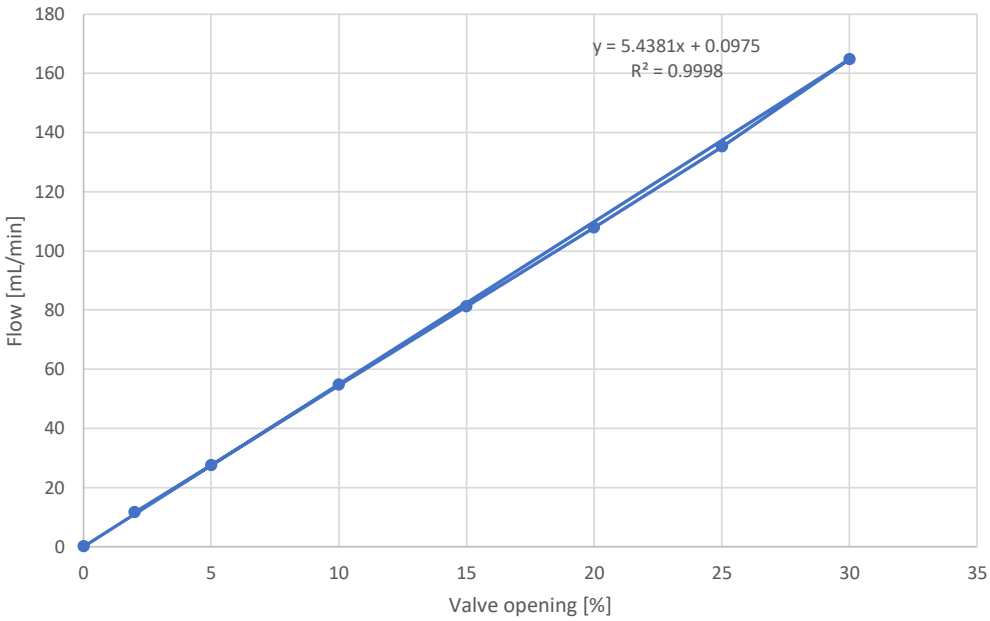

Hydrogen sulfide

Channel: 3
User tag: H2SMIX

Valve opening [%]	Volume [mL]	Corrected volume	Time [s]	Flow rate [mL/min]
0	-	-	-	0
2	1	4,331	1,006661732	13,94590255
5	9	15,742	9,059955588	34,53165642
7	9	11,319	9,059955588	48,02520853
10	9	7,982	9,059955588	68,10289843
15	9	5,33	9,059955588	101,988243
20	9	4,008	9,059955588	135,6280777
25	9	3,235	9,059955588	168,0362706
30	90	26,248	90,59955588	207,1004782

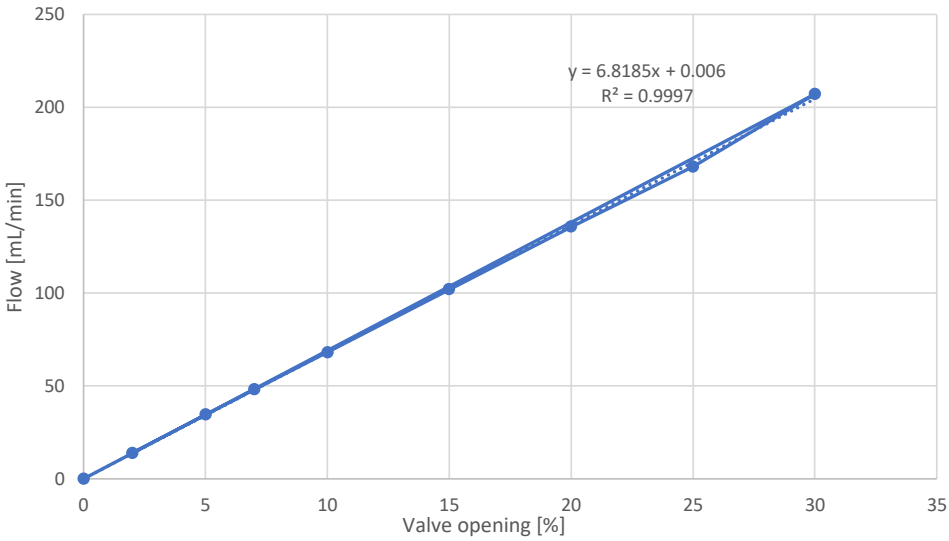

Nitrogen

Channel: 4
User tag: N2

Valve opening [%]	Volume [mL]	Corrected volume	Time [s]	Flow rate [mL/min]
0	-	-	-	0
2	1	0,98198865	5,648	10,43189076
5	9	8,837897853	19,739	26,86427231
10	9	8,837897853	9,812	54,0434031
15	9	8,837897853	6,498	81,60570502
20	9	8,837897853	4,864	109,0201215
25	9	8,837897853	3,848	137,8050601
30	9	8,837897853	3,202	165,6070803

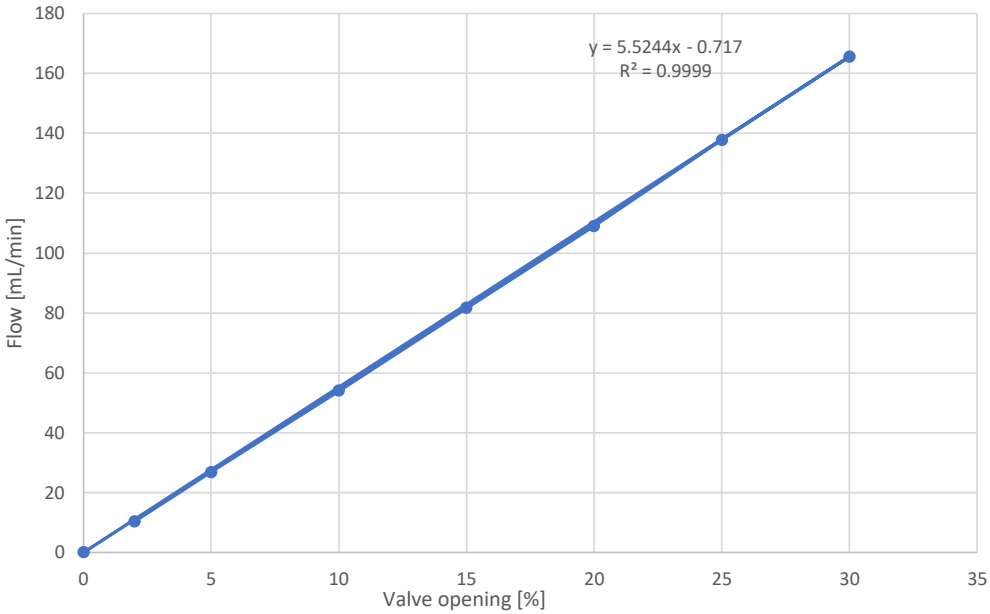

Appendix D

Sorption Capacity Calculations

The total amount of H_2S removed by the sorbent is found by equation D.1:

$$IC = a \cdot [C] + b \tag{D.1}$$

Where:

- a and b: ion current signals
- C: concentration of H_2S

Calculations for Zr1-Mn15/Al_2O_3 sorbent

Sorbent prepared by incipient wetness impregnation and calcined at 700° C

Concentration of H_2S [ppm] is calculated from the ion current signal obtained from the mass spectrometer after analysis using equation D.1:

$$[C] = \frac{IC - b}{a} = \frac{IC - b}{IC_{max} - b} \cdot 4000 = \frac{IC - 1.3 * 10^{-10}}{IC_{max} - 1.3 * 10^{-10}} \cdot 4000$$

The maximum amount H_2S removed is found by converting ppm to mL:

1 mL = 1 ppm , where 1 ppm = 10^{-6}.
Total gas flow: 100 mL/min

$$10^{-6} \cdot \frac{100\text{mL}}{\text{min}} * \frac{1\text{min}}{60s} = \frac{1}{600000}\text{mL/s}$$

Breakthrough sorption capacity:

Table D.1: Breakthrough sorption capacity for Zr1-Mn15/Al_2O_3, prepared by incipient wetness impregnation and calcined at 700°C

Cycle	[1] Maximum amount of H_2S removed [mL/s]	[2] Time for sorption breakthrough [s]	[4] Maximum amount of H_2S removed [mol]	[3] Sorption capacity [mmolH_2S/ g sorbent]
1	0.006780	1191	3.36E-04	1.679994597
2	0.006775	1122	3.16E-04	1.581663769
3	0.006776	1093	3.08E-04	1.539851637
4	0.006773	966	2.72E-04	1.361050409
5	0.006766	956	2.69E-04	1.345489743
6	0.006768	1027	2.89E-04	1.446308087
7	0.006771	1020	2.87E-04	1.435901241
8	0.006770	1023	2.88E-04	1.440168245
9	0.006637	1011	2.79E-04	1.395572812
10	0.006770	1003	2.83E-04	1.41298968

[1] Calculated from the assumption of a linear relationship between the ion current signal and H_2S concentration
[2] Calculated as the difference between the time when the sorption gas is switched to the reactor and the time when the H_2S concentration start to increase
[3] Mol H_2S removed = (time for sorption breakthrough [s] · maximum H_2S [mL/s]) / (24.04 L/mol · 1000 mL/L)
[4] Breakthrough sorption capacity: H_2S [mmol]/ mass of sorbent [g] = (maximum amount H_2S removed [mol] / 200 mg sorbent) · (1000 mg / 1 g sorbent)

Appendix E

Nitrogen Adsorption Summary Reports

Summary reports for fresh and reacted $Mn15/Al_2O_3$ sorbent, preapred by incipient wetness impregnation and calcined at 700∘C, are included in this appendix.

$Mn15/Al_2O_3$ sorbent

Fresh sorbent prepared by incipient wetness impregnation and calcined at 700°C.

Micromeritics Instrument Corporation

TriStar II 3020 Unit 1 Port 3

Sample:	15 wt.% Mn on Alumina calcined 700
Operator:	Siri
Submitter:	Siri
File:	C:\TriStar II 3020\data\Siri S\000-126.SMP

Started:	06.04.2018 17:09:38	Analysis Adsorptive:	N2
Completed:	06.04.2018 22:45:16	Analysis Bath Temp.:	-195,850 °C
Report Time:	08.04.2018 11:30:57	Thermal Correction:	No
Sample Mass:	0,1043 g	Warm Free Space:	11,6447 cm³ Measured
Cold Free Space:	34,4415 cm³	Equilibration Interval:	5 s
Low Pressure Dose:	None	Sample Density:	1,000 g/cm³
Automatic Degas:	No		

Summary Report

Surface Area

Single point surface area at p/p° = 0,299608027:	127,6463 m²/g
BET Surface Area:	130,7793 m²/g
Langmuir Surface Area:	207,0297 m²/g
t-Plot Micropore Area:	5,8775 m²/g
t-Plot External Surface Area:	124,9018 m²/g
BJH Adsorption cumulative surface area of pores between 17,000 Å and 3 000,000 Å width:	142.890 m²/g
BJH Desorption cumulative surface area of pores between 17,000 Å and 3 000,000 Å width:	150,5971 m²/g

Pore Volume

Single point adsorption total pore volume of pores less than 863,215 Å width at p/p° = 0,977047805:	0,426471 cm^3/g
t-Plot micropore volume:	0,002075 cm^3/g
BJH Adsorption cumulative volume of pores between 17,000 Å and 3 000,000 Å width:	0,450556 cm^3/g
BJH Desorption cumulative volume of pores between 17,000 Å and 3 000,000 Å width:	0,461321 cm^3/g

Pore Size

Adsorption average pore diameter (4V/A by BET):	130,4399 Å
BJH Adsorption average pore width (4V/A):	126,127 Å
BJH Desorption average pore width (4V/A):	122,531 Å

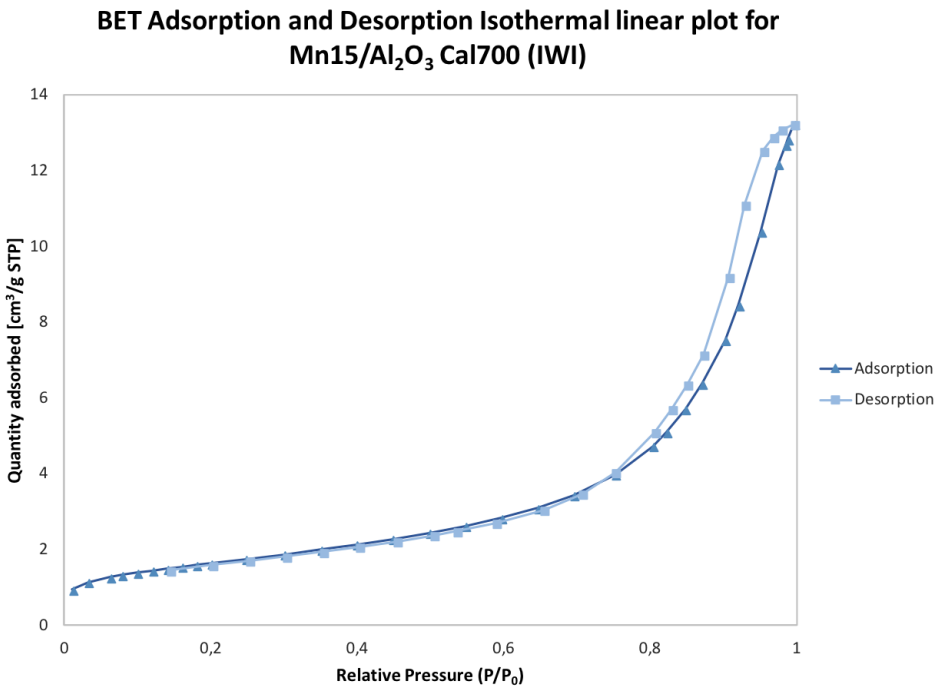

Figure E.1: N_2 adsorption and desorption isotherms for fresh Mn15/Al_2O_3 sorbent prepared by incipient wetness impregnation (IWI) and calcined at 700°C after 10 sorption and regeneration cycles

Mn15/Al_2O_3 sorbent

Reacted sorbent (after 10 cycles of sorption- and regeneration) prepared by incipient wetness impregnation and calcined at 700°C.

Micromeritics Instrument Corporation

TriStar II 3020 3.02 Unit 1 Port 1

Sample:	15Mn/Al2O3_700_reacted_10cycles
Operator:	Siri
Submitter:	Siri
File:	C:\TriStar II 3020\data\Siri Stavnes\000-238.SMP

Started:	06.05.2018 11:38:15	Analysis Adsorptive:	N2
Completed:	06.05.2018 17:08:48	Analysis Bath Temp.:	-195,850 °C
Report Time:	06.05.2018 19:58:15	Thermal Correction:	No
Sample Mass:	0,0977 g	Warm Free Space:	11,8312 cm³ Measured
Cold Free Space:	35,2631 cm³	Equilibration Interval:	5 s
Low Pressure Dose:	None	Sample Density:	1,000 g/cm³
Automatic Degas:	No		

Summary Report

Surface Area

Single point surface area at p/p° = 0,299897002:	115,7669 m²/g
BET Surface Area:	118,0769 m²/g
Langmuir Surface Area:	185,8971 m²/g
t-Plot Micropore Area:	11,2788 m²/g
t-Plot External Surface Area:	106,7981 m²/g
BJH Adsorption cumulative surface area of pores between 17,000 Å and 3 000,000 Å width:	120.717 m²/g
BJH Desorption cumulative surface area of pores between 17,000 Å and 3 000,000 Å width:	124,7679 m²/g

Pore Volume

Single point adsorption total pore volume of pores less than 863,215 Å width at p/p° = 0,977047805:	0,359504 cm³/g
t-Plot micropore volume:	0,005216 cm³/g
BJH Adsorption cumulative volume of pores between 17,000 Å and 3 000,000 Å width:	0,388807 cm³/g
BJH Desorption cumulative volume of pores between 17,000 Å and 3 000,000 Å width:	0,399675 cm³/g

Pore Size

Adsorption average pore diameter (4V/A by BET):	121,7864 Å
BJH Adsorption average pore width (4V/A):	128,833 Å
BJH Desorption average pore width (4V/A):	128,134 Å

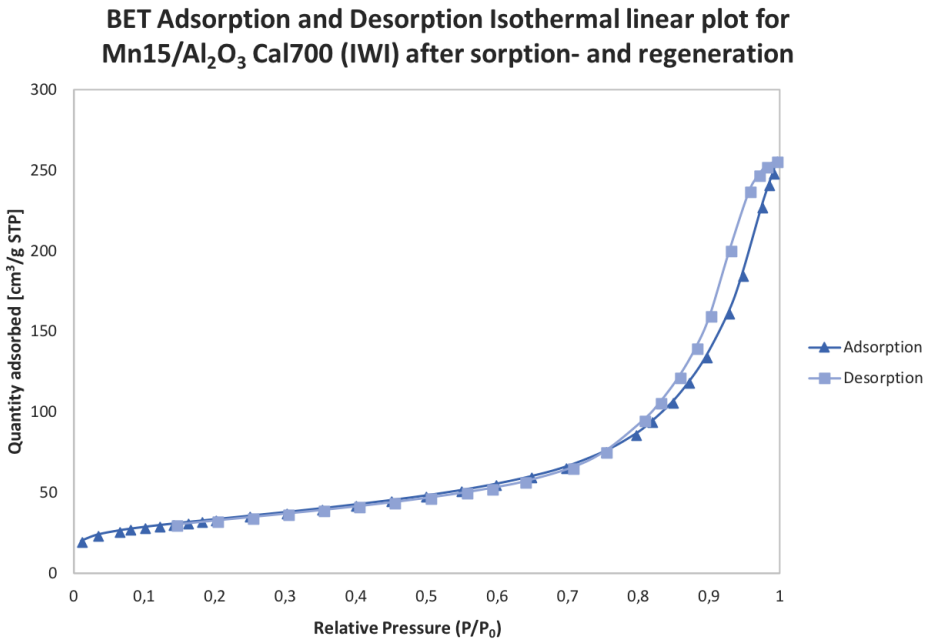

Figure E.2: N_2 adsorption and desorption isotherms for Mn15/Al_2O_3 sorbent prepared by incipient wetness impregnation (IWI) and calcined at 700°C after 10 sorption and regeneration cycles

Appendix F

XRD Diffractograms

The oxide phases for fresh and reacted sorbents were identified by a search and match analysis, and the results are presented here.

Diffractograms for fresh sorbents prepared by incipient wetness impregnation and calcined at 500°C

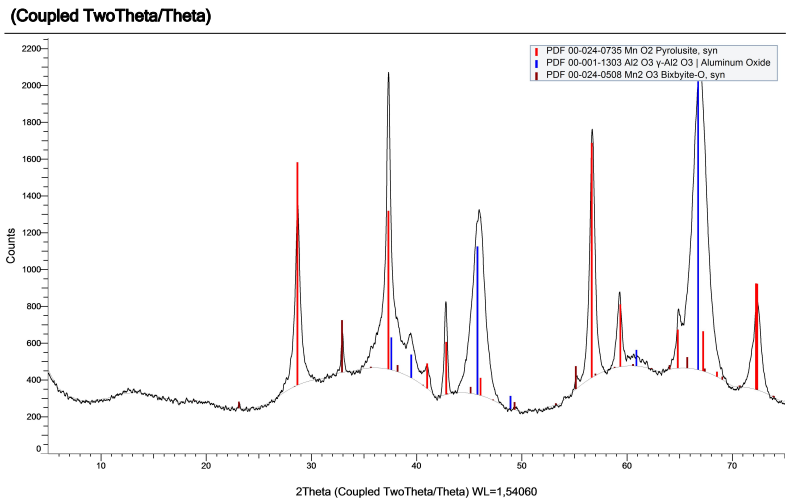

Figure F.1: Diffractogram for fresh Mn15/Al_2O_3 sorbent prepared by incipient wetness impregnation and calcined at 500°C

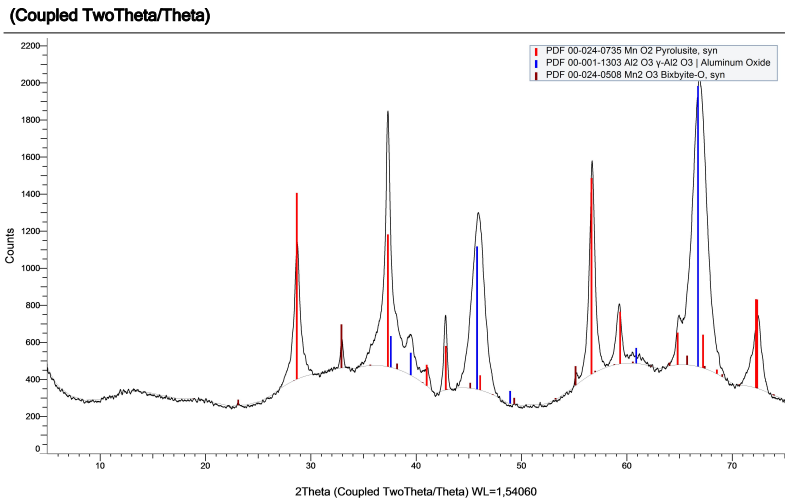

Figure F.2: Diffractogram for fresh Zr1-Mn15/Al_2O_3 sorbent prepared by incipient wetness impregnation and calcined at 500°C

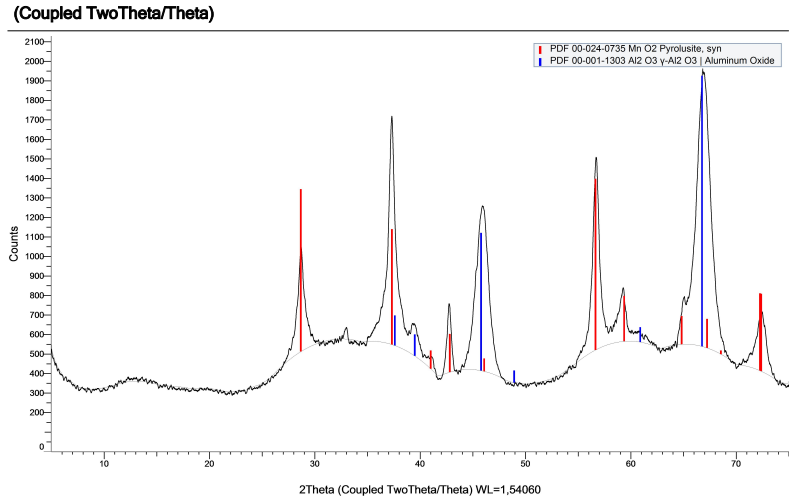

Figure F.3: Diffractogram for fresh Zr5-Mn15/Al_2O_3 sorbent prepared by incipient wetness impregnation and calcined at 500°C

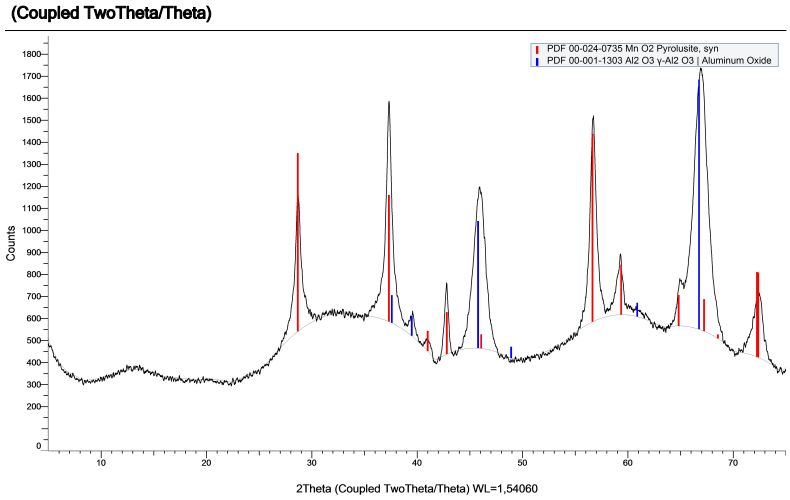

Figure F.4: Diffractogram for fresh Zr10-Mn15/Al_2O_3 sorbent prepared by incipient wetness impregnation and calcined at 500°C

Diffractograms for fresh sorbents prepared by incipient wetness impregnation and calcined at 700°C

The same phases was identified on all fresh sorbents calcined at 700°C. Hence, only one diffractogram is presented here ($Zr10\text{-}Mn15/Al_2O_3$), which applies for all sorbents.

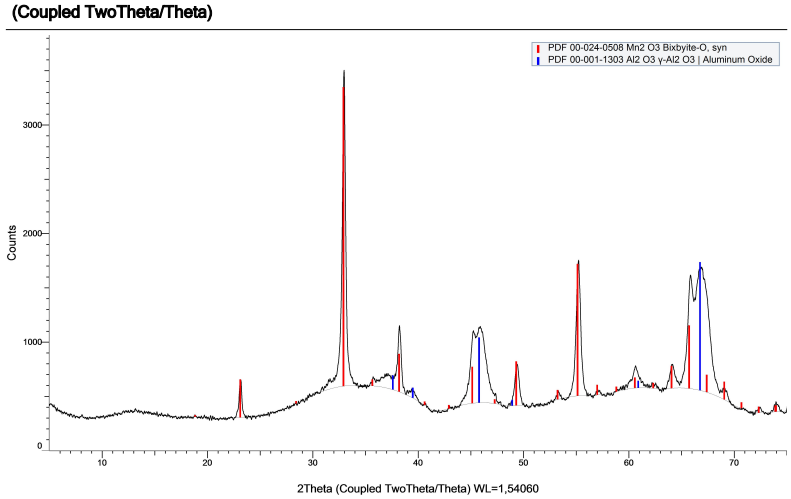

Figure F.5: Diffractogram for fresh $Zr10\text{-}Mn15/Al_2O_3$ sorbent prepared by incipient wetness impregnation and calcined at 700°C

Diffractograms for reacted sorbents prepared by incipient wetness impregnation and calcined at 500°C

Diffractograms for sorbents after 10 sorption- and regeneration experiments are presented here.

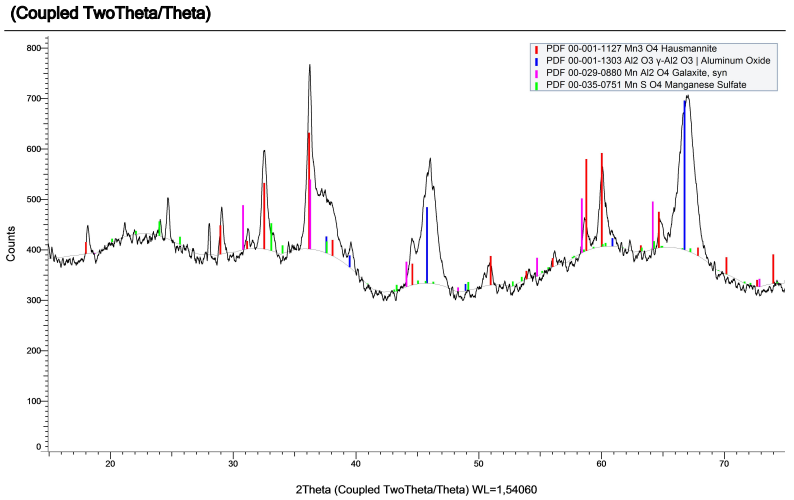

Figure F.6: Diffractogram for reacted $Mn15/Al_2O_3$ sorbent prepared by incipient wetness impregnation and calcined at 500°C

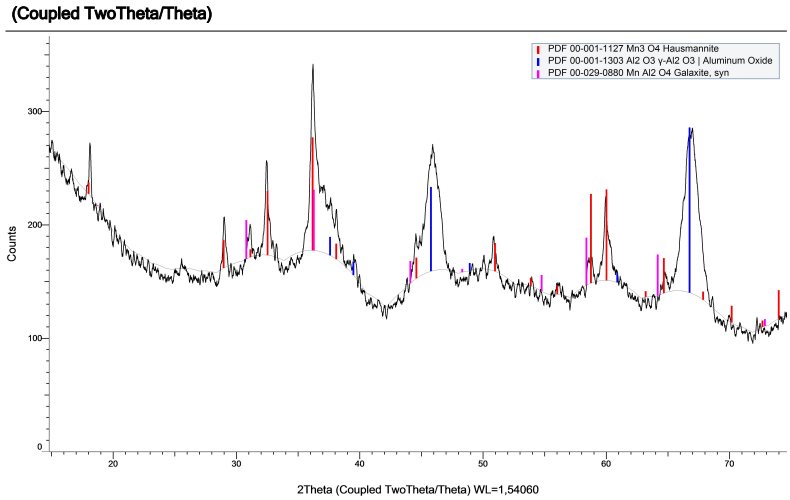

Figure F.7: Diffractogram for reacted Zr1-Mn15/Al_2O_3 sorbent prepared by incipient wetness impregnation and calcined at 500°C

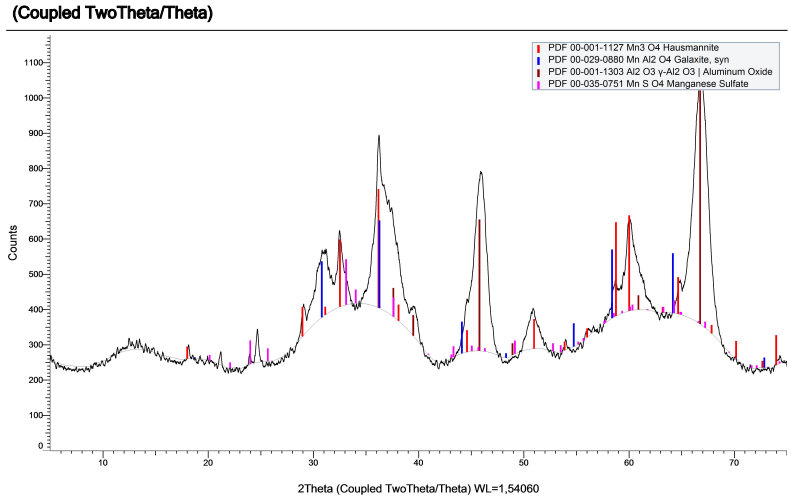

Figure F.8: Diffractogram for reacted Zr5-Mn15/Al_2O_3 sorbent prepared by incipient wetness impregnation and calcined at 500°C

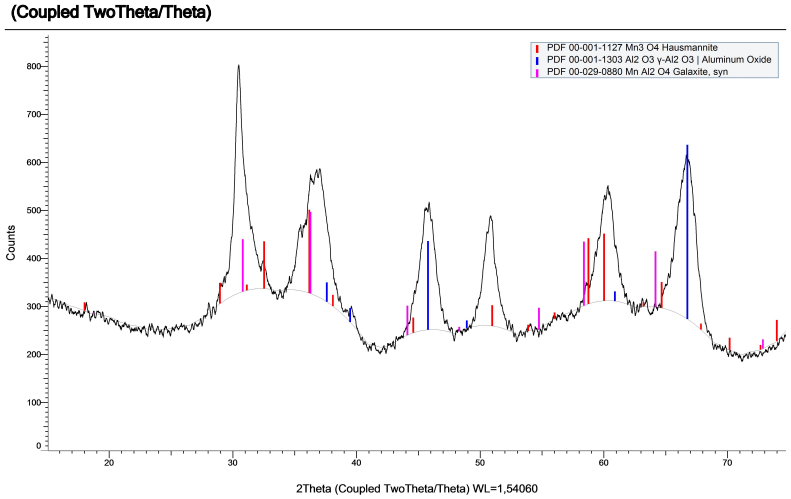

Figure F.9: Diffractogram for reacted Zr10-Mn15/Al_2O_3 sorbent prepared by incipient wetness impregnation and calcined at 500°C

Diffractograms for reacted sorbents prepared by incipient wetness impregnation and calcined at 700°C

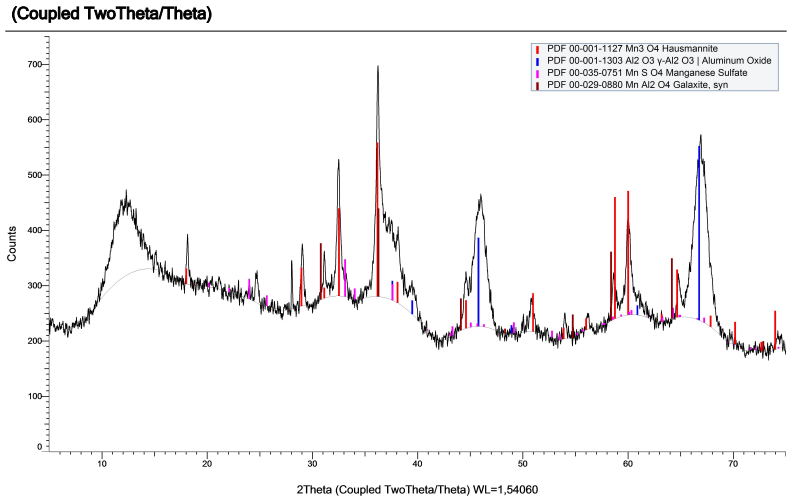

Figure F.10: Diffractogram for reacted $Mn15/Al_2O_3$ sorbent prepared by incipient wetness impregnation and calcined at 700°C

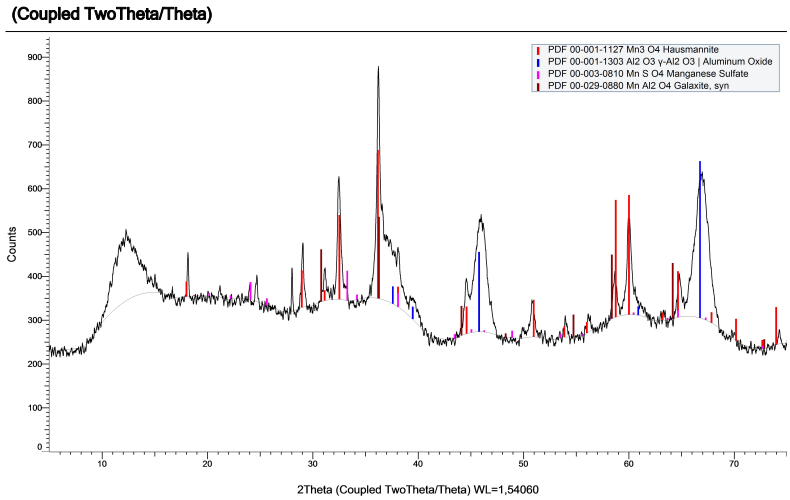

Figure F.11: Diffractogram for reacted Zr1-Mn15/Al_2O_3 sorbent prepared by incipient wetness impregnation and calcined at 700°C

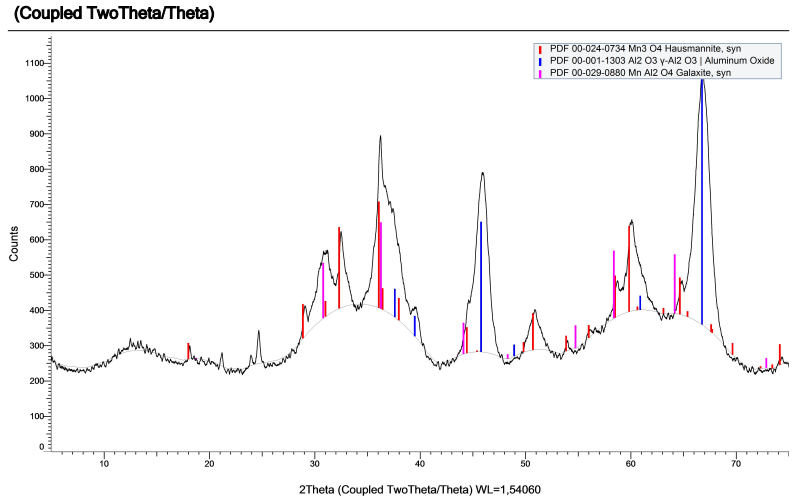

Figure F.12: Diffractogram for reacted Zr1-Mn15/Al_2O_3 sorbent prepared by incipient wetness impregnation and calcined at 700°C

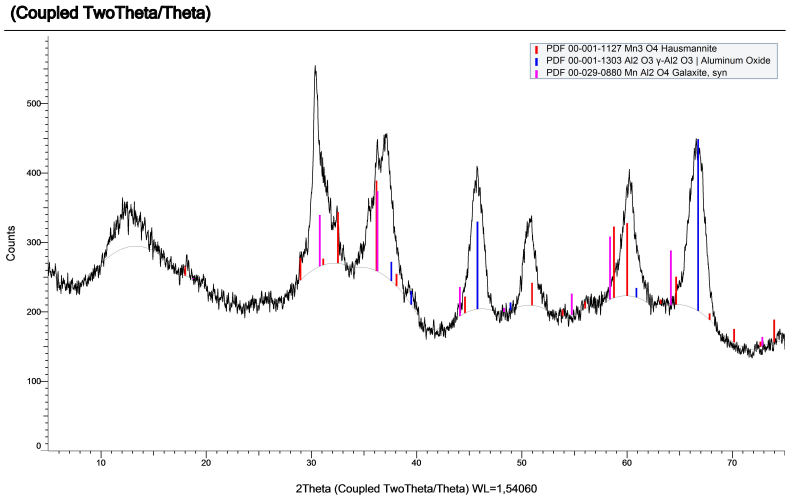

Figure F.13: Diffractogram for reacted Zr10-Mn15/Al_2O_3 sorbent prepared by incipient wetness impregnation and calcined at 700°C

Diffractograms for fresh sorbents prepared by co-precipitation and calcined at 500°C

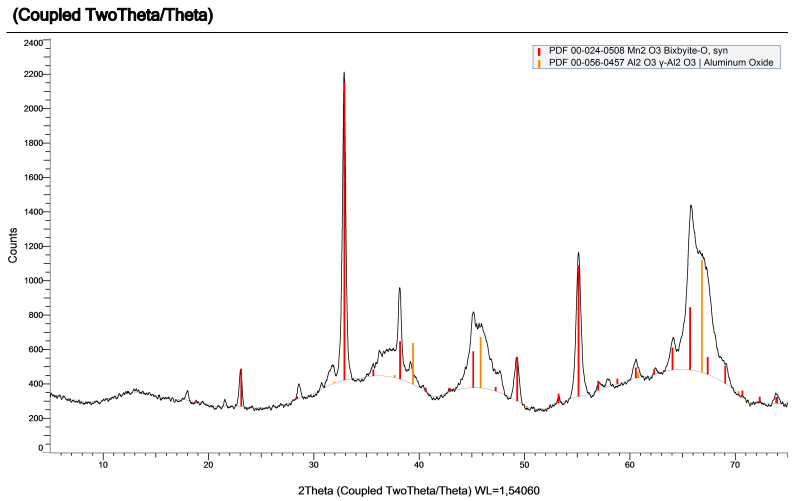

Figure F.14: Diffractogram for fresh Mn15/Al_2O_3 sorbent prepared by co-precipitation and calcined at 500°C

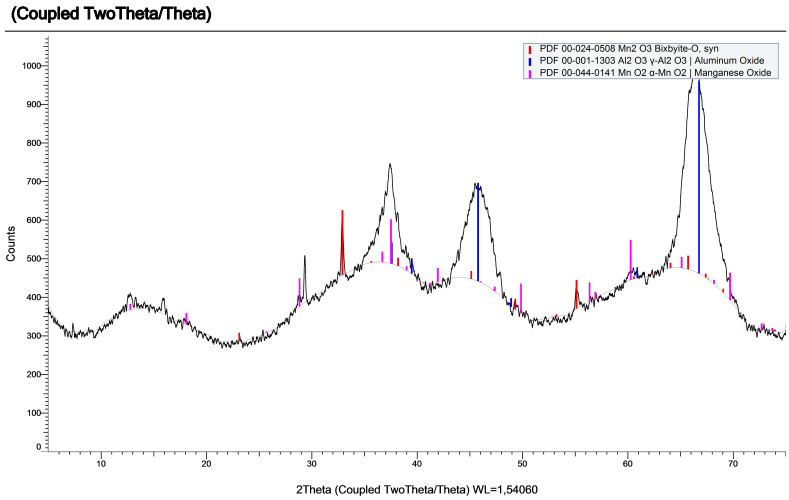

Figure F.15: Diffractogram for fresh Zr1-Mn15/Al_2O_3 sorbent prepared by co-precipitation and calcined at 500°C

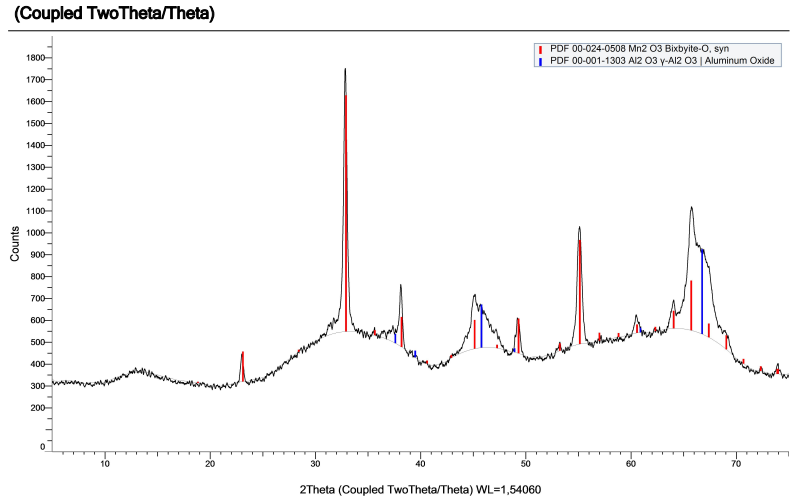

Figure F.16: Diffractogram for fresh Zr10-Mn15/Al_2O_3 sorbent prepared by co-precipitation and calcined at 500°C

Diffractograms for fresh sorbents prepared by co-precipitation and calcined at 700°C

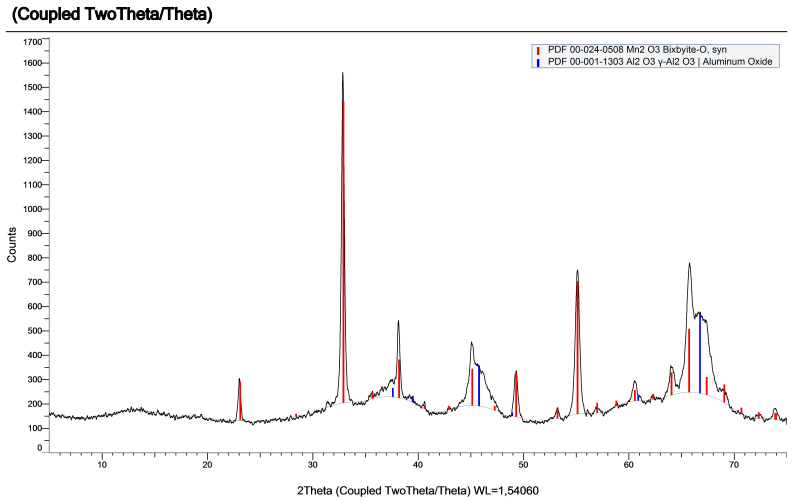

Figure F.17: Diffractogram for fresh $Mn15/Al_2O_3$ sorbent prepared by co-precipitation and calcined at 700°C

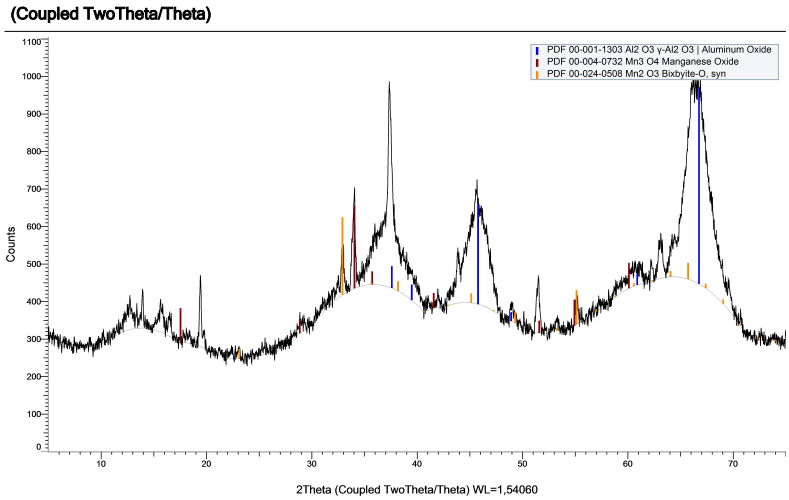

Figure F.18: Diffractogram for fresh Zr1-Mn15/Al_2O_3 sorbent prepared by co-precipitation and calcined at 700°C

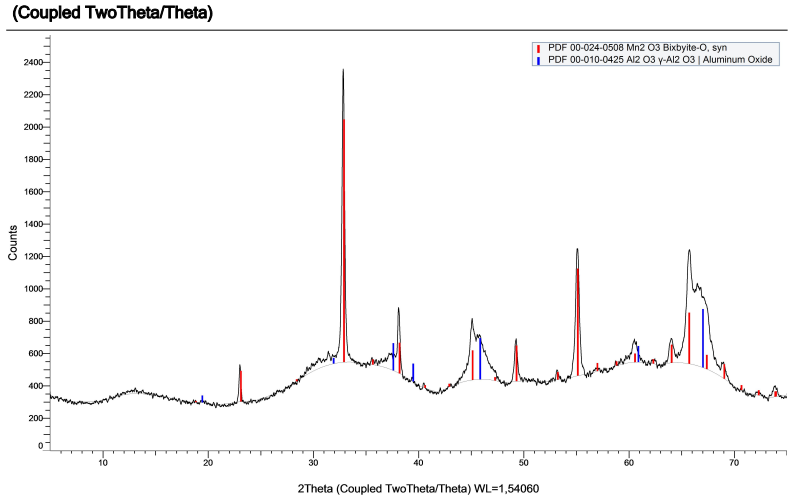

Figure F.19: Diffractogram for fresh Zr10-Mn15/Al_2O_3 sorbent prepared by co-precipitation and calcined at 700°C

Diffractograms for reacted sorbents prepared by co-precipitation

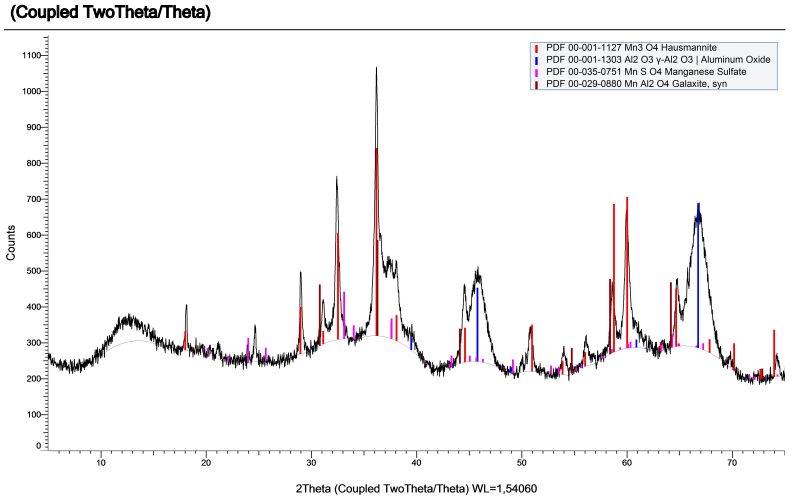

Figure F.20: Diffractogram for reacted $Mn15/Al_2O_3$ sorbent prepared by co-precipitation and calcined at 500°C

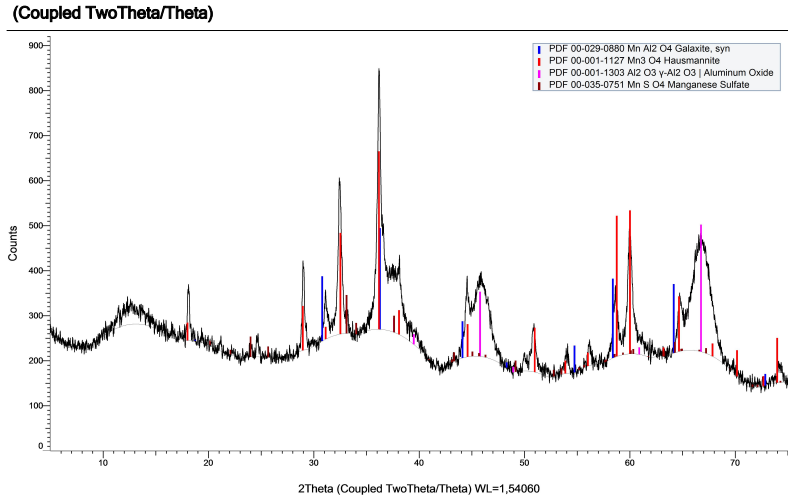

Figure F.21: Diffractogram for reacted $Mn15/Al_2O_3$ sorbent prepared by co-precipitation and calcined at 700°C

Appendix G

XRF Raw Data

XRF raw data for sorbents prepared by incipient wetness impregnation

$Mn15/Al_2O_3$ Cal500 (IWI)	Components [wt. %]						
	MnO	Al_2O_3	ZrO_2	K_2O	Fe_2O_3	SO_3	SiO_2
Pellet 1	14.5	84.7	0	0.31	0.07	x	0.44
Pellet 2	15.8	83.5	0	0.30	x	x	0.39
Pellet 3	15.1	84.3	0	0.29	x	0.07	0.22

$Mn15/Al_2O_3$ Cal700 (IWI)	Components [wt. %]						
	MnO	Al_2O_3	ZrO_2	K_2O	Fe_2O_3	SO_3	SiO_2
Pellet 1	14.5	84.9	0	0.28	x	x	0.30
Pellet 2	15.4	83.9	0	0.29	0.06	0.04	0.28
Pellet 3	12.8	87.0	0	0.28	x	x	x

$Zr1\text{-}Mn15/Al_2O_3$ Cal500 (IWI)	Components [wt. %]						
	MnO	Al_2O_3	ZrO_2	K_2O	Fe_2O_3	SO_3	SiO_2
Pellet 1	13.6	85.6	0.56	0.28	x	x	x
Pellet 2	13.2	85.8	0.60	0.30	0.05	x	x
Pellet 3	13.0	86.1	0.59	0.27	x	x	x

$Zr1\text{-}Mn15/Al_2O_3$ Cal700 (IWI)	Components [wt.%]						
	MnO	Al_2O_3	ZrO_2	K_2O	Fe_2O_3	SO_3	SiO_2
Pellet 1	14.8	84.1	0.64	0.31	0.04	x	x
Pellet 2	13.9	85.2	0.61	0.28	x	x	x
Pellet 3	14.6	84.4	0.66	0.28	0.04	x	x

Zr5-Mn15/Al_2O_3 Cal500 (IWI)	Components [wt.% %]						
	MnO	Al_2O_3	ZrO_2	K_2O	Fe_2O_3	SO_3	SiO_2
Pellet 1	18.0	76.3	5.03	0.33	x	0.04	0.79
Pellet 2	17.4	78.6	3.61	0.33	0.07	x	x
Pellet 3	16.8	79.3	3.46	0.37	x	0.08	x

Zr5-Mn15/Al_2O_3 Cal700 (IWI)	Components [wt.%]						
	MnO	Al_2O_3	ZrO_2	K_2O	Fe_2O_3	SO_3	SiO_2
Pellet 1	15.9	80.4	3.37	0.38	x	x	x
Pellet 2	16.4	79.8	3.39	0.36	0.06	x	x
Pellet 3	16.9	79.3	3.48	0.29	0.09	x	x

Zr10-Mn15/Al_2O_3 Cal500 (IWI)	Components [wt.%]							
	MnO	Al_2O_3	ZrO_2	K_2O	Fe_2O_3	SO_3	SiO_2	HfO_2
Pellet 1	18.4	73.0	7.83	0.42	0.07	x	x	0.29
Pellet 2	19.4	70.0	9.30	x	0.11	x	x	0.32
Pellet 3	17.0	72.8	9.59	x	0.05	0.02	x	0.28

Zr10-Mn15/Al_2O_3 Cal700 (IWI)	Components [wt.%]							
	MnO	Al_2O_3	ZrO_2	K_2O	Fe_2O_3	SO_3	SiO_2	HfO_2
Pellet 1	19.2	70.7	8.98	0.40	0.07	0.05	0.26	0.29
Pellet 2	17.2	74.8	7.29	0.44	x	0.09	x	0.20
Pellet 3	20.7	68.9	9.84	0.44	x	x	x	x

XRF raw data for sorbents prepared by co-precipitation

$Mn15/Al_2O_3$ Cal500 (CP)	Components [wt.%]						
	MnO	Al_2O_3	ZrO_2	K_2O	Fe_2O_3	SO_3	SiO_2
Pellet 1	14.7	84.4	0	0.57	x	0.08	0.23
Pellet 2	16.4	82.9	0	0.73	x	x	x
Pellet 3	20.2	78.7	0	0.73	x	x	0.33

$Mn15/Al_2O_3$ Cal700 (CP)	Components [wt.%]						
	MnO	Al_2O_3	ZrO_2	K_2O	Fe_2O_3	SO_3	SiO_2
Pellet 1	15.8	83.7	0	0.50	x	x	x
Pellet 2	18.2	81.2	0	0.66	x	x	x
Pellet 3	17.8	81.1	0	0.66	0.09	0.09	0.26

$Zr1\text{-}Mn15/Al_2O_3$ Cal500 (CP)	Components [wt.%]							
	MnO	Al_2O_3	ZrO_2	K_2O	Fe_2O_3	SO_3	SiO_2	Na_2O
Pellet 1	21.4	66.3	1.12	0.62	x	0.08	0.22	10.2
Pellet 2	23.2	65.3	1.25	0.58	x	0.11	x	9.58
Pellet 3	22.8	65.5	1.16	0.59	0.08	0.02	x	9.85

$Zr1\text{-}Mn15/Al_2O_3$ Cal700 (CP)	Components [wt.%]							
	MnO	Al_2O_3	ZrO_2	K_2O	Fe_2O_3	SO_3	SiO_2	Na_2O
Pellet 1	24.0	66.4	1.25	0.58	x	0.13	x	7.69
Pellet 2	22.7	65.5	1.30	0.58	x	x	0.17	9.80
Pellet 3	21.4	68.0	1.10	0.52	x	0.02	x	8.84

$Zr10\text{-}Mn15/Al_2O_3$ Cal500 (CP)	Components [wt.%]							
	MnO	Al_2O_3	ZrO_2	K_2O	Fe_2O_3	SO_3	SiO_2	HfO_2
Pellet 1	21.0	63.9	13.9	0.60	x	x	0.20	0.38
Pellet 2	22.4	60.1	16.4	0.64	x	x	x	0.39
Pellet 3	21.1	63.1	14.9	0.51	x	x	x	0.33

$Zr10\text{-}Mn15/Al_2O_3$ Cal700 (CP)	Components [wt.%]							
	MnO	Al_2O_3	ZrO_2	K_2O	Fe_2O_3	SO_3	SiO_2	HfO_2
Pellet 1	22.6	61.0	15.1	0.66	x	x	0.28	0.46
Pellet 2	22.1	61.9	14.9	0.54	x	x	x	0.55
Pellet 3	21.9	61.8	15.4	0.54	x	x	x	0.36